MESOPOROUS SILICON NANOPARTICLES FOR SOLAR-DRIVEN HYDROGEN GENERATION FROM WATER

by

Isabel S. Curtis

Submitted in partial fulfilment of the requirements
for the degree of Master of Science

at

Dalhousie University
Halifax, Nova Scotia
November 2021

Dalhousie University is located in Mi'kma'ki,
the ancestral and unceded territory of the Mi'kmaq.
We are all Treaty people.

TABLE OF CONTENTS

LIST OF TABLES

LIST OF FIGURES

ABSTRACT

Solar-driven hydrogen (H_2) production from water (water splitting) by semiconductor photocatalysts has potential as a sustainable and cost-competitive alternative to current H_2 production technologies. In recent years, mesoporous silicon (mp-Si) nanoparticles (NPs) have been recognized as promising photocatalysts for H_2 generation. To explore the influence of the synthetic conditions on their catalytic activity, mp-Si NPs were prepared by magnesiothermic reduction while varying the annealing temperature and time. These conditions were found to affect both the crystallinity and amount of oxygen present in the mp-Si NPs. The effect of porosity on the catalytic activity of mp-Si was investigated using porous SiO_2 precursors with varying pore size, which influenced the pore sizes in the mp-Si formed. The results in this thesis suggest that high crystallinity improves the performance of mp-Si photocatalysts, while high amounts of oxygen due to incomplete reduction or surface oxidation have a deleterious effect.

LIST OF ABBREVIATIONS USED

BE	Binding Energy
BET	Brunauer-Emmett-Teller
BF	Brightfield
BSE	Backscattered Electron
CB	Conduction band
CCD	Charged Coupled Device
CdS	Cadmium Sulfide
CHA	Concentric Hemispherical Analyzer
CH_3OH	Methanol
DFT	Density Functional Theory
E_k	Kinetic Energy
EtOH	Ethanol
FCEV	Fuel Cell Electric Vehicle
FEG	Field Emission Gun
FESEM	Field Emission Scanning Electron Microscopy
FWHM	Full Width at Half Maximum
GC	Gas Chromatography
g-C_3N_4	Graphitic Carbon Nitride
HCl	Hydrochloric Acid
HER	Hydrogen Evolution Reaction
HFC	Hydrogen Fuel Cell
HRTEM	High-Resolution Transmission Electron Microscopy
IR	Infrared
Mg-L	Magnesium < 0.1 mm particle size from Sigma Aldrich

Mg-S	Magnesium –325 mesh powder from Alfa Aesar
Mg-S2	Magnesium –325 mesh powder from Oakwood Chemical
mp-Si	Mesoporous Silicon
mp-Si100	Mesoporous Silicon prepared by annealing at 650 ºC for 0.5 h, followed by 100 ºC for 6 h
mp-Si200	Mesoporous Silicon prepared by annealing at 650 ºC for 0.5 h, followed by 200 ºC for 6 h
mp-Si300	Mesoporous Silicon prepared by annealing at 650 ºC for 0.5 h, followed by 300 ºC for 6 h
mp-Si650	Mesoporous Silicon prepared by annealing at 650 ºC for 3 h
mp-Sip4	Mesoporous Silicon prepared from SBA-15 silica with 4 nm pore size
mp-Sip6	Mesoporous Silicon prepared from SBA-15 silica with 6 nm pore size
mp-Sip8	Mesoporous Silicon prepared from SBA-15 silica with 8 nm pore size
NH_4OH	Ammonium Hydroxide
$Ni(OAc)_2$	Nickel (II) Acetate
$Ni(NO_3)_2$	Nickel (II) Nitrate
NP	Nanoparticle
OER	Oxygen Evolution Reaction
PEM	Proton-Exchange Membrane
PLOT	Porous Layer Open Tubular
PV-E	Photovoltaic Electrolysis
$SBA\text{-}15_{4nm}$	SBA-15 silica with a 4 nm pore size
$SBA\text{-}15_{6nm}$	SBA-15 silica with a 6 nm pore size
$SBA\text{-}15_{8nm}$	SBA-15 silica with a 8 nm pore size
SCOT	Support-Coated Open Tubular
SE	Secondary Electron

SEM	Scanning Electron Microscopy
SHE	Standard Hydrogen Electrode
SSA	Specific Surface Area
STH	Solar-to-Hydrogen Conversion Efficiency
TCD	Thermal Conductivity Detector
TEM	Transmission Electron Microscopy
TEOS	Tetraethyl Orthosilicate
UV	Ultraviolet
UV-Vis	Ultraviolet-Visible
VB	Valence Band
WCOT	Wall-Coated Open Tubular
XPS	X-Ray Photoelectron Spectroscopy
XRD	X-Ray Diffraction

ACKNOWLEDGEMENTS

First and foremost, I would like to thank my supervisor, Dr. Mita Dasog, for the opportunity to work in her laboratory and for her guidance over the course of my degree. I am beyond thankful to have had her support.

I would like to thank my lab mates for their friendship and the wonderful working environment that they provide. A special thank you goes to Sarah Martell for training me on the synthesis procedures and photocatalysis experiments. Furthermore, I thank everyone who has offered their services and/or guidance for the characterization of materials in this work: Dr. Kevin Hewitt and Ben Hansen (Raman), Pat Scallion (SEM), Andy George (XPS), Atri Maharaj and Anton Paar Canada Inc. (surface area analysis) and the Canadian Centre for Electron Microscopy (TEM).

Many thanks go to all the professors and staff at Dalhousie university who made an impact during my degree. Specifically, I would like to thank my committee member, Dr. Michael Freund for providing feedback on my work and thesis. I would also like to thank Dr. Jennifer MacDonald for supporting my interest in teaching and for providing me numerous opportunities to participate in teaching activities throughout my degree.

Finally, I would like to extend my thanks to my family and friends for supporting me through this journey.

CHAPTER 1. Introduction

1.1. The Hydrogen Economy

The hydrogen (H_2) economy refers to a proposed system in which H_2 is the main fuel used to supply the energy demands of a nation. The idea has been promoted since the 1970s; however, new-found interest in the H_2 economy has arisen as governments worldwide have increased efforts towards decarbonization of the current fuel economy.[1] In this regard, hydrogen fuel cell (HFC) technology has been successfully demonstrated for several applications. In the HFC, externally supplied fuel (H_2) and oxidant (O_2) are used to generate electricity *via* reverse water electrolysis using a metal catalyst. Compared to other fuels, H_2 has a high mass energy density (120 MJ kg^{-1}),[2] and the overall reaction of the HFC results in the emission of water as the only by-product.[3] These factors are largely what have led to the perceived viability of H_2 as a green energy vector.

HFCs are currently being explored and considered for stationary applications such as centralized energy networks[4] and distributed energy systems,[5] as well as for applications in transportation. For instance, several car manufacturing companies have made commitments to further the development of fuel cell electric vehicles (FCEVs) and H_2 infrastructure.[3] However, the potential of HFCs within the transportation sector is still heavily debated. Of the greener alternatives to conventional internal combustion engines, HFCs do offer some clear benefits, such as easy refueling for long distance driving (provided the infrastructure is available) and high power density. FCEVs could also help mitigate environmental concerns currently associated with battery electric vehicles, such as the mining of metals and harmful emissions from electricity generation.

Despite its benefits, popularization of HFC technology still warrants substantial research to address a plethora of challenges. The main challenges facing the H_2 fuel economy include the need for stable storage and supply of H_2, high overall cost and the lack of refuelling stations/infrastructure. H_2 storage poses a significant challenge for transportation applications specifically, as the weight, volume, efficiency, safety, and cost must be carefully considered. Current storage technologies have faced difficulties achieving a desirable balance between these factors. High cost due to the need for platinum (Pt), which is currently the preferred catalyst for HFCs, and expensive membrane materials also poses a significant barrier to their acceptance in consumer markets.[3] Finally, the development and expansion of green (emission-free) methods of H_2 production is imperative to achieve the full environmental benefits of HFCs.

Regardless of its potential for more widespread use in HFCs, H_2 is already used extensively in many industries for a variety of applications. H_2 is an important chemical feedstock in the petroleum and other chemical industries. H_2 is used catalytically in petroleum refining, as a reagent in the production of petrochemicals, in oil and fat hydrogenation, in the production of fertilizers (*i.e.*, ammonia production) and as a reducing agent for metallurgical applications and in the electronics industry.[6] Although highly abundant, H_2 is not present by itself in nature and must be extracted from the source (water, hydrocarbons or hydrides). Currently, steam natural gas (methane) reforming is the most common method of production for industrial H_2. Methane (CH_4) is catalytically reacted with steam at high temperature giving a mixture of H_2 and CO (Eq. 1.1). This is proceeded by the water-gas shift reaction to consume the CO and increase the H_2 yield. While this is currently the most established and low-cost H_2 production method, steam methane

reforming is reliant on fossil fuels, has a high energy consumption, and results in high emission of CO_2 (~7 kg per kg H_2).[7] As such, the development of alternative routes to producing H_2 are necessary if its large-scale use is to be continued.

$$CH_4 + H_2O \rightarrow CO + 3H_2 \quad (\Delta H = +251 \text{ MJ kmol}^{-1} CH_4) \qquad \text{Eq. 1.1}$$

$$CO + H_2O \rightarrow CO_2 + H_2 \quad (\Delta H = -41.4 \text{ MJ kmol}^{-1} CH_4) \qquad \text{Eq. 1.2}$$

Some other current methods to produce H_2 include gasification (thermo-chemical conversion of fossil fuels or biomass), electrolysis and biochemical processes such as dark fermentation.[5] Of these, gasification is currently the highest efficiency alternative to steam methane reforming; however, it also requires energy input and results in greenhouse gas emissions. Biochemical processes can reduce energy consumption, but suffer from low H_2 yields.[5] Water electrolysis (or electrochemical water splitting) offers a low-carbon alternative to produce H_2. In this electrochemical process, water is "split" into H_2 and oxygen (O_2) using electrical energy. The overall redox reaction is shown in Eq. 1.3.

$$2H_2O \rightarrow 2H_2 + O_2 \quad (E^o_{cell} = -1.23 \text{ V}) \qquad \text{Eq. 1.3}$$

In electrolysis, the electrolyser is composed of a cathode, an anode, and an electrolyte, which is the medium for ion transport. The reaction in Eq. 1.3 can be divided into two redox half reactions, the hydrogen evolution reaction (HER) and the oxygen evolution reaction (OER). The ions involved in each half reaction depends on the pH of the electrolyte in the electrochemical cell.[8] The HER and OER reactions under basic and acidic conditions are shown in Eq. 1.4 and 1.5, and Eq. 1.6 and 1.7, respectively.

Basic conditions:

$$4OH^- \rightarrow O_2 + 2H_2O + 4e^- \quad \text{Eq. 1.4}$$

$$2H_2O + 2e^- \rightarrow H_2 + 2OH^- \quad \text{Eq. 1.5}$$

Acidic conditions:

$$2H_2O \rightarrow O_2 + 4H^+ + 4e^- \quad \text{Eq. 1.6}$$

$$2H^+ + 2e^- \rightarrow H_2 \quad \text{Eq. 1.7}$$

Currently, alkaline and proton-exchange membrane (PEM) electrolysers are the most mature technologies and have been employed in some industrial settings.[9] However, more widespread integration is limited by electrolyser lifetimes and overall cost. The cost of CH_4 reforming is about 2 – 5 times lower than the cost of current electrolysis technologies due to the price of the required materials and electricity.[5]

1.2. Solar-Mediated Hydrogen Production

Of the renewable energy resources at our disposal, solar energy is a favourable option. The solar energy irradiating the surface of the Earth (1.3×10^5 TW) exceeds the current global energy demand by roughly four orders of magnitude.[10] As such, solar-mediated pathways could offer effective and renewable H_2 production methods for its current industrial uses. Additionally, the conversion of solar energy into stable chemical energy (in the form of H_2) could help alleviate the issues of seasonal intermittent and regional variability. Electrochemical water splitting methods can utilize solar energy for H_2 generation using light-harvesting photovoltaic cells to supply the electricity (photovoltaic electrolysis). Alternatively, H_2 generation *via* water splitting through

photoelectrochemical (PEC),[10–12] photocatalytic,[8,10] photobiological,[13,14] and solar thermochemical[15–17] pathways have been researched extensively. Solar thermochemical pathways use concentrated solar energy to drive the endothermic decomposition of water into H_2 and O_2. The most viable routes to solar thermochemical water splitting rely on a two-step cycle involving the reduction and subsequent re-oxidation of metal oxides, which lower the water decomposition temperature.[16] However, the reaction still requires high temperatures (> 1000 °C) which limits its applications.[18] Photobiological pathways take advantage of biological photosystems and other enzymes which catalyze the water splitting half reactions. For instance, to achieve H_2 production through light absorption, the photosystems present in photosynthetic organisms can be coupled with H_2-producing hydrogenases or nitrogenases either within the microorganism,[14] or artificially using isolated enzymes.[13] Such technologies are likely not viable for large-scale H_2 production due to the high cost and low lifetimes of enzymes.[19]

Solar-driven water splitting using light-harvesting semiconductors is a popular and perhaps more viable approach to renewable H_2 production. As mentioned, photovoltaic electrolysis (PV-E) methods apply solar energy harvesting technologies to power water splitting via electrolysis (Fig. 1.1A). In a PV-E reactor, an external photovoltaic device converts solar radiation into electrical energy which is then supplied to the electrolytic cell. Alternatively, in PEC water splitting (Fig. 1.1B), the electrolysis redox couple consists of at least one semiconductor electrode (a photoanode or photocathode). The absorption of solar radiation by the semiconductor electrode generates electron-hole pairs which can participate in redox reactions (depending on the positioning of its valence and conduction bands). An externally applied electric bias provides the additional voltage needed to drive

the overall water splitting reaction and overcome slow reaction kinetics.[11] The third main category of the semiconductor-based water splitting methods is photocatalysis (Fig. 1.1C).[20] Like PEC methods, the photocatalytic method relies on semiconductor materials to drive the water splitting half reactions, however, it does not require application of an external bias. Instead, H_2 generation is directly catalyzed on the surface of suspended photocatalysts with favourable electronic band positioning. Numerous semiconducting materials have been investigated for photocatalytic water splitting, including titanium dioxide (TiO_2), carbon nitride, silicon (Si), and other particulate photocatalysts.[8] These are discussed in more detail in the following sections.

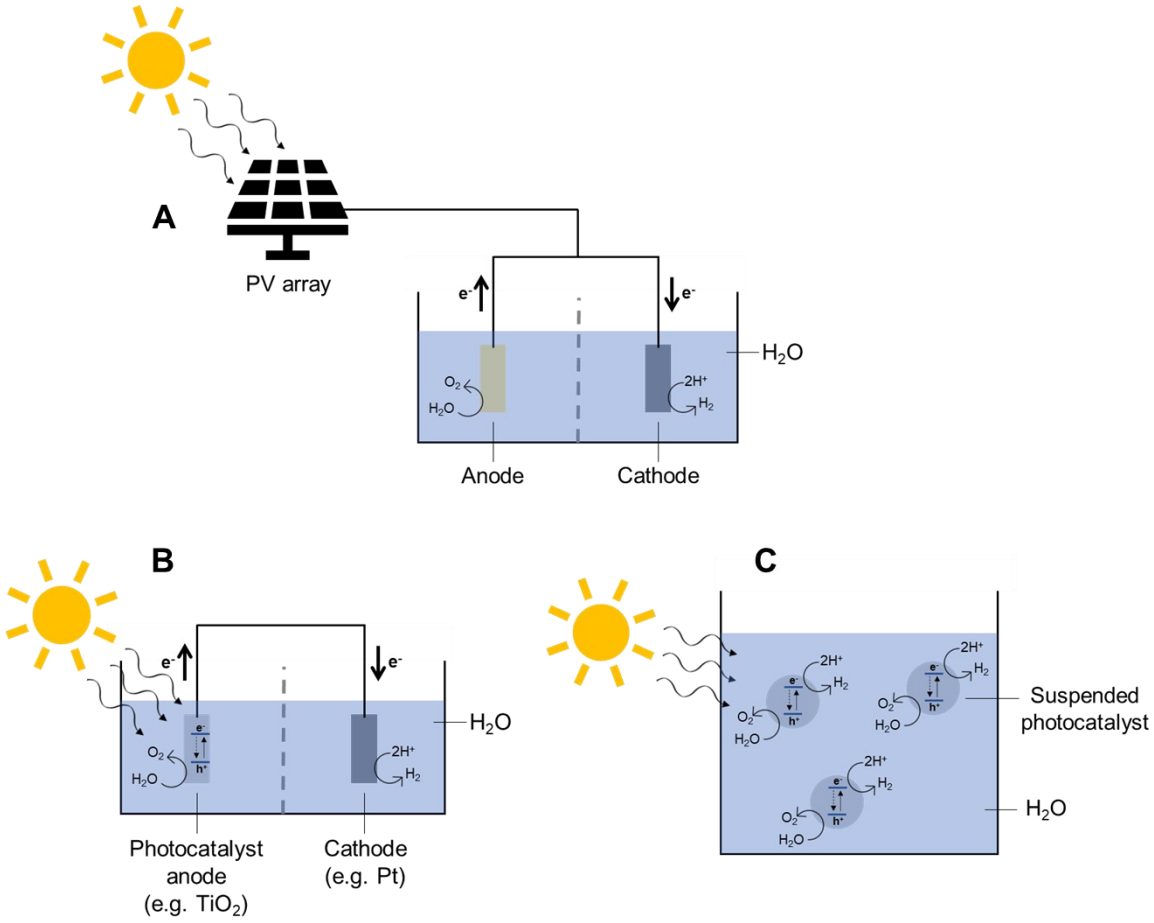

Figure 1. 1. Illustration depicting the three main categories of solar-mediated H_2 generation *via* water splitting using semiconductors: (A) photovoltaic-powered electrolysis (PV-E), (B) photoelectrochemical (PEC) water splitting and (C) photocatalytic water splitting.

1.3. Photocatalytic Water Splitting

The feasibility of H_2 production *via* water splitting using a heterogenous photocatalyst was first demonstrated by Fujishima and Honda in 1972, using a TiO_2 electrode coupled with a Pt cathode in a PEC cell.[21] Later, in 1977, Schrauzer *et al.* demonstrated H_2 evolution on TiO_2 powder under UV irradiation with no external bias.[22]

These discoveries paved the way for research into solar-driven water splitting using particulate semiconductor photocatalysts.

In a particulate photocatalyst system, water splitting occurs within an aqueous suspension of semiconductor particles under solar illumination. The reactions (HER and/or OER) occur on the surface of the semiconductor particles and are directly driven by photogenerated charge carriers (electrons and holes, respectively). Compared to PV-E and PEC methods, photocatalytic systems based on simple powder photocatalysts have the potential to facilitate larger scale-up.[20] Assuming that a photocatalyst having the required efficiency can be obtained, H_2 production *via* solar-driven water splitting using suspended particulate photocatalysts has also been predicted to be inexpensive by technoeconomic analysis, making it cost competitive with the steam CH_4 reforming process.[23,24]

1.3.1. Fundamentals of Photocatalytic Water Splitting

Photocatalytic water splitting on semiconductor particles occurs in three main steps: 1) light absorption, 2) charge carrier separation and diffusion, and 3) transfer of charge carriers from the particle surface to perform the chemical reaction. The efficiency of each step contributes to the overall efficiency of the photocatalyst system.[8]

Light Absorption.

The process of photocatalysis begins with an optical excitation in the semiconductor particle. Incident light with energy equal to or greater than the bandgap ($h\nu \geq E_g$) can be absorbed, resulting in the excitation of an electron from the valence band (VB) to the conduction band (CB) of the semiconductor material. The charge carriers generated from the excitation are called electron-hole pairs, where a hole refers to the lack of an

electron in its position in the VB after being promoted to the CB. The solar spectrum is comprised of mainly ultraviolet (UV), visible, and infrared (IR) radiation. Of these, about 53% is in the visible range (400 nm < λ < 800 nm) and only about 4% is in the UV (λ < 400 nm).[10] To achieve an acceptable solar-to-hydrogen conversion efficiency (STH) from water splitting, a good photocatalyst should have a bandgap narrow enough to absorb visible radiation. If only UV radiation up to 400 nm is used, the maximum STH of the photocatalyst would be limited to no more than 2%.[8]

Charge Carrier Separation and Diffusion.

To participate in interfacial reactions, electron-hole pairs must migrate from the bulk to the surface of the photocatalyst particle. This process faces kinetic competition with the elimination of charge carriers through recombination, which can limit the photocatalyst efficiency. Electron-hole pairs can recombine through radiative (band-to-band) recombination, or *via* trap states (energy levels introduced by defects or impurities) in the forbidden gap (Fig. 1.2). The carrier lifetime, τ, is the time required for charge carrier concentrations to return to their equilibrium values (recombination of electron-hole pairs) and is typically short, occurring on the picosecond to microsecond time scale.[8]

The ability of photogenerated charge carriers to diffuse through a material depends on the electronic structure of the semiconductor and is represented by their diffusion coefficient, D. D is related to the drift mobility, μ, of the charge carriers in the semiconductor by Eq. 1.8 and can be used to define the average diffusion length (L) a carrier will travel before recombining (Eq. 1.9).

$$D = \frac{K_B T}{q} \mu \qquad \text{Eq. 1.8}$$

$$L = (D\tau)^{1/2} \qquad \text{Eq. 1.9}$$

where K_B is the Boltzmann constant, T is the absolute temperature and q is the electrical charge of the carrier (in Eq. 1.8).

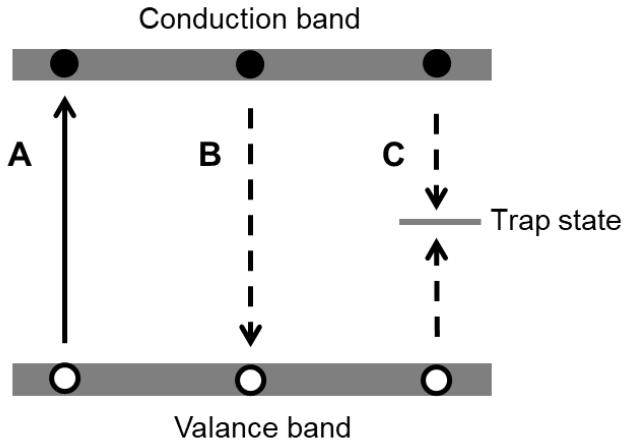

Figure 1. 2. Schematic depicting the electronic processes which may occur following optical excitation in a semiconductor: (A) promotion of a VB electron to the CB, generating an electron-hole pair, (B) radiative (band-to-band) recombination, and (C) recombination facilitated by a trap state in the forbidden gap.

Transfer of Charge Carriers to Perform the Chemical Reaction.

In aqueous suspensions of the appropriate photocatalyst, water splitting can proceed by the half reactions shown in Fig. 1.3. In order to drive these reactions, the transfer of charge carriers from the photocatalyst surface to the reactants must be thermodynamically favourable. Overall water splitting by a single photocatalyst can only occur if the CB and VB "straddle" the reduction and oxidation potentials of water (Fig. 1.3). That is, the CB

minimum must be more negative than the H^+/H_2 reduction potential, and the VB maximum must be more positive than the water (H_2O/O_2) oxidation potential; 0 and +1.23 V *vs.* the standard hydrogen electrode (SHE), respectively. The minimum theoretical band gap for such a photocatalyst should therefore be slightly larger than 1.23 eV. However, additional kinetic overpotentials required to drive electron transfer at reasonable rates suggest that the band gap should exceed at least 1.6 eV.[8]

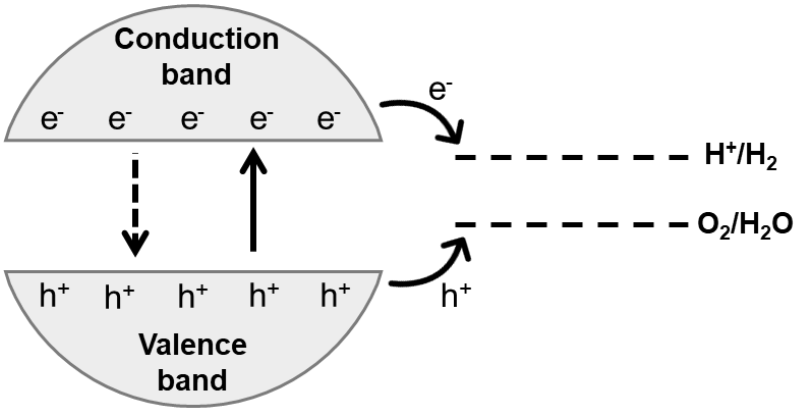

Figure 1. 3. Photocatalyst particle and energy level diagram showing the thermodynamic requirements for overall water splitting.

1.3.2. Methods to Improve Photocatalytic Activity

Despite the potential of particulate photocatalyst systems for cost-effective and renewable H_2 generation, several challenges continue to limit their efficiency. Fast rates of charge carrier recombination and trapping are common problems associated with many photocatalyst materials. Recombination can be facilitated by charge carrier trapping at bulk or surface trap states in the semiconductor. Trapping can also prevent charge migration to the surface catalytic sites.[8] Furthermore, the thermodynamic requirements for overall water splitting pose a significant challenge to developing efficient photocatalysts for simultaneous H_2 and O_2 evolution. Photocatalysts for overall water splitting have wide band gaps which hinder their ability to absorb in the full range of the solar spectrum, greatly limiting their STH.

There are several considerations to be made when designing efficient photocatalysts for water splitting. For instance, materials with high crystallinity have reduced structural imperfections such as vacancies and dislocations that commonly act as recombination sites. Nanostructuring can also improve the water splitting capability of semiconductors due to shorter carrier migration distances, which reduces recombination (especially if the particle size is smaller than the diffusion lengths). Furthermore, quantum confinement effects that occur in semiconductor nanoparticles (NPs) can be used to tune the band structure.[8] Many photocatalyst systems also incorporate metal cocatalysts which can serve as catalytic sites, prevent back-reactions and improve electron-hole separation.[25] Other strategies to improve photocatalytic activity include doping (which can be used to tune the band gap and carrier dynamics), dye sensitization and plasmonic enhancement.[8]

Alternative to photocatalysts for overall water splitting, narrow bandgap photocatalysts which can absorb light in the visible region have been investigated for catalysis of either the H_2 or O_2 evolution half reactions individually. Given an appropriate photocatalyst for each half reaction, a Z-scheme configuration (inspired by natural photosynthesis) could be used to achieve overall water splitting without the need for sacrificial reagents.[26] In the Z-scheme, water is oxidized to O_2 by photogenerated holes on one photocatalyst. To complete the cycle, electrons in the CB of the O_2 evolution photocatalyst must pass through a redox shuttle which mediates electron transfer to the valence band of the H_2 evolution photocatalyst (Fig. 1.4).

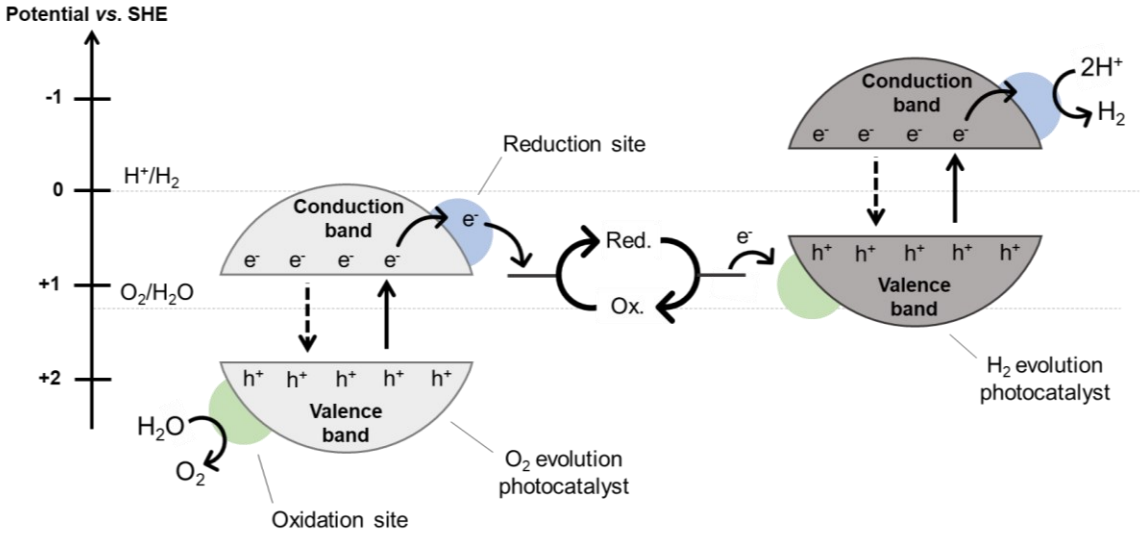

Figure 1. 4. Energy level diagram for photocatalytic water splitting through a two-step photoexcitation (Z-scheme) system.

1.3.3. Photocatalysts for Overall Water Splitting

A variety of wide bandgap photocatalysts have been investigated for single-step overall water splitting (Fig. 1.5). Of these, TiO_2 has been widely studied since its potential for water splitting was first demonstrated in the 70s using a PEC system.[21] Anatase and rutile TiO_2 are the most studied polymorphs for photocatalysis, with rutile typically showing superior performance for overall water splitting with stoichiometric H_2/O_2 production under UV irradiation.[27] Besides TiO_2, several other metal oxides have been explored as water splitting photocatalysts. Some notable examples present in the literature are Cu_2O,[28] ZrO_2,[29,30] Ta_2O_5[31] and Ga_2O_3.[32,33] Most metal oxide photocatalysts capable of overall water splitting consist of metal cations with either d^0 or d^{10} configurations, which are primarily responsible for forming the CBs of the semiconductor (composed of d and sp orbitals, respectively). The VBs are usually composed of O 2p orbitals, which give a highly positive VB position of ~3 V *vs*. SHE.[8] To have a CB that is also sufficiently negative to drive the H^+/H_2 reaction, the band gaps of metal oxide photocatalysts are usually too large to absorb visible light ($\lambda > 400$ nm). As such, most metal oxide photocatalysts are only active under UV irradiation. Perovskite-type photocatalysts have also been explored for overall water splitting. One of the best studied is $SrTiO_3$, first reported to achieve overall water splitting under UV light in 1980.[34] Additionally, tantalates with layered perovskite structures such as $KTaO_3$, $NaTaO_3$,[35] and others[36] have shown promising activities for overall water splitting, but are typically only active under UV irradiation.

Compared to metal oxides, metal nitride and oxynitride photocatalysts have potential for improved solar light absorption since N 2p orbitals tend to form VBs at more negative potentials than the O 2p orbitals. For instance, the wide bandgap of Ta_2O_5 (3.9

eV) limits its absorption spectrum to only UV light, while the absorption spectra of TaON (E_g = 2.4) and Ta_3N_5 (E_g = 2.1 eV) are extended into the visible region due to their VBs consisting of O 2p + N 2p and N 2p orbitals, respectively.[8] The d^{10} metal nitrides GaN and Ge_3N_4 also have band structures which meet the thermodynamic requirements for overall water splitting, but have wider bandgaps due to a more negative CB position.[36,37] This is useful to drive the HER, but renders them only active under UV light. Alternatively, solid solutions of GaN or Ge_3N_4 with ZnO have been explored to achieve narrower bandgaps for more efficient water splitting.[36,38] Metal sulphides such as CdS and ZnS have also been considered as visible light-responsive photocatalysts.[8,36]

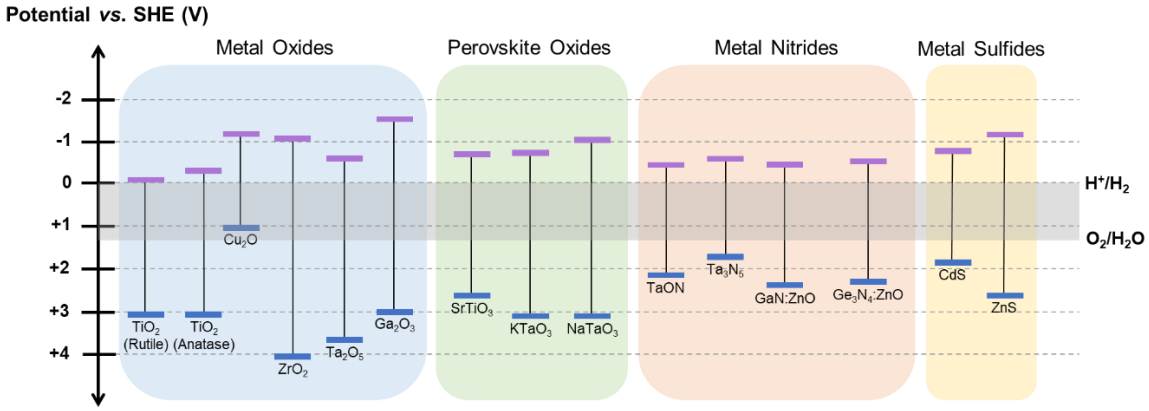

Figure 1. 5. Examples of wide bandgap photocatalysts with suitable band positions for overall water splitting.

Compared to metal-based photocatalysts, carbon or silicon-based photocatalysts carry the advantages of lower cost and high natural abundance. Examples include graphitic carbon nitride (g-C_3N_4)[39,40] and silicon carbide (SiC),[41,42] which have tunable band gaps and band positioning sufficient for both the HER and OER.

Although the aforementioned photocatalysts have suitable band gaps for overall water splitting, most are inactive without the aid of metal cocatalysts, heteroatom doping or other modifications.[8] The photostability of the catalyst materials must also be considered. For instance, metal sulfides are prone to photocorrosion since S^{2-} is easily oxidized by the photogenerated holes (Eq. 1.10). ZnO can also be corroded by a similar mechanism.[43]

$$CdS + 2h^+ \rightarrow Cd^{2+} + S \qquad \text{Eq. 1.10}$$

Various wide bandgap photocatalysts have also been investigated for either H_2 or O_2 evolution in the presence of sacrificial reagents. An electron donor or acceptor is used to drive photocatalysis of either the HER or OER, respectively, to support charge carrier separation and supress undesirable recombination or back reactions. These sacrificial reagents should be more easily oxidized or reduced compared to water and consume the electrons or holes irreversibly. Silver cations (Ag^+) or methanol (CH_3OH) are commonly added to photocatalyst systems as electron or hole scavengers, respectively (Eq. 1.11 and 1.12).[10,44] In photocatalytic H_2 generation, CH_3OH is first oxidized to CH_2O (Eq. 1.13).[45] Further oxidation can also occur *via* Eq. 1.14 and Eq. 1.15, giving the overall reaction in Eq. 1.16.[46]

$$Ag^+ + e^- \rightarrow Ag \quad (E^o_{Ag^+/Ag} = 0.08\ V) \qquad \text{Eq. 1.11}$$

$$CH_3OH + 2h^+ \rightarrow CH_2O + 2H^+ \quad (E^o_{CH_2O/CH_3OH} = 0.13\ V) \qquad \text{Eq. 1.12}$$

Methanol oxidation pathway:

$$CH_3OH \rightarrow CH_2O + H_2 \quad \text{Eq. 1.13}$$

$$CH_2O + H_2O \rightarrow HCOOH + H_2 \quad \text{Eq. 1.14}$$

$$HCOOH \rightarrow CO_2 + H_2 \quad \text{Eq. 1.15}$$

Overall reaction:

$$CH_3OH + H_2O \rightarrow CO_2 + 3H_2 \quad \text{Eq. 1.16}$$

1.3.4. Photocatalysts for Hydrogen Evolution

Of the water splitting half reactions, the OER is generally more difficult to achieve, as it is a complex 4-electron process which requires higher overpotentials than the HER.[39] For this reason, paired with the high demand for sustainable H_2, many investigations of water splitting photocatalysts have focussed on H_2 production in the presence of sacrificial reagents. A myriad of semiconductor materials have been investigated for H_2 evolution via water splitting, including various metal oxides, nitrides and sulfides,[8,47,48] layered perovskites,[48] metal-organic frameworks (MOFs),[49] intramolecular assemblies,[50] carbon-based materials,[39,48] and composite materials.[48,51] Some examples commonly seen in the literature are presented in the following discussion and in Table 1.1. Ideally, photocatalysts for sustainable H_2 production should be photostable and efficient under solar illumination, naturally abundant, inexpensive, and relatively easy to synthesize.

Nanostructured TiO_2 is one of the most widely studied photocatalysts due to its low toxicity, high photochemical stability, high abundance and low cost. However, the wide band gap of TiO_2 results in poor solar energy utilization. Furthermore, fast recombination

and high overpotentials for H^+ reduction on TiO_2 surfaces limit its applicability to H_2 generation.[47] Numerous efforts have been made to improve the photocatalytic performance of TiO_2 in the presence of sacrificial reagent (CH_3OH), through structural modifications, and through the integration of cocatalyst materials.[47,52] For instance, nanocrystalline mesoporous TiO_2 was found to outperform commercial TiO_2 powder due to its high surface area and crystallinity.[53] Furthermore, the incorporation of a noble metal cocatalyst, namely Pt, can greatly enhance the H_2 evolution rate compared to bare TiO_2.[54] Incorporation of plasmonic cocatalysts such as Ag has also been shown to greatly enhance the photocatalytic performance of TiO_2 since the plasmon resonance extends light absorption to the visible region.[55] Nonetheless, the high cost and low abundance of such precious metals limits the practicality of these systems.

Cadmium sulfide (CdS, E_g ~2.4 eV) is a popular visible light photocatalyst for H_2 production. CdS suffers from instability due to photocorrosion; however, this can be mediated by using appropriate sacrificial reagents containing S^{2-} electron donors.[56] Modification with Pt[56] or noble-metal free cocatalysts such as MoS_2 significantly enhances H_2 evolution performance compared to pure CdS.[57–59] Specifically, MoS_2 is commonly incorporated onto CdS photocatalysts as it also functions to prevent photocorrosion.[57]

In recent years, g-C_3N_4 has gained popularity due to its unique electronic structure and properties. Moreover, it is made from abundant elements, has good stability and is nontoxic.[60] Depending on its structure, g-C_3N_4 can be suitable for visible light absorption; however, high recombination rates (especially in bulk g-C_3N_4) tend to limit its efficiency.[61] Various literature reports have revealed that photocatalytic performance is heavily reliant on the structural details of g-C_3N_4. As such, efforts to improve its activity include

exfoliating bulk g-C_3N_4 to single-layer nanosheets,[62,63] controlled polymerization,[60,64] and structural ordering into condensed nanostructures.[65,66] Among the highest quantum yields have been achieved by carefully tailoring the degree of polymerization and protonation of g-C_3N_4, controlled by the precursor and synthetic parameters.[60]

Composite materials which aim to combine the desirable properties of multiple photocatalyst materials have also been investigated for H_2 production. Furthermore, heterojunctions between semiconductors can provide more efficient charge separation and reduce the rate of recombination.[61] For example, Yang and coworkers constructed CdS/MoS_2 core-shell composites which showed significantly enhanced H_2 evolution performance compared to other CdS systems.[57] Composites of g-C_3N_4 such as g-C_3N_4/TiO_2[61] and g-C_3N_4/SiC[67] have been investigated in attempts to improve charge mobility in g-C_3N_4. However, the photocatalytic performance of these materials has still been relatively low.

Table 1. 1. Some examples of photocatalyst materials used for H_2 production from water and their H_2 evolution rates.

Photocatalyst Material	Cocatalyst	Light Source	H_2 Evolution Rate ($\mu mol\ h^{-1}\ g^{-1}$)	Reference
TiO_2	–	450-W Hg lamp	419.5	53
Mesoporous TiO_2	–	300-W Hg lamp	1652.5	53
TiO_2	Pt (0.6 wt%)	300-W Xe lamp	8450	54
TiO_2 nanowires	Pt (0.5 wt%)	450-W Hg lamp	4300	68
TiO_2	Ag_2O (1 wt%)	Solar light,19 $mW\ cm^{-2}$	67000	55
CdS	Pt (1 wt%)	300-W Xe lamp, > 420 nm	9357	56
CdS	MoS_2/graphene (2 wt%)	300-W Xe lamp, > 420 nm	6103	59
CdS/MoS_2	–	300-W Xe lamp, > 410 nm	26140	57
Mesoporous g-C_3N_4 nanosheets	Pt (3 wt%)	500-W Hg lamp, > 420 nm	1490	64
g-C_3N_4 (urea synthesis)	Pt (3 wt%)	300-W Xe lamp, > 395 nm	3327.5	60
g-C_3N_4/TiO_2	Pt (3 wt%)	300-W Xe lamp, > 420 nm	513	61
g-C_3N_4/SiC	Pt (1 wt%)	300-W Xe lamp, > 420 nm	182	67

1.3.5. Mesoporous Silicon

In recent years, nanostructured Si have shown promise as photocatalysts for H_2 generation.[69–76] Si is an attractive semiconductor for this application given its abundance, non-toxicity, and ability to absorb in the UV to near IR region of the solar spectrum.[74,77] While bulk Si (E_g = 1.1 eV) has been well-established for electricity production in solar cells[78] and fuel formation in PEC systems,[79,80] its applicability as a particulate photocatalyst remains relatively under investigated.

Mesoporous silicon (mp-Si) is a sponge-like material with pore diameters between 2 and 50 nm.[81] Given attractive properties such as high surface area and pore volume, mp-Si has been extensively explored for applications in optics,[82] sensors,[83] drug delivery,[84,85] gas storage,[86] high capacity anode material for Li-ion batteries,[87] chemical conversion of species such as CO_2,[88,89] as well as photocatalytic H_2 evolution.[90–93] Recent studies have demonstrated that mp-Si NPs are attractive particulate photocatalysts for H_2 production for the following reasons: 1) the porous network provides high-surface area and more catalytic sites which enhances the amount of H_2 generated, 2) the nano-structuring shifts the conduction band edge position of Si favorably to further facilitate electron transfer to drive H_2 formation, and 3) the pore structure can enhance light absorption through pore-induced multiple reflections.[74,93]

Several synthetic routes have been reported to produce porous Si, including top-down etching methods[94–96] and bottom-up methods such as chemical vapour deposition,[84] carbothermal reduction,[97] and metallothermic reduction.[85] Of these, metallothermic reduction has received significant attention as a straightforward method to produce mp-Si NPs from inexpensive precursors and at lower temperatures compared to carbothermal

reduction.[97] Magnesium (Mg) and Aluminum (Al) are routinely used reducing agents for metallothermic reduction as they are relatively inexpensive, easy to handle, and produce easily removable by-products. Specifically, magnesiothermic reduction using Mg metal has become a popular method for synthesizing mp-Si photocatalysts, as it tends to yield products with high surface area.[85]

1.4. Motivation for Research

In previous reports, mp-Si NPs investigated for photocatalytic H_2 generation have been prepared either *via* reduction of $SiCl_4$ using a NaK alloy[93] or through magnesiothermic reduction of silica (SiO_2) precursors.[70,72,74,76] As with other semiconductor materials, properties such as the crystallinity, surface area, porosity, and surface chemistry of mp-Si should affect the charge carrier dynamics, density of trap states, availability of reaction sites, and light harvesting ability of the material.[8] For mp-Si synthesized *via* metallothermic reduction, such properties can be influenced by a number of variables such as the choice of reducing metal,[85] the reaction conditions (*i.e.,* annealing temperature and time),[98] the workup conditions,[91] and the morphology of the precursor. As such, variations in the synthetic method, reaction conditions, and precursors between literature reports has led to different H_2 evolution rates for mp-Si NPs (Table 1.2).

Table 1. 2. Summary of H_2 evolution rates and properties of mp-Si photocatalysts prepared under various synthetic conditions.

Precursor	Reducing Agent	Annealing Temperature (°C)	Annealing Time (h)	Surface Area (m^2 g^{-1})	Crystallite Size (nm)	H_2 Evolution Rate (μmol h^{-1} g^{-1})	Reference
$SiCl_4$	NaK	600	0.5	580	2 – 5	882	93
Porous SiO_2	Mg	650	5	337	22	1785	90
Porous SiO_2 (MCM-41)	Mg	800	10	370.9	19.7	604.7	92
Natural Clay	Mg	650	5	308	30 – 35	486	75
Talc Clay	Mg	650	3	188	72	850	70

The motivation for the research presented in this thesis was to systematically investigate how various parameters involved in the synthesis of mp-Si affects its performance as a photocatalyst for H_2 generation *via* water splitting. In Chapter 3, the effect of the reaction conditions (temperature and time) used for magnesiothermic reduction of non-porous, monodisperse SiO_2 on the H_2 evolution rates of mp-Si was investigated. In Chapter 4, porous SiO_2 was used to gain insight into the effects of porosity and surface area. Finally, Chapter 5 presents preliminary results on factors such as the magnesium particle size used for mp-Si synthesis and the addition of a metal cocatalyst. By observing trends in the H_2 evolution rates for various samples characterized by their morphology, crystallinity, and surface chemistry, an improved understanding of the physical and chemical properties of mp-Si and their relation to the photocatalytic activity could be

achieved. Furthermore, this work provides insight into the synthetic conditions needed to optimize the photocatalytic performance of mp-Si.

CHAPTER 2. Experimental Techniques

2.1. Photocatalyst Preparation

2.1.1. Stöber Silica Synthesis

The mp-Si photocatalysts studied in Chapter 3 and Chapter 5 were synthesized using monodisperse, spherical SiO_2 NPs prepared *via* the Stöber sol-gel processing method. In sol-gel processing, precursor molecules form a sol (a stable suspension of colloidal particles) which then forms a gel (a three-dimensional network of sol particles), that becomes a solid material upon removal of the solvent. The precursors are typically metal alkoxides. During the reaction, the precursors polymerize through multiple hydrolysis and condensation reactions.[99] Acid or base catalysts are typically used to enhance the reaction kinetics by producing good leaving groups (acids) or strong nucleophiles (bases) via protonation or deprotonation, respectively.[100] In 1968, Stöber, Fink and Bohn described a sol-gel processing method to synthesize monodisperse spheres of SiO_2 with sizes up to 2 μm in diameter.[101] In their synthesis, now recognized as the Stöber process, tetraethyl orthosilicate (TEOS) is used as the precursor, with ammonium hydroxide (NH_4OH) serving as the catalyst. The growth of SiO_2 particles is governed by two consecutive reactions: 1) hydrolysis of TEOS to form silanol monomers ($Si(OEt)_{4-x}OH_x$) (Eq. 2.1), and 2) condensation of silanol monomers into a siloxane network. Condensation can occur either between two silanol groups (Eq. 2.2) or between a silanol and an unhydrolyzed ethoxy group (Eq. 2.3).[102] The resulting siloxane networks are what form the SiO_2 particles, which can eventually form a gel due to attractive dispersion forces between them. Gels formed from particulate sols are generally reversible and can be re-dispersed by stirring or sonicating (*i.e.,* during washing steps) or by grinding the material after drying.[100]

$$\mathrm{Si(OEt)_4 + H_2O \rightleftharpoons Si(OEt)_3OH + EtO} \quad \text{Eq. 2.1}$$

$$\mathrm{2Si(OEt)_{4-x}(OH)_x \rightleftharpoons (EtO)_{8-2x}(Si-O-Si)(OH)_{2x-2} + H_2O} \quad \text{Eq. 2.2}$$

$$\mathrm{Si(OEt)_4 + Si(OEt)_{4-x}(OH)_x \rightleftharpoons (EtO)_{7-x}(Si-O-Si)(OH)_{x-1} + EtOH} \quad \text{Eq. 2.3}$$

The kinetic balance between the hydrolysis and condensation reactions during the Stöber process is incredibly important in dictating the growth of SiO_2 particles, and therefore their size distribution. In general, for sol-gel reactions, hydrolysis and condensation are influenced by parameters such as the precursor, catalyst, solvent, temperature, pH, and the precursor to water ratio. The rate of hydrolysis is affected by steric and inductive effects of the precursor. For the Stöber process, TEOS provides an adequate balance of steric hindrance and low electron density at the Si atom to achieve monodisperse SiO_2 particles within 24 hours or less. The size of the particles is largely dependent on the reagent concentrations, which dictate the rates of hydrolysis and condensation. However, the relationships between the concentration of a given reagent and the resulting particle size are not necessarily straightforward. For instance, it has been demonstrated that the SiO_2 particle size initially increases with increasing water concentration to a maximum, then decreases as the water content is further increased. This maximum water concentration also depends on the concentrations of TEOS and NH_4OH.[103] Multivariate studies of these reaction parameters (NH_4OH, water, ethanol, and TEOS concentrations) have shown the effects of each variable on particle size to be dependent on each other.[104]

While there is growing understanding of the conditions required to achieve a desired SiO_2 particle size, the detailed mechanisms of nucleation and growth during the Stöber process have yet to be elucidated and have been met with some debate.[102–104] Han

et al. have presented compelling evidence for a growth mechanism occurring over two separate pathways based on their investigation of the reaction kinetics.[102] Their results support a seeded growth model for the Stöber synthesis, where pathway I (nucleation and growth) is dominated by TEOS hydrolysis, and pathway II (the size-enlargement stage) is dominated by condensation. The investigation also revealed the importance of the catalyst concentration (NH_4OH, which strongly affects hydrolysis) on the growth mechanism. Temporal separation of pathways I and II was found to occur only at NH_4OH concentrations ≥ 0.95 M. Below this concentration, the two pathways interweave and result in more loosely condensed siloxane networks within the particles. That is, the NH_4OH concentration seems to influence not only the SiO_2 particle size, but also their internal structure.

In this work, Stöber SiO_2 was prepared by adding 30 mL of TEOS to 700 mL of 95% ethanol (EtOH), followed by 60 mL of 28% ammonia solution (~ 14.8 M NH_4OH). It is important to ensure that the concentration of NH_4OH in the stock solution is correct, since ammonia can easily evaporate from the solution over time. If the stock NH_4OH concentration is too low and not accounted for, the concentration of NH_4OH in the reaction mixture may be less than 0.95 M, resulting in precursors that may alter the performance of mp-Si photocatalysts. As such, when used several months after opening the stock container, the concentration of NH_4OH was determined by titration with hydrochloric acid (HCl), and the volume of ammonia solution added to the reaction was adjusted accordingly. After adding the reagents, the reaction vessel was sealed with parafilm and left to stir for 18 h at 400 rpm. Following the reaction, the white solid (SiO_2 NPs) was collected by centrifuging at 3300 rpm for 25 min. The supernatant was discarded, and the nanoparticles were washed

twice with 100% EtOH to remove any unreacted TEOS. The SiO_2 NPs were dried in an oven overnight at 100 °C.

2.1.2. Magnesiothermic Reduction

All mp-Si photocatalysts investigated in this work were synthesized *via* solid-state magnesiothermic reduction of SiO_2 precursors. The reactions were performed using a programmable single-zone tube furnace under argon atmosphere (Fig. 2.1). The reagents (SiO_2 and Mg powders) were thoroughly ground together in a mortar and pestle to ensure homogenous mixing, then distributed evenly in an alumina reaction boat. The reaction boat was placed in a quartz furnace tube able to withstand high temperatures (up to 1100 °C). The material of the reaction boat was chosen to withstand high temperatures while also avoiding contamination.

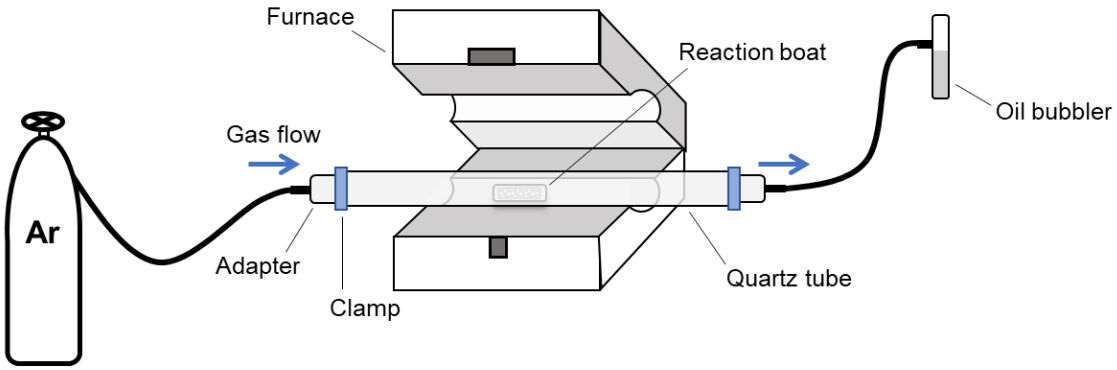

Figure 2. 1. Tube furnace setup for magnesiothermic reduction reactions.

Mg has a melting point of 650 °C and a relatively low vapor pressure of 1 Pa at 428 °C. At temperatures near the Mg melting point (650 °C), Mg vapour reduces SiO_2 to

Si by the reaction shown in Eq. 2.4.[98] The reaction produces polycrystalline Si and the by-product, magnesia (MgO), which can be easily removed by treating it with HCl. In some cases (depending on the reaction conditions and ratio of reagents), the by-products magnesium silicide (Mg_2Si, Eq. 2.5) and magnesium silicate (Mg_2SiO_4, Eq. 2.6) are also formed.[105,106]

$$SiO_2(s) + 2Mg(g) \rightarrow Si(s) + 2MgO(s) \quad \text{Eq. 2.4}$$

$$Si(s) + 2Mg(g) \rightarrow Mg_2Si(s) \quad \text{Eq. 2.5}$$

$$SiO_2(s) + 2MgO(s) \rightarrow Mg_2SiO_4(s) \quad \text{Eq. 2.6}$$

During magnesiothermic reduction, the starting SiO_2 morphology acts as a template for the resulting mp-Si. However, regardless of any porosity in the precursor, mesoporosity in the product is created during the reaction, resulting from the removal of oxygen atoms from the SiO_2 network. Fig. 2.2 illustrates the proposed mechanism for pore formation in mp-Si. The transformation of SiO_2 nanoparticles to mp-Si is thought to occur from the surface to the core.[87] As Mg diffuses through and reacts with the solid SiO_2, it leaves behind Si crystallites and MgO interwoven into a composite product. Depending on the reaction conditions (ratio of SiO_2:Mg, reaction temperature, Mg and SiO_2 particle size), other by-products such as Mg_2Si, may also form within the composite.[87] Once the product is cooled, etching with HCl removes the MgO (Eq. 2.7) resulting in the remaining sponge-like mp-Si structure.

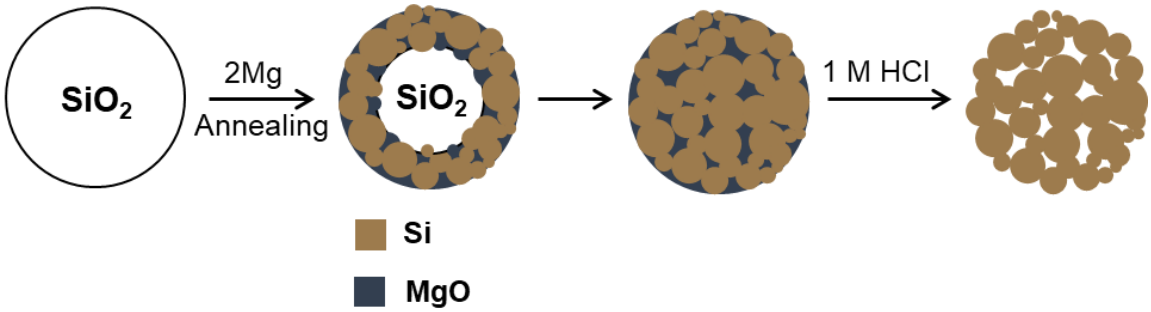

Figure 2. 2. Illustration depicting the process of magnesiothermic reduction to produce mp-Si.

$$\mathrm{MgO}(s) + 2\mathrm{HCl}(aq) \rightarrow \mathrm{MgCl_2}(aq) + \mathrm{H_2O}(l) \qquad \text{Eq. 2.7}$$

While relatively easy to perform, magnesiothermic reduction is a complex reaction in that there are several reaction parameters that can influence the resulting product. Both the characteristics of the reagents (morphology of the SiO_2 precursor, particle sizes and stoichiometry), and the reaction conditions (ramp rate, temperature and reaction time) have tunable aspects that will dramatically affect the characteristics of mp-Si formed. The reaction conditions of magnesiothermic reduction (namely, the temperature and time) are key factors in determining characteristics such as the crystallinity and surface structure of mp-Si. Most magnesiothermic reduction reactions are held at least as high as 650 °C to enhance atom diffusion and ensure complete reduction. Higher temperatures generally lead to larger crystallites and to larger pores.[87]

Metallothermic reductions are highly exothermic reactions. For the magnesiothermic reduction of SiO_2, in situ reaction temperatures have been found to reach up to 1000 °C and above.[105,107] Such excessively high temperatures can lead to large amounts of sintering and morphological damage in mp-Si when the reaction is heated to

650 °C, even when the reaction is held just long enough to reach completion.[89] To mediate this, thermally stable and inert salts have been used as heat sinks for magnesiothermic reduction reactions.[108–111] However, these increase the cost of synthesis and may introduce contamination. Another method to control the exothermic nature of magnesiothermic reduction involves first heating to the initiation temperature (650 ºC), then lowering it (below the Mg melting point) for a longer duration to maintain the reaction until completion. This two-step heating method has been demonstrated to reduce morphological damage, while leading to mp-Si with higher surface areas.[89]

The mp-Si NPs in this work were prepared using a stoichiometric ratio of 2.2:1 Mg:SiO_2. The reactions were annealed using either the conventional single temperature heating method at 650 °C or the two-temperature heating method described above. For the two-temperature heating process, the reactions were held at 650 °C for 0.5 h, then air-cooled and held at a predetermined temperature (100, 200 or 300 °C) for 6 h. For all reactions, the ramp rate was 10 °C min^{-1}. After the reactions were completed and cooled to room temperature, the resulting product was treated with 25 mL of 1.0 M HCl for 4 h with stirring at 300 rpm. The solid was collected by suction filtration and washed with 150 mL of distilled water, then dried overnight in an oven at 100 °C.

2.2. Characterization Techniques

2.2.1. Powder X-Ray Diffraction

Powder X-ray diffraction (XRD) is one of the most routinely used methods for characterizing solid materials. The non-destructive technique works by irradiating the sample with a monochromatic beam of X-rays. By using X-ray wavelengths comparable to the interatomic spacing of crystalline solids, the composition and phase of a material can

be analyzed through an elastic scattering process.[112] An X-ray diffractometer has three main components: an X-ray source, a sample holder and a detector (Fig. 2.3A). The X-ray source and detector rotate together on a goniometer with the sample holder in the centre.[113] Incoming X-rays irradiate the sample at an angle, θ, and the detector collects diffraction data within the angle 2θ (the angle between the refracted X-ray and the incident X-ray path).

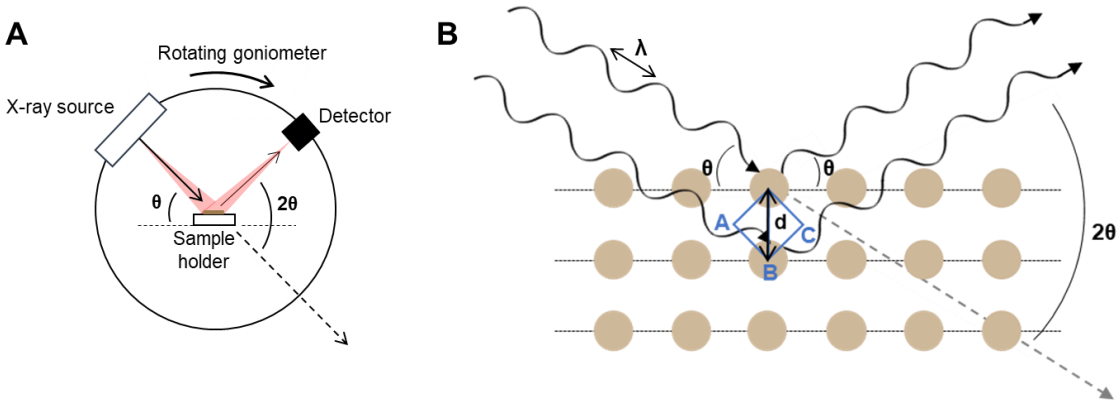

Figure 2. 3. (A) Configuration of an X-ray diffractometer. (B) Schematic depicting a set of crystal planes giving a diffraction signal according to Bragg's Law.

During XRD analysis, incoming X-rays with wavelength, λ, and incident angle, θ, interact with the sample through elastic scattering. The diffraction signals in the spectrum are generated through the constructive interference of refracted X-rays, which occurs only for a set of crystal planes satisfying Bragg's Law (Eq. 2.9).[112] Fig. 2.3B depicts a set of crystal planes giving rise to a diffraction signal. For two lattice planes separated by a distance, *d*, an X-ray diffracted from the lower plane must travel an extra distance (distance AB + BC in Fig. 2.3B) from the source to the detector compared to an X-ray diffracted

from the first plane. Therefore, for the diffracted beams to remain in phase and constructive interference to occur (giving a signal in the XRD spectrum), AB + BC must equal some integer of the wavelength (Eq. 2.8). According to Fig. 2.3B, the distances AB and CD are each equivalent to $d\sin\theta$. This relation gives rise to Bragg's Law (Eq. 2.9).

$$\mathrm{AB} + \mathrm{BC} = n\lambda \qquad \text{Eq. 2.8}$$

$$n\lambda = 2d\sin\theta \qquad \text{Eq. 2.9}$$

Each peak in an XRD spectrum corresponds to a set of lattice planes. As such, crystalline materials give sharp XRD peaks, while amorphous materials (lacking long range order) result in a broad peak in the spectrum.[112] The materials in this work were characterized using a Rigaku Ultima IV X-ray diffractometer with Cu Kα radiation (λ = 1.54). To generate X-rays, electrons are thermally generated in a cathode ray tube, then accelerated towards the anode target (Cu), causing the emission of core electrons. X-Rays of a corresponding wavelength are emitted as valence electrons in the anode relax to the vacant core states.[112] A monochromator filters out unwanted wavelengths such that only the Kα line is used for analysis.[113] In this work, samples were prepared for analysis by placing them on a zero-background Si wafer, and XRD spectra were collected at 3 counts per second.

2.2.2. Electron Microscopy

Electron microscopy is an imperative tool for the characterization of nanomaterials. In traditional light microscopy, visible light is used to view specimens on the micrometre scale. The resolution of a microscope is on the order of the wavelength of the light that is

used to view the specimen. In order to view specimens on the nanometre scale, electrons with a well-defined de Broglie wavelength are used in place of photons. The resolving power of electron microscopes can be controlled by changing the accelerating voltage (the electron velocity, *v*) according to the de Broglie relation (Eq. 2.10) where λ is the electron's de Broglie wavelength, *p* is its momentum, *m* is its mass and *h* is Planck's constant. Unlike light microscopes which use glass lenses to focus light onto the specimen, electron microscopes contain electromagnetic "lenses" to guide the electrons into a focussed beam.[114] Instead of visible light, electrons are emitted from an electron gun. Electron guns in electron microscopes can be either thermionic emitters or field emitters, which use heat or electric fields, respectively, to eject electrons from the source material.[115]

$$\lambda = \frac{h}{p} = \frac{h}{mv} \qquad \text{Eq. 2.10}$$

To understand electron microscopy, it is important to define the concepts of elastic and inelastic scattering. In elastic scattering events there is no loss in energy. Therefore, elastically scattered electrons can change direction, but do not change their wavelength. Inelastic scattering is accompanied by an energy loss (and increase in wavelength) which can occur through a variety of mechanisms. Scattering in electron microscopy is dictated by factors such as the specimen thickness, interaction volume and electron transparency. For instance, in thick specimens (with a longer electron path) electrons are more likely to experience scattering events. Scanning electron microscopy (SEM) is typically used to analyze thicker samples which primarily scatter electrons rather than transmit them. On the other hand, transmission electron microscopy (TEM) is restricted to thin specimens (less than 1 μm) which allow electrons to pass through the sample. Specimens which allow

incident electrons to pass through without scattering are called “electron transparent.” This depends on both the kinetic energy of the incident electrons and the chemical composition of the specimen, as heavier elements will have stronger electron interactions.[114]

Transmission Electron Microscopy.

TEM instruments have a similar configuration to a traditional light microscope (Fig. 2.4), which permits a two-dimensional projection of the specimen produced by electrons transmitted through the sample. The electron gun accelerates electrons at a high voltage (80 – 300 kV) which are directed down the column of the microscope by a positively charged anode. The microscope column is kept under vacuum as to not interfere with electron movement or scattering. Electromagnetic condenser lenses focus the electrons into a beam which passes through the sample. The objective lens then focuses the transmitted electrons to form a diffraction pattern, which is magnified by projector lenses onto the detection system and translated into an image.[114]

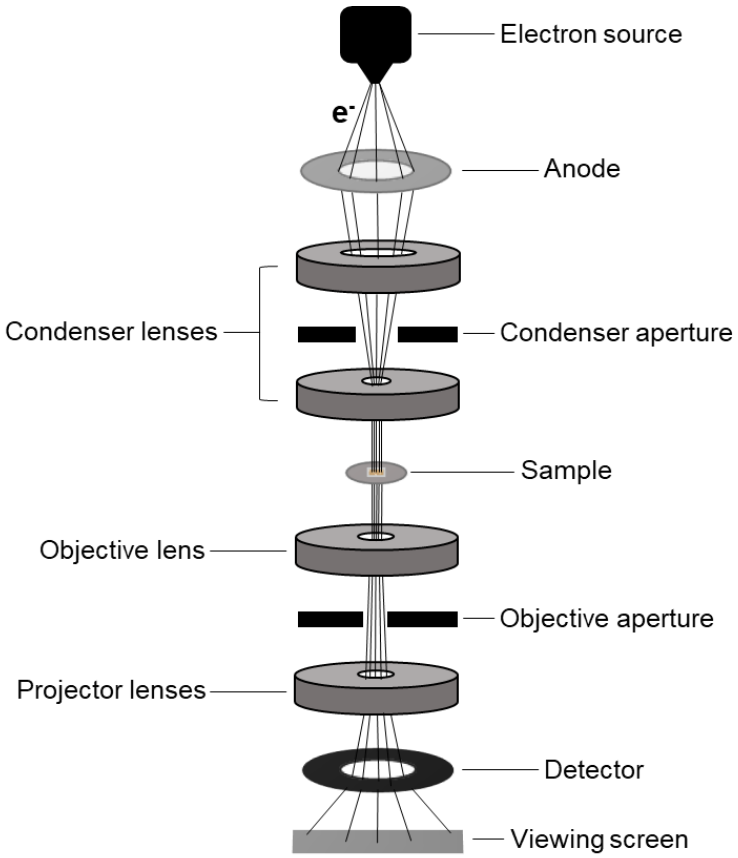

Figure 2. 4. Core components of a transmission electron microscope.

Various imaging modes are available in TEM, with one of the most common being the brightfield (BF) imaging mode. In BF imaging, scattered electrons are blocked using an objective aperture (Fig. 2.5) and the image is generated using only non-scattered electrons. Areas of the sample where many electrons are being scattered (such as areas of higher thickness or mass) have fewer transmitted electrons and therefore appear darker in the image.[114]

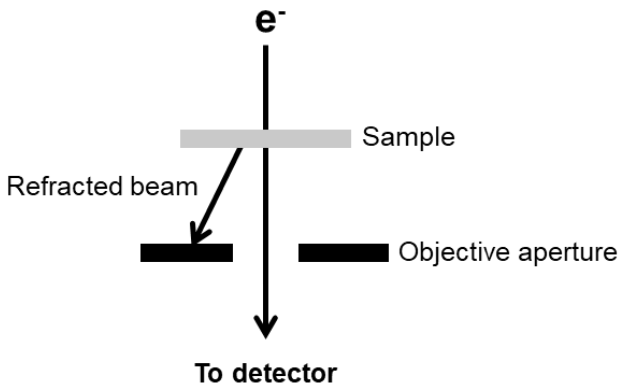

Figure 2. 5. Use of an objective aperture for BF imaging by TEM.

In high-resolution TEM (HRTEM), rather than using an aperture to block either the transmitted or refracted beams, multiple beams are allowed to interact. For crystalline materials, recombination of the transmitted and refracted beams generates an interference pattern that reveals the periodic nature of the crystal. For ultrathin specimens at high enough magnification, these diffraction patterns correspond to atom positions, allowing for the observation of lattice spacings and grain boundaries.[114]

In this work, SiO_2 and mp-Si NPs were characterized using a FEI Titan 80-300 TEM at an operating voltage of 300 kV. The instrument is equipped with a Schottky (thermally-assisted) field emitter, which uses a combination of heat and electric fields to trigger electron emission. Charged coupled device (CCD) cameras translate the transmitted electron signal to an image. HRTEM was used to visualize the lattice planes and measure the crystallite size of the mp-Si samples. Ethanolic suspensions of NPs were drop cast onto a carbon coated copper TEM grid to prepare the samples for imaging.

Scanning Electron Microscopy.

Scanning electron microscopy (SEM) was used to gain topographical and size information for the nanomaterials prepared in this work. SEM differs from TEM in that the incident electrons are scattered back from the sample and detected, rather than passing through. The general setup of a SEM instrument is shown in Fig. 2.6. The SEM chamber is held under vacuum at pressures of 0.1 – 10^{-4} Pa. The electron gun accelerates electrons through 1 – 30 kV accelerating voltage (selected prior to imaging), which influences the depth of electron penetration.[114] Also set prior to analysis are the emission current (probe current) and the working distance (the distance between the sample surface and the objective lens).[115] Electrons released from the source first pass through the anode, which helps to align the electrons into a beam and accelerate them towards the sample stage. Electromagnetic condenser and objective lenses are both situated above the stage and work in tandem to finely focus the electron beam onto the specimen. The beam is directed to scan the sample surface by scan coils, which deflect the beam in the x and y directions.[116] When the incident electrons reach the sample surface, a number of different processes can occur. Most importantly are the release of secondary electrons (SEs) and back-scattered electrons (BSEs) which are detected by SE and BSE detectors, respectively. Secondary electrons are scattered electrons resulting from inelastic interactions between the electron beam and the sample. They typically originate from shallow surface regions of the sample and are important for gaining topographical information at the highest resolution (typically ~100 Å).[117] Contrarily, backscattered electrons are a result of elastic interactions with atomic nuclei that cause a reflection of the incident beam. Larger atoms (with larger nuclei) result in a more intense reflection, thus appearing brighter in the image. As such, BSE

detection can be useful for providing qualitative elemental contrast.[116] Most SEMs are equipped with multiple detectors which allow for various imaging modes. The placement of SE and BSE detectors shown in Fig. 2.6 allow them to detect the scattered and reflected electrons, respectively. Signals from each detector are sent to a computer which generates a raster depicting a three-dimensional image of the specimen.

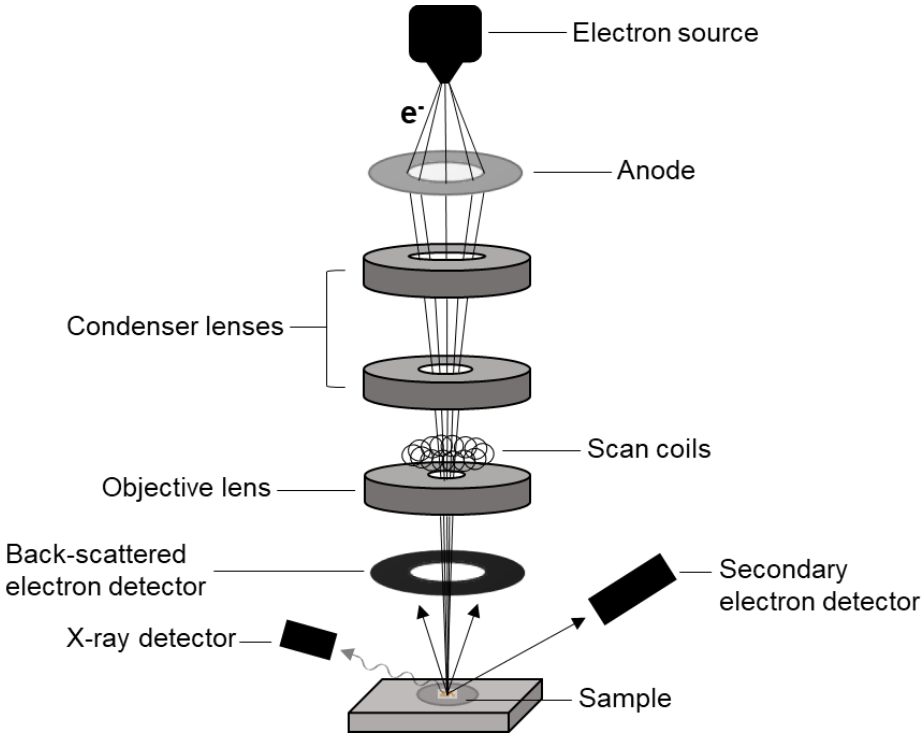

Figure 2. 6. Core components of a scanning electron microscope.

The mp-Si NPs and precursors in this work were imaged using a Hitachi S-4700 field emission SEM (FESEM). FESEMs contain a field emission gun (FEG, or "cold cathode field emitter") as the electron source, allowing electrons to be generated without heating. Instead, the FEG releases electrons by applying a high electric field near the

filament tip.[115] The samples in this work were imaged without applying any coating, which was sufficient to obtain images revealing size and topographical information, as well as to perform EDS analysis on the mp-Si samples (see section 2.2.3). To prepare the samples, NPs were dispersed in acetone by sonication, then drop cast onto a silicon wafer mounted to the SEM stub. The images were collected at an accelerating voltage of 3.0 – 5.0 kV, an emission current of 14 – 16 μA and a 7 – 9 mm working distance (depending on the sample and desired information).

2.2.3. Energy-Dispersive X-Ray Spectroscopy

Energy-dispersive X-ray spectroscopy (EDS) analysis was performed on the mp-Si samples using either a JEOL JSM-7000F (Chapter 3) or Hitachi S-4700 (Chapters 4 and 5) SEM instrument equipped with an Oxford Instruments X-Max EDS detector. Quantitative results for the elemental analysis were recorded in atomic percent. Representative images and associated data from EDS analysis are shown in Figs. A1 – A3 (Appendix A). The data was normalized to include only Si and O.

EDS is used in conjunction with SEM or TEM for elemental analysis or chemical characterization of a sample. The emission of characteristic X-rays by atoms occurs when the primary electron beam from the microscope knocks out an inner-shell (usually a K or L shell) electron from the sample, leaving a vacancy (Fig. 2.7). This triggers an outer-shell electron to jump from a higher to lower energy state to fill the vacancy, resulting in a release of energy (X-rays).[116] Detection of the X-rays emitted allows for both qualitative and quantitative analysis of the elemental composition, which can be given in the form of point spectra or elemental maps. X-rays are produced within a region about 1 μm deep into the specimen.[114]

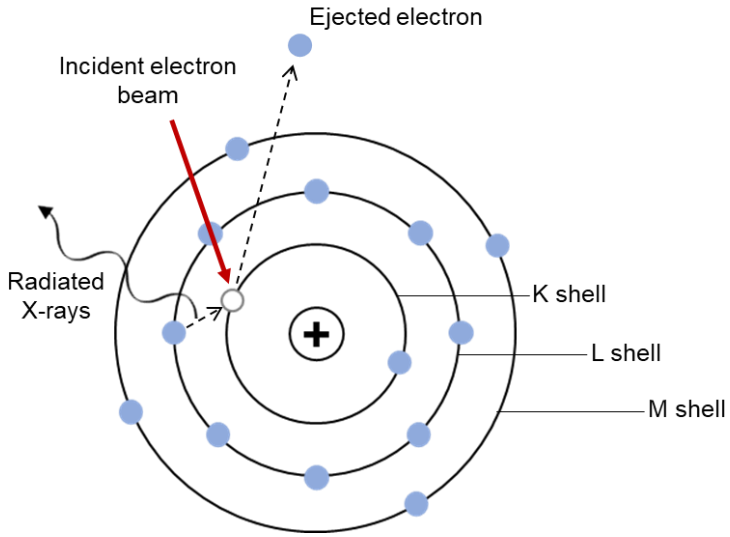

Figure 2. 7. Emission of characteristic X-rays from an atom during EDS analysis.

2.2.4. Raman Spectroscopy

Raman spectroscopy is a vibrational spectroscopic technique based on the inelastic scattering of photons by matter. When a sample is irradiated with monochromatic visible light, most of it is either absorbed or transmitted, while a small proportion of the radiation is scattered in all directions. Scattering occurs when incident light interacts with a material and induces a vibrational transition to an intermediate "virtual" energy state (Fig. 2.8). Following this transition, the material instantaneously relaxes, causing the emission of a photon (the scattered light). In most cases, the frequency of the scattered photon (ν_s) is equal to that of the incident photon (ν_i). These elastic scattering events are called Rayleigh scattering. Less often, Raman scattering results from a change in frequency of the emitted photon ($\nu_s \neq \nu_i$), either by a loss (Stokes scatter) or gain (anti-Stokes scatter) of energy. The processes of Stokes and anti-Stokes Raman scattering are illustrated in Fig. 2.8. In Stokes scattering, the vibrationally excited molecule falls to an excited state above the ground

state, resulting in a lesser amount of energy released. In anti-Stokes scattering, the incident light interacts with and promotes a molecule that is already vibrationally excited. The excess energy is then released upon return to the ground state.[118]

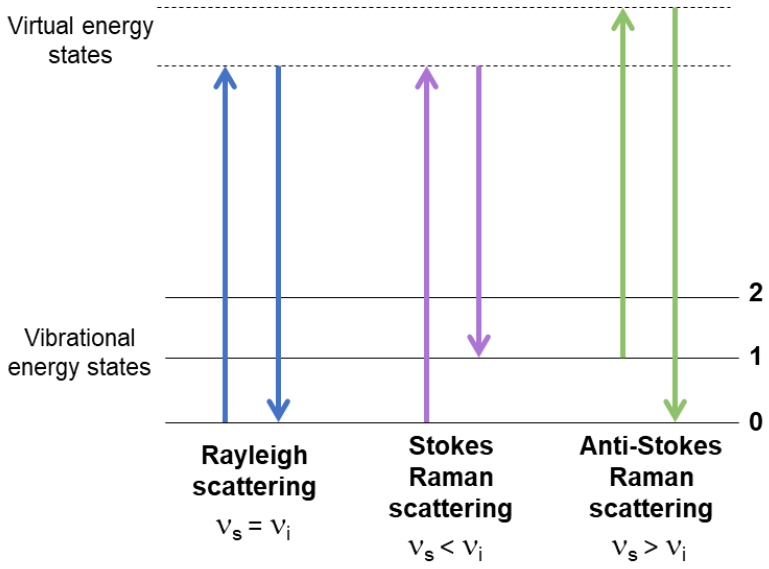

Figure 2. 8. Energy level diagram depicting Rayleigh and Raman scattering.

In Raman spectroscopy, Raman scattering is detected as the sample is irradiated with laser light of a chosen wavelength. The Raman shift, which represents the shift in wavenumber from the incident photon, is plotted against the intensity of the spectral lines. Since (at room temperature) molecules exist most commonly in the ground state than in excited vibrational states, Stokes lines have a higher intensity in the Raman spectrum than anti-Stokes lines. Fig. 2.9 depicts a simplified configuration of a Raman system. The system consists of three main components: a laser source, optics for focussing and collecting incident and scattered radiation, and a spectrometer. The laser first passes

through a filter to eliminate extraneous radiation, then a set of mirrors and/or lenses focusses the laser light onto the specimen. Raman scattered radiation is filtered out from the incident beam and focused into the entrance slit of the spectrometer, containing a grating and CCD detector.[118]

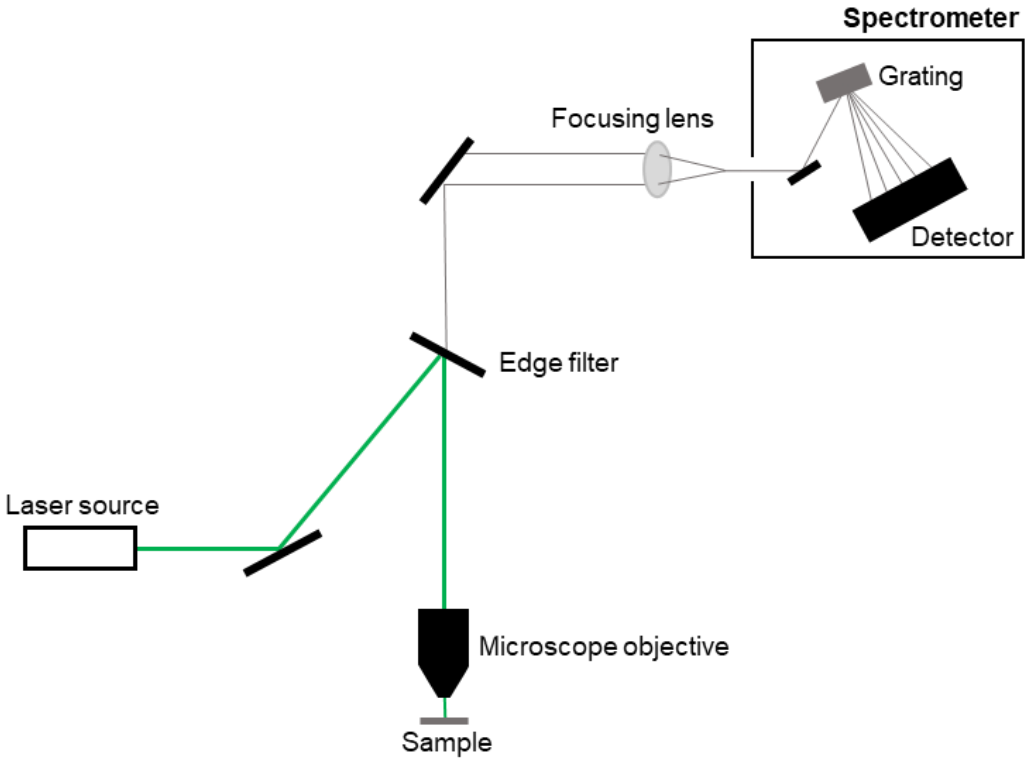

Figure 2. 9. Basic components and configuration of a typical Raman instrument.

The Raman spectrum of a material provides a molecular fingerprint with peaks correlating to various Raman active vibrational modes. The vibrational modes in a molecule are dependent on the orientation of atoms and bonds (*i.e.,* the molecular symmetry), atomic masses, bond order, and hydrogen bonding. The intensity of Raman scattering is directly related to the polarizability of the molecule. Therefore, for a molecular

vibration to be Raman active (having a detectable Raman scatter), the molecule must undergo a increase in polarizability during the vibration, which allows the electromagnetic field of incident radiation to temporarily distort the electron cloud.[118] The appearance of vibrational modes in a Raman spectrum also depends on the degree of chemical interaction between molecules. For instance, Raman scattering by optical phonons can occur in solid crystalline materials with long range translational symmetry. Raman spectroscopy can therefore be a useful tool in distinguishing between crystalline and amorphous solids of the same chemical composition. For amorphous solids lacking in translational symmetry, numerous variations in bond angles and lengths produces a distribution of states with slightly varying vibrational energies, thereby broadening and/or shifting the peaks in the Raman spectrum.[119]

In this work, Raman spectroscopy was used to observe differences in the degree of crystallinity between mp-Si samples. The Raman spectrum of monocrystalline Si has a sharp peak centred at 520 cm^{-1} corresponding to the Si-Si transverse optical phonon mode.[120] As the degree of crystallinity decreases, the confinement of optical phonons within crystallites and the widened distribution of states causes the peak to be broadened and shifted to lower wavenumbers.[120,121] Raman spectroscopy was conducted using a Jobin-Yvon T64000 Raman system with 532 nm laser excitation. The spectra were collected through a 50 × long working distance objective, with a power of 10 mW at the sample.

2.2.5. X-Ray Photoelectron Spectroscopy

X-Ray photoelectron spectroscopy (XPS) is a surface-sensitive characterization technique based on the photoelectric effect. The typical configuration for XPS

instrumentation consisting of an X-ray source, electron optics, and detection system is shown in Fig. 2.10. The system is housed under vacuum to prevent excess scattering of electrons and to keep the sample surface clean. The X-ray source consists of a heated tungsten or LaB_6 filament from which electrons are accelerated towards a metal anode to generate X-rays.[122]

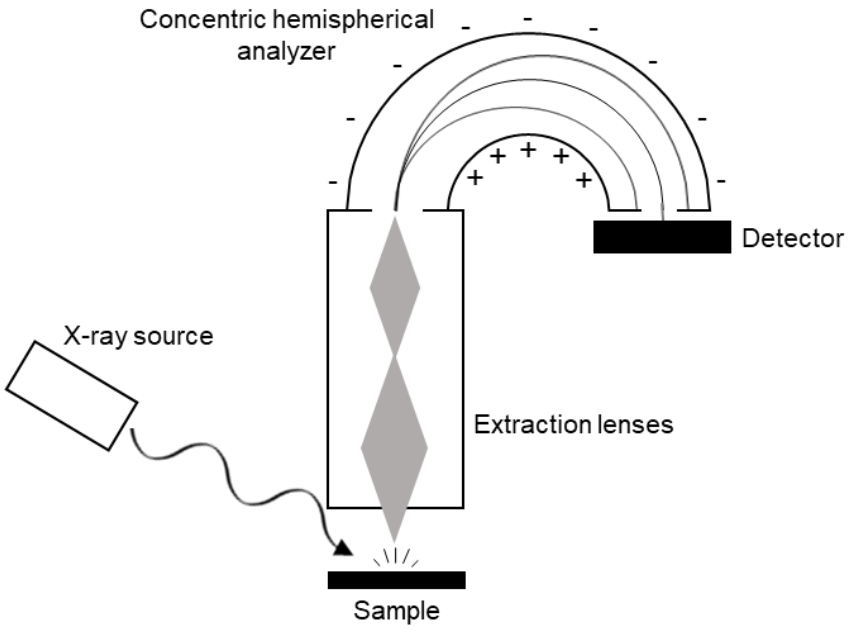

Figure 2. 10. Core components of an X-ray photoelectron spectrophotometer.

When X-rays penetrate the sample, their energy is transferred to a core electron, resulting in ejection after it overcomes the binding energy (the energy difference between the core level and the Fermi level) and the material work function, becoming a free electron as it reaches the vacuum level (Fig. 2.11A). The generated photoelectrons travel through a set of electron optics to the detection system, which measures their kinetic energy, E_k. Due

to conservation of energy, the binding energy (BE) of an electron reaching the detection system can be determined according to Eq. 2.11,[122]

$$BE = h\nu - \phi_{spec} - E_k \qquad \text{Eq. 2.11}$$

where $h\nu$ is the energy of the incoming X-ray, ϕ_{spec} is the spectrometer work function (a constant value determined by calibration) and E_k is the kinetic energy of the electron measured by the spectrometer. For solid samples, the BE is measured with respect to the sample Fermi level, which for conducting materials is aligned to that of the spectrometer (Fig. 2.11A).[122–124] Therefore, the work function of the spectrometer can considered in the BE equation without needing to know the work function of the sample material.

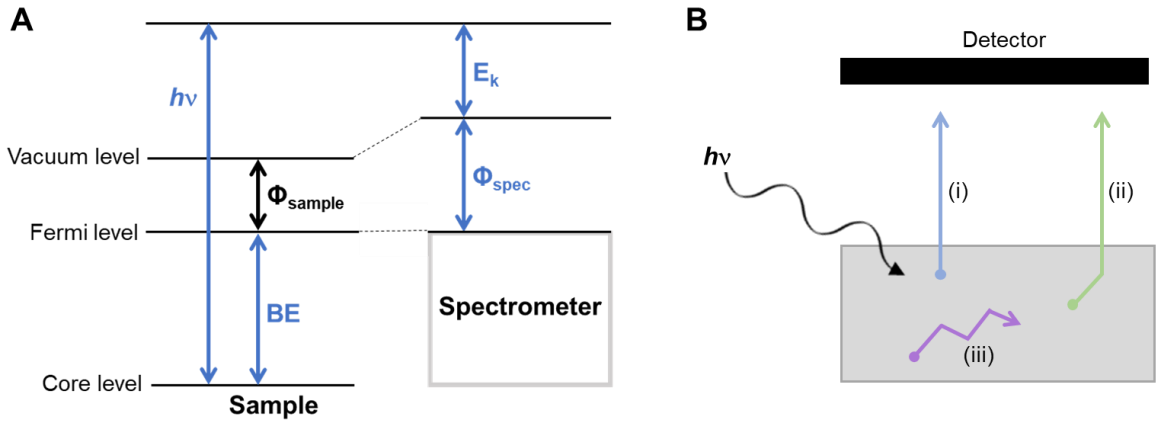

Figure 2. 11. (A) Energy level diagram for a sample in good electrical contact with the XP spectrometer. The terms of the binding energy equation are indicated in blue. (B) Schematic depicting the possible interactions of photoelectrons with the sample upon X-ray irradiation. Photoelectrons near the surface reach the detector without inelastic scattering (i) or encounter one or two collisions, leaving the sample with a slightly lower E_k (ii). Photoelectrons deeper in the sample lose their energy through inelastic collisions (iii).

The BE of an electron is a material property influenced by the atom's chemical environment (*i.e.,* oxidation state and nearest neighbours). As such, XPS can be a useful tool for probing the chemical composition of material surfaces. XPS is considered a surface sensitive technique, since, although X-rays can typically penetrate a sample up to a few μm, photoelectrons generated within deeper regions of the sample will lose most or all their energy through inelastic collisions before escaping the sample (Fig. 2.11B). Therefore, only electrons reaching the detector without losing energy will contribute to the characteristic peaks in an XP spectrum. Some electrons closer to the surface will encounter only one or two inelastic collisions and leave the sample with a slightly lower E_k, giving rise to the step-like background contributions seen in most XPS spectra.[122]

The probability of photoelectron escape (roughly equivalent to the probability of XPS detection) for a detection angle of 90 ° can be calculated according to Eq. 2.12,[125]

$$\mathrm{P}(d) = \exp\left(-d/\lambda\right) \qquad \text{Eq. 2.12}$$

where P(d) represents the likelihood of an electron reaching the detector without being inelastically scattered for an atom at a distance, d, from the sample surface. The inelastic mean free path, λ, is a measure of the average distance travelled by a photoelectron before it is inelastically scattered and depends on both the material and the irradiating energy. According to Eq. 2.12, about 95% of all detected electrons come from within 3λ of the surface, usually about 10 nm or less.[122]

During an XPS experiment, photoelectrons escaping the sample move through a set of electron optics (called extraction lenses) which direct them to a concentric hemispherical analyzer (CHA).[122] To improve resolution, the kinetic energy of the electrons is reduced

by a retardation voltage to a specific energy (defined by the user) called the pass energy. Voltages are applied to the CHA such that the outer hemisphere has a more negative potential with respect to the inner hemisphere, creating a potential difference which guides the electrons through the analyzer. Only electrons having the specified pass energy will follow the curved flight path through the centre of the analyzer and reach the detector. For a typical XPS experiment, the pass energy is held constant in order to keep a constant energy resolution, and the retardation voltage is scanned to cover the desired E_k range.[124]

In the XPS spectrum, photoelectron peaks are notated by the element and the orbital from which the electrons were ejected. All XPS lines, except those from s orbitals, occur as doublets due to spin-orbit coupling and are notated with the j quantum number. For instance, a Si 2p high-resolution spectrum contains a $2p_{1/2}$ peak and a $2p_{3/2}$ peak. In this work, XPS was conducted on mp-Si samples with a ThermoVGScientific Multilab 2000 XPS using Al Kα radiation. The high-resolution spectra were recorded with a pass energy of 30 eV in 0.1 eV steps. The XP spectra were fitted on CasaXPS software using Shirley background subtraction. Calibration was performed using the C1s peak (285 eV).

2.2.6. Optical Bandgap Determination using UV-Vis Spectroscopy

In ultraviolet-visible (UV-vis) spectroscopy, light absorption of a sample is measured as a function of wavelength. The typical configuration of a single-beam UV-vis spectrometer is shown in Fig. 2.12. Radiation from the light source passes through a monochromator, which selects the desired wavelength to irradiate the sample. The detector then measures the intensity of light transmitted. The absorbance (A) of the sample is related to the transmittance (T) according to the Beer-Lambert law (Eq. 2.13), where I and I_o are the intensities of the transmitted and incident beams, respectively. The absorbance is also

directly proportional to the concentration of the absorbing species (c) and the path length (l) of light through the sample (Eq. 2.13). The molar absorptivity constant, ε, has the units of L mol^{-1} cm^{-1}.[126]

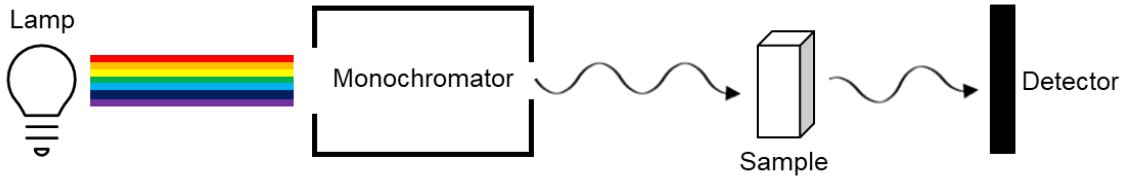

Figure 2. 12. Core components of a UV-vis spectrophotometer.

$$A = -\log T = -\log \frac{I}{I_o} = \varepsilon l c \qquad \text{Eq. 2.13}$$

According to the Beer-Lambert law, the absorption coefficient (α) of a material is a measure of the rate of decrease in the intensity of transmitted radiation and can be expressed by Eq. 2.14.

$$I = I_o \exp\left(-\alpha/t\right) \qquad \text{Eq. 2.14}$$

For semiconductor materials, the optical absorption coefficient, α, when the energy of incident radiation is less than that of the bandgap has a value of zero (Eq. 2.15).[127] Therefore, the ideal UV-vis spectrum for a direct bandgap semiconductor should exhibit almost no absorption when the energy of incident photons is below the bandgap, and a sharp increase in absorption for photons with energies above the bandgap. Real spectra exhibit a nonlinear increase in absorption that reflects the local density of states at the

valence band minimum and conduction band maximum.[128,129] In other words, the absorbance is not directly proportional to the increase in photon energy ($h\nu$).

Based on semi-classical descriptions of optical absorption in semiconductors, the optical absorption coefficient of a direct bandgap semiconductor is expected to act according to Eq. 2.16, which states that when $h\nu$ is greater or equal to the bandgap energy (E_g), α is proportional to $(h\nu - E_g)^{1/2}$. For an indirect bandgap semiconductor, when $h\nu \geq E_g$, α is proportional to $(h\nu \pm \hbar\Omega - E_g)^2$ (Eq. 2.17). The term $\hbar\Omega$ denotes the energy of a phonon being emitted or absorbed. In most cases, this contribution is negligible and can be disregarded.[127] It follows that α can be expressed by the Tauc relation (Eq. 2.18), where B is a proportionality constant and γ is a factor dependent on the nature of the electronic transition (1/2 and 2 for direct and indirect semiconductors, respectively).[130] The proportional relationship given by the Tauc relation allows for the determination of E_g by linear extrapolation when $(\alpha h\nu)^{1/\gamma}$ is plotted against $h\nu$.

$$\alpha(h\nu < E_g) = 0 \qquad \text{Eq. 2.15}$$

$$\alpha_{dir}(h\nu \geq E_g) \propto (h\nu - E_g)^{1/2} \qquad \text{Eq. 2.16}$$

$$\alpha_{ind}(h\nu \geq E_g) \propto (h\nu \pm \hbar\Omega - E_g)^2 \qquad \text{Eq. 2.17}$$

$$(\alpha h\nu)^{1/\gamma} = B(h\nu - E_g) \qquad \text{Eq. 2.18}$$

The optical band gaps for the mp-Si NPs in this work were estimated from Tauc plots obtained from UV-vis absorption spectra. UV-vis spectra were recorded on a Varian Cary 100 Bio spectrophotometer. The Tauc plots were generated by first converting absorbance (A) at each wavelength to the absorption coefficient (α) according to the Beer-Lambert law (Eq. 2.19). The wavelength (in nm) is converted to energy using Eq. 2.20,

which can be simplified to Eq. 2.21 to obtain units in eV. The data was plotted with $h\nu$ on the abscissa and $(\alpha h\nu)^{1/2}$ on the ordinate. The bandgap energy is estimated by extrapolating the linear region to y = 0.

$$\alpha = \ln(10) \times A \quad \text{Eq. 2.19}$$

$$h\nu = \frac{hc}{\lambda} \quad \text{Eq. 2.20}$$

$$h\nu\ (\text{eV}) = \frac{1240\ (\text{eV nm})}{\lambda\ (\text{nm})} \quad \text{Eq. 2.21}$$

2.2.7. Brunauer-Emmett-Teller Specific Surface Area

The specific surface areas (SSAs) of mp-Si NPs and precursors in Chapter 4 of this work were determined using the Brunauer-Emmett-Teller (BET) method with nitrogen (N_2) adsorption measurements. The BET theory is an extension of the Langmuir theory of gas adsorption on solid surfaces. According to the Langmuir theory, monolayer adsorption of adsorbates (gas molecules) can be related to the gas pressure above the solid surface at a fixed temperature by Eq. 2.22,[131]

$$\theta = \frac{\alpha p}{1 + \alpha p} \quad \text{Eq. 2.22}$$

where θ is the fractional coverage of the surface, p is the gas pressure and α is the Langmuir binding constant at dynamic equilibrium. This relation depends on the assumptions that adsorption on the solid surface is restricted to one monolayer, and that both the gas phase and adsorbed phase behave ideally. In other words, there are no intermolecular interactions and all surface sites are assumed have the same adsorption energy for the adsorbate.[131] The

system is considered to reach dynamic equilibrium when the rates of adsorption and desorption are equal.[132,133] The BET theory expands on the Langmuir theory by including multilayer adsorption in the description.[134] The theory is based on the following assumptions (in addition to those of the Langmuir theory): 1) gas molecules will physically adsorb on a solid surface in infinite layers, 2) there is no interlayer interaction, and 3) the theory can be applied to each layer.[135]

A schematic for a typical surface area analyzer is shown in Fig. 2.13.[136] Prior to the analysis, the sample (of known mass) is cleaned of adsorbed contaminants through a process called degassing under vacuum or inert gas and at high temperature. The temperature and degassing time must be selected as to sufficiently remove contaminants without damaging the sample. To obtain measurable adsorption, the analysis must be done at low temperatures (*i.e.,* 77 K for nitrogen adsorption). After degassing, the sample is moved to the analysis port which is cooled and maintained at constant temperature using a dewar of liquid N_2. The adsorbate is then released stepwise into the sample cell at pre-determined relative pressures (p/p_o) using a calibrated piston that controls the injection volume. At each step, the system is allowed to equilibrate, and the volume adsorbed is recorded. N_2 is a commonly used adsorbate due to its availability in high purity and ability to interact with most solid surfaces. Helium gas (which does not adsorb to the sample surface) is also typically used for calibration.[136]

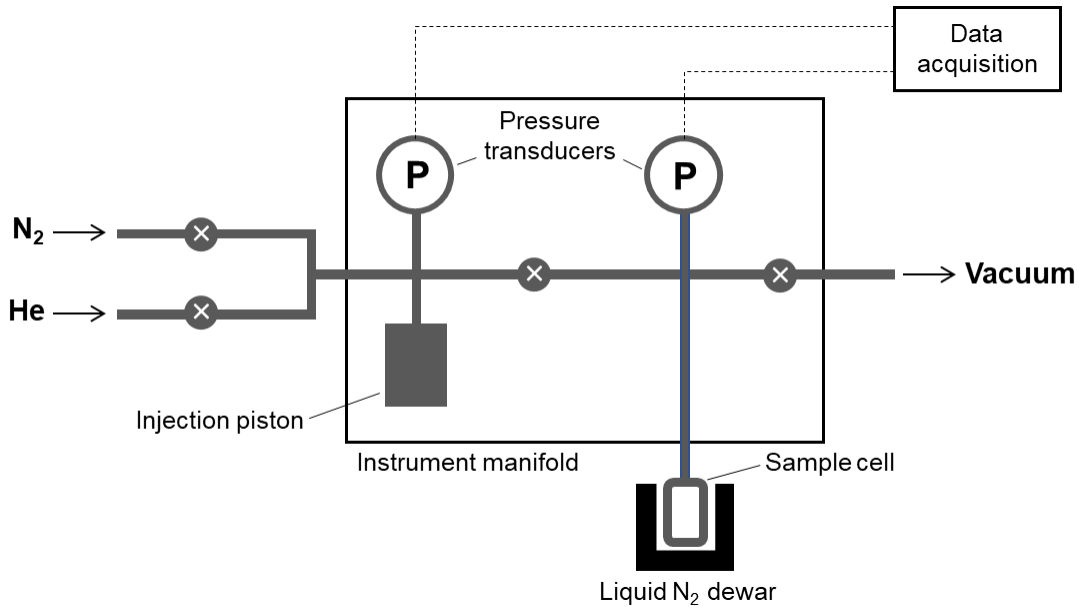

Figure 2. 13. Instrumentation for surface area analysis by nitrogen adsorption.

The majority of physisorption isotherms fit into one of the six classifications shown in Fig. 2.14A, which depend on the morphology and adsorption energy of the solid surface.[137] Some isotherm types are also characterized by hysteresis loops (Fig. 2.14B) which are usually related to capillary condensation in mesoporous materials. The type of hysteresis is thought to be indicative of the pore morphology. Of the isotherm classifications, Type I isotherms (also referred to as Langmuir isotherms) depict monolayer adsorption only and are seen for microporous materials. Type II isotherms are suitable for either non-porous or microporous materials where multilayer adsorption occurs at higher relative pressures. Type III isotherms may occur when the adsorption capacity is low. These curves have no region corresponding to monolayer formation and cannot be treated using BET analysis. Type IV isotherms are common for mesoporous solids and are characterized by a hysteresis loop (Fig. 2.14B) and saturation plateau. At low relative

pressures, the formation of a monolayer occurs, followed by mesopore filling (capillary condensation) corresponding to a steep increase in the adsorbed volume as the pressure is increased. The isotherm plateaus once the mesopores are filled and adsorption continues on the external surface (Fig. 2.15A). Type V isotherms are similar to Type III and occur for mesoporous solids with low adsorption capacity. The final isotherm, Type VI, depicts step-wise multilayer adsorption and appears for surfaces containing different types of adsorption sites with energetically different characteristics.[137] Type IV isotherms were observed for the materials characterized in this work, since they are mesoporous in nature. A more detailed depiction of a Type IV isotherm and the processes occurring at each step is shown in Fig. 2.15A.

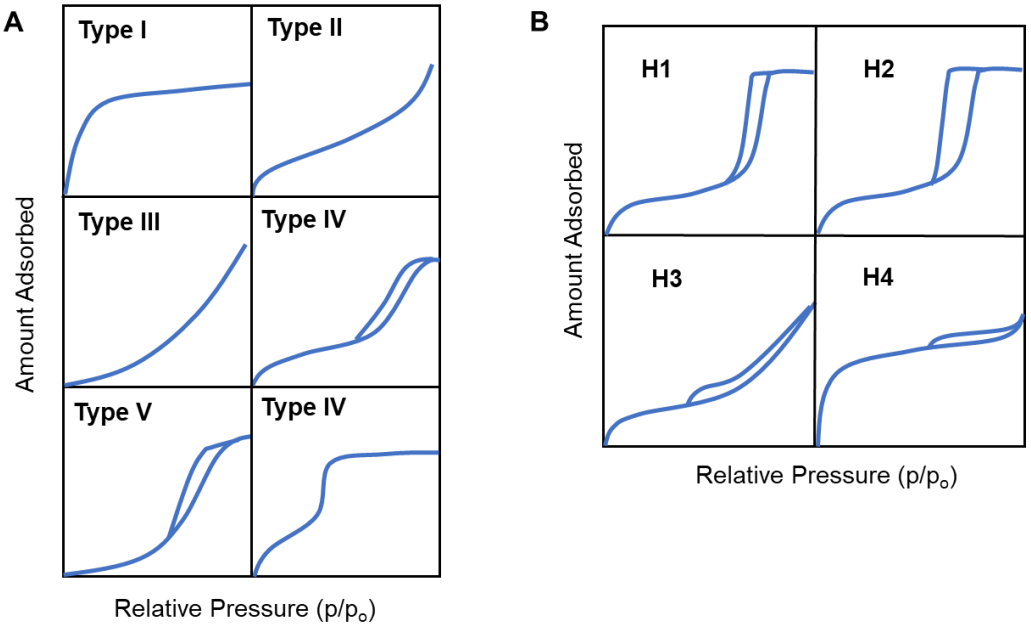

Figure 2. 14. IUPAC classifications for (A) adsorption isotherms and (B) hysteresis types.

To perform a BET surface area analysis, adsorption data are fit to the BET equation (Eq. 2.23) by a linear regression to determine the monolayer capacity of the surface,[138]

$$\frac{{}^{p}/_{p_o}}{\mathrm{V}(1-{}^{p}/_{p_o})} = \frac{\mathrm{c}-1}{\mathrm{V}_m c}\left({}^{p}/_{p_o}\right) + \frac{1}{\mathrm{V}_m c} \qquad \text{Eq. 2.23}$$

where V represents the volume of gas molecules adsorbed at a given relative pressure, p/p_o, V_m is the volume corresponding to monolayer coverage, and c is a constant. Isotherm data from the typical range of linearity (p/p_o = 0.05 – 0.030, where monolayer adsorption occurs) is plotted according to the BET equation (Fig. 2.15B).

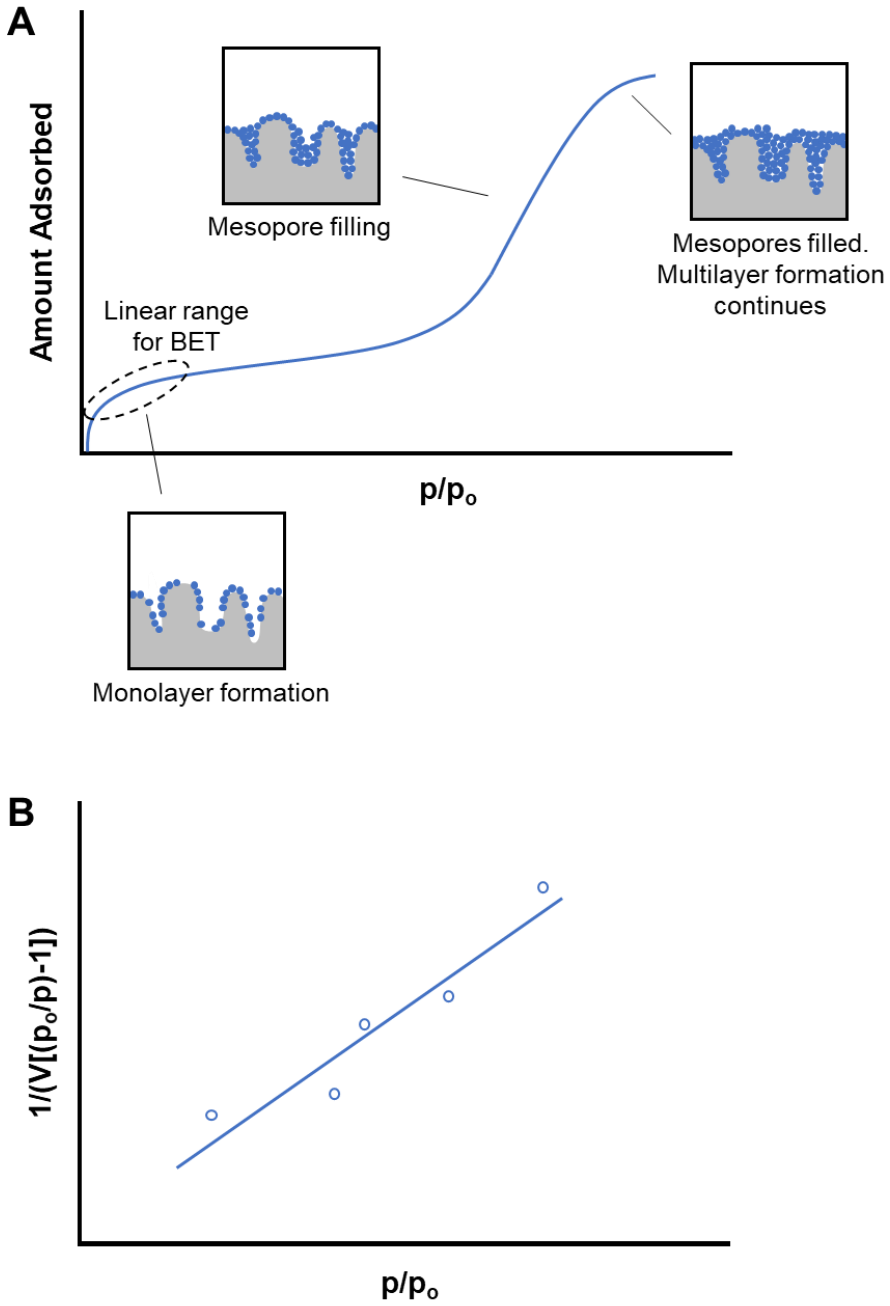

Figure 2. 15. (A) BET isotherm and illustrations showing the adsorption process for a mesoporous solid. (B) BET plot and linear regression.

Each term in the linear regression (y = mx + b) corresponds to a term in Eq. 2.23 such that the slope, m, and the intercept, b, are defined according to Eq. 2.24 and Eq. 2.25,

respectively. The numerical values for the slope and intercept can thus be used to solve for V_m and c.

$$\mathrm{m} = \frac{c-1}{\mathrm{V}_m c} \qquad \text{Eq. 2.24}$$

$$\mathrm{b} = \frac{1}{\mathrm{V}_m c} \qquad \text{Eq. 2.25}$$

Once V_m is known, the BET surface area (S_{BET}), which is the total surface area of the sample material, is determined using Eq. 2.26, where N_a is Avogadro's number, M_v is the molar volume of gas adsorbate, and s is the cross-sectional area of the adsorbate. The SSA for the known mass (m) of dry sample is determined using Eq. 2.27.[138]

$$\mathrm{S_{BET}} = \frac{\mathrm{V}_m \mathrm{N}_a s}{\mathrm{M}_v} \qquad \text{Eq. 2.26}$$

$$\mathrm{SSA} = \frac{\mathrm{S_{BET}}}{m} \qquad \text{Eq. 2.27}$$

In this work, N_2 adsorption experiments were performed using an Anton Paar NOVAtouch surface area and pore size analyzer. The samples were degassed at 200 °C for 12 hours prior to analysis. The pore size distributions were calculated using density functional theory (DFT) simulations.

2.3. Photocatalysis

The photocatalytic experiments in this work were performed using the setup illustrated in Fig. 2.16. A gas-tight Pyrex cell sealed with a rubber septum and hose clamp served as the reaction vessel for photocatalysis. In preparation for each experiment, the mp-Si powder was transferred to the reaction vessel which was then flushed with N_2 gas for

0.5 h. Distilled water and CH_3OH were also bubbled with N_2 for 0.5 h. After purging was complete, 5 mL of the N_2-bubbled CH_3OH and 30 mL of the N_2-bubbled water were added to the reaction vessel containing the mp-Si NPs under N_2 flow. The purpose of CH_3OH is to act as a sacrificial hole scavenger, as the band positioning of Si does not allow for water oxidation by the holes generated upon photoexcitation (Fig. 2.17). At neutral pH, the half-reactions can proceed according to Eq. 2.28 and Eq. 2.29, to give the overall reaction shown by Eq. 2.30.

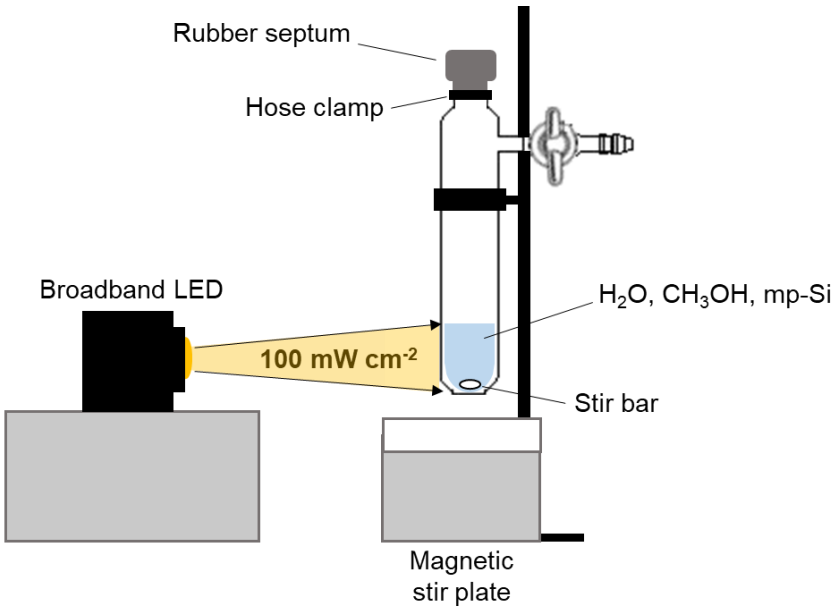

Figure 2. 16. Setup for photocatalysis experiments using mp-Si NPs.

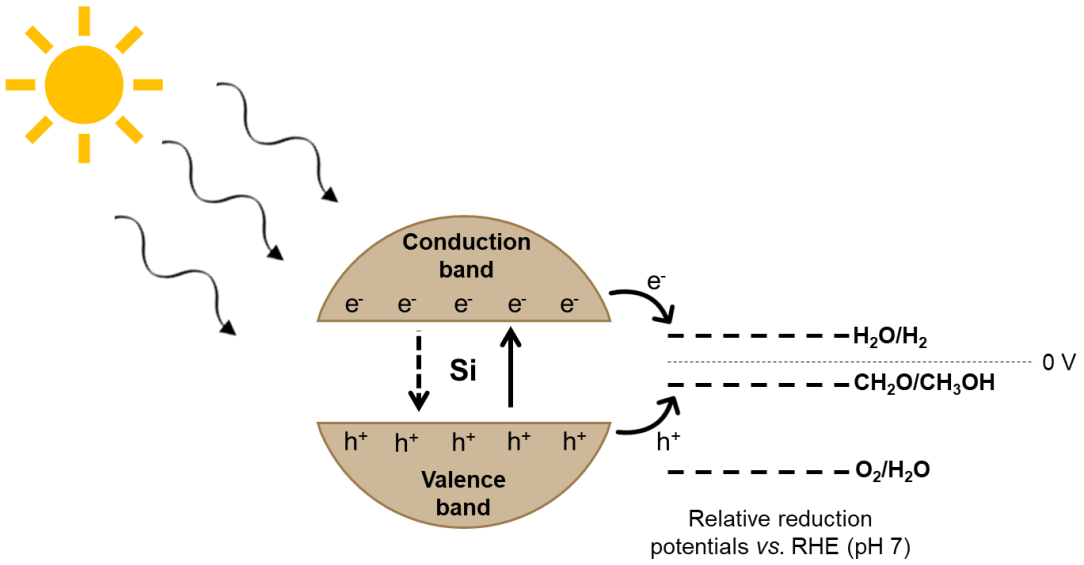

Figure 2. 17. Energy level diagram depicting charge carrier transfer during photocatalytic water splitting by a mp-Si NP.

$$CH_3OH \rightarrow CH_2O + 2H^+ + 2e^- \qquad \text{Eq. 2.26}$$

$$2H_2O + 2e^- \rightarrow H_2 + 2OH^- \qquad \text{Eq. 2.27}$$

$$CH_3OH \rightarrow CH_2O + H_2 \qquad \text{Eq. 2.30}$$

Once all the reagents were added to the vessel, N_2 flow was ceased, and the vessel was sealed off by tightening the hose clamp on the rubber septum. The reaction mixture was then sonicated (5 – 10 s) to ensure the mp-Si NPs were well dispersed, then stirred for the duration of the experiment. A broadband LED (Thorlabs, SOLIS-3C) was used as the light source and the photocatalytic reactions were carried out at 100 mW cm^{-2} (1 sun) illumination power density, calibrated using a silicon photodiode (Thorlabs). One sun illumination is a standard test condition for photovoltaic devices, and corresponds to the typical full sunlight intensity on a clear day on Earth.[139]

2.3.1. Quantification of Hydrogen by Gas Chromatography

To quantify the amount of H_2 produced during a photocatalytic experiment, gas from the reaction vessel headspace (10 mL) was collected using a syringe through the rubber septum and injected into a gas chromatograph. In gas chromatography (GC) components of a vaporized sample are separated by being distributed between the mobile and stationary phases of a column. The carrier gas (a chemically inert gas) is the mobile phase and helps to transport the sample components through the column to the detector. The stationary phase, located in the column, can be either a solid or liquid material. Upon reaching the column, components of the sample interact with the stationary phase, and are separated depending on the strength of the interaction. The distribution of components between the mobile phase and the stationary phase can be represented by the equilibrium expression in Eq. 2.31, where K is the distribution constant, and C_S and C_M are equilibrium concentrations of the analyte in the stationary phase, and the mobile phase, respectively.[140]

$$K = \frac{C_S}{C_M} \qquad \text{Eq. 2.31}$$

A sample component with a large distribution constant will be more strongly retained by the stationary phase and will therefore take more time to pass through the column than a component with a lower distribution constant. The time a component takes to reach the detector is called its retention time.

The components of a typical GC system are illustrated in Fig. 2.18. The carrier gas is contained in a gas cylinder connected to the system. Pressure regulators and flow meters control the flow of the gas through the GC column, which is housed in a thermostatted oven. A variety of detectors can be used for GC, including flame ionization, thermal

conductivity, electron capture, mass spectrometry detectors, and others.[126] The optimal choice of detector will depend on the types of compounds being analyzed and the information desired.

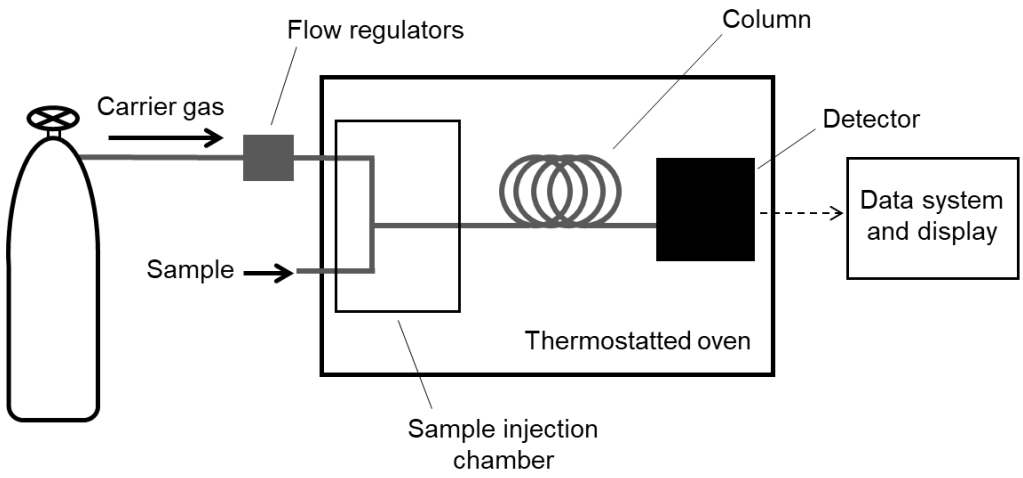

Figure 2. 18. Basic components and configuration of a typical GC system.

The columns used in GC can be classified into two main types: packed columns and open tubular (capillary) columns (Fig. 2.19). The former is densely packed with a solid packing material (typically uniform particles), which either acts as the stationary phase itself, or supports a liquid stationary phase. The latter can be further classified as either wall-coated open tubular (WCOT), support-coated open tubular (SCOT) or porous layer open tubular (PLOT) capillary columns. In WCOT columns, the inner wall is coated directly with a thin layer of the liquid stationary phase. Contrarily, SCOT columns are lined with a solid support on which the liquid stationary phase is adsorbed.[126] Capillary columns with a solid stationary phase are usually referred to as PLOT columns. These are coated

with porous sorbents such as alumina or SiO_2.[141] PLOT columns are commonly used for separations of compounds that are gaseous at room temperature.

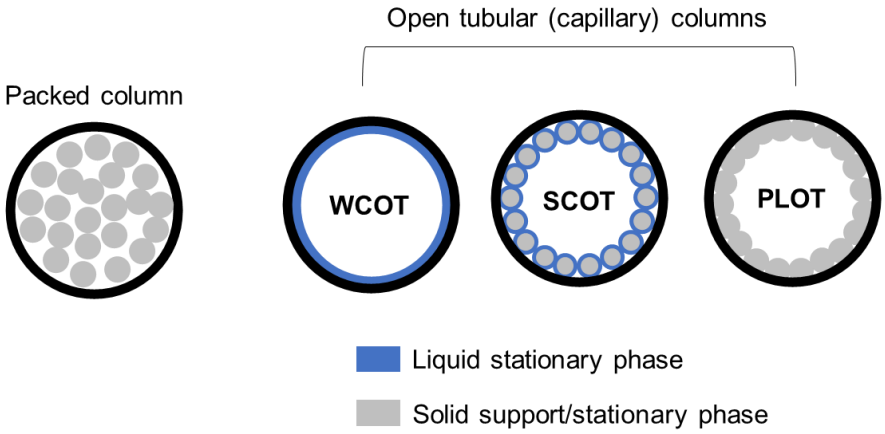

Figure 2. 19. Types of columns used in gas chromatography.

In this work, GC analysis was conducted using an Agilent 8860 GC system with a thermal conductivity detector (TCD) and N_2 as the carrier gas. The system is equipped with a molecular sieve analytical column as well as a precolumn, which serves to separate contaminants (such as air and hydrocarbons) to improve separation and protect the analytical column. A packed column containing Hayesep Q, 80-100 mesh adsorbent (made from copolymers of polydivinylbenzene)[142] was used as the precolumn. A PLOT capillary column coated with zeolite molecular sieve (CP-Molsieve 5 Å, 60-80 mesh) was used as the analytical column. The amount of H_2 was quantified using a calibration curve generated with gas mixtures (H_2/N_2) containing 0.08, 0.4, 1 and 5 % H_2.

GC-TCD is commonly used for hydrogen detection as it is capable of measuring a wide variety of hydrogen concentrations.[143] The basic principle of a TCD is the comparison

of the thermal conductivity of a component dissolved in the carrier gas with the pure carrier gas. The gas flows through an electrically heated thermostatted cavity which contains a sensing element (either a metal wire or thermistor). A typical TCD contains reference cells and sample cells housed in separate chambers and receiving a flow of the reference gas (pure carrier gas) and the sample gas from the column, respectively. Detection is based on the amount of heat lost from the sensor, which depends on the thermal conductivity of the gas.[126] For the best sensitivity, the carrier gas should have a thermal conductivity that is different from those of the sample components. For H_2 detection, N_2 is a well-suited carrier gas since the thermal conductivities of H_2 and N_2 are relatively distinct from each other.[143]

CHAPTER 3. Influence of the Magnesiothermic Reduction Conditions and Nanoparticle Aging on the Photocatalytic Activity of Mesoporous Silicon*

3.1. Introduction

Magnesiothermic reduction has become the sought-after method for synthesizing mp-Si given its ease, scalability, and tunability. As discussed in section 2.1.2, the reaction conditions of magnesiothermic reduction can be easily modified to change physical properties such as the surface area, pore size, crystallinity, and crystallite size of the resulting mp-Si.[87] While this can be an effective tool for designing the best performing mp-Si photocatalyst, unfortunately, it is not currently well understood how different magnesiothermic reduction conditions affect the photocatalytic behaviour of the mp-Si formed. Variations in reaction parameters (*i.e.,* SiO_2 precursor, reaction time, and temperature) between literature reports have led to different H_2 evolution rates despite the common use of magnesiothermic reduction as the synthetic method. As such, a systematic evaluation of the influence of magnesiothermic reduction parameters on the catalytic activity of mp-Si is required to design an optimum photocatalyst.

In this chapter, the relationship between the magnesiothermic reduction conditions (reaction temperature and time) and their influence on the photocatalytic activity for H_2 generation is detailed. The mp-Si NPs were prepared using either the conventional single temperature heating method or recently reported two-temperature heating method,[89] and characterized using techniques discussed in Chapter 2. The photocatalytic H_2 evolution

*Chapter 3 was adapted from Curtis, I. S.; Wills, R. J.; Dasog, M. Photocatalytic hydrogen generation using mesoporous silicon nanoparticles: influence of magnesiothermic reduction conditions and nanoparticle aging on the photocatalytic activity. *Nanoscale* **2021**, *13*, 2685–2692 with permission from the Royal Society of Chemistry. Initial photocatalysis screening experiments for various mp-Si NPs, as well as the synthesis and photocatalysis experiments for the mp-Si NPs annealed at 650 ºC for 6 h were performed by Ryan Wills. The author, I. S. Curtis's contributions include synthesizing SiO_2 and mp-Si NPs, performing XRD, SEM, Raman, and photocatalysis experiments, and assisting with manuscript preparation.

rates were determined for various mp-Si NPs and the performance was compared to their physical properties. While performing these studies, we noticed that the catalyst aging under ambient conditions also influenced the catalytic performance of mp-Si NPs. Therefore, the best performing photocatalyst was aged under ambient conditions and its photocatalytic activity was studied as a function of time.

3.2. Experimental Methods

3.2.1. Materials

Ammonium hydroxide (28% NH_3) and magnesium –325 mesh powder (Mg, 99.8%) were purchased from Alfa Aesar. Tetraethyl orthosilicate (TEOS, 99.9%), hydrochloric acid (HCl, 37%), methanol, and ethanol (95% and 100%) were purchased from Sigma-Aldrich. All reagents were used as received without further purification. Deionized water was obtained from an Arium Ultrapure Water System.

3.2.2. Synthesis of Stöber Silica Nanoparticles

The SiO_2 NPs were prepared as discussed in section 2.1.1.

3.2.3. Magnesiothermic Reduction of Silica Nanoparticles

The mp-Si NPs were prepared following the procedures discussed in section 2.1.2. The dried Stöber SiO_2 NPs (0.20 g) and –325 mesh Mg powder (0.18 g) were ground together using a mortar and pestle prior to annealing. Reactions were done using either single temperature heating (mp-Si650) or the two-temperature heating process (mp-Si100, mp-Si200, and mp-Si300).

3.2.4. Materials Characterization

Powder XRD, SEM, EDS, TEM, HRTEM, Raman, XPS, and UV-Vis were conducted as discussed in section 2.2. Particle size analysis was performed on SEM images using Image J software.

3.2.5. Photocatalytic Hydrogen Evolution

Photocatalytic experiments were performed using dried mp-Si NP powder (~0.01 g) following the procedure discussed in section 2.3. For a typical experiment, the mp-Si samples were used within 48 h after synthesis. For the cycling experiments, gas from the reaction vessel headspace was sampled every hour for a period of 5 h. Illumination was then ceased, and the reaction vessel was evacuated using N_2 flow before resuming illumination for another 5 h cycle. The reaction vessel was evacuated using N_2 flow and left overnight in the dark before performing the third 5 h cycle.

3.2.6. Catalyst Aging

To determine the effect of catalyst aging, the mp-Si NPs were stored in a glass vial under ambient atmosphere in a drawer for a predetermined amount of time. The photocatalytic activity was examined under broadband illumination as outlined in the previous section.

3.3. Results and Discussion

3.3.1. Characterization of Mesoporous Silicon Nanoparticles

Stöber SiO_2 NPs were prepared using a previously reported base catalyzed sol-gel method (detailed in section 2.1.1).[144] The synthesized particles were monodisperse and had

an average diameter of 295 ± 15 nm as seen in the SEM image (Fig. 3.1A). The powder XRD pattern showed a broad peak centered around ~22° corresponding to amorphous SiO_2 (Fig. 3.1B).[145]

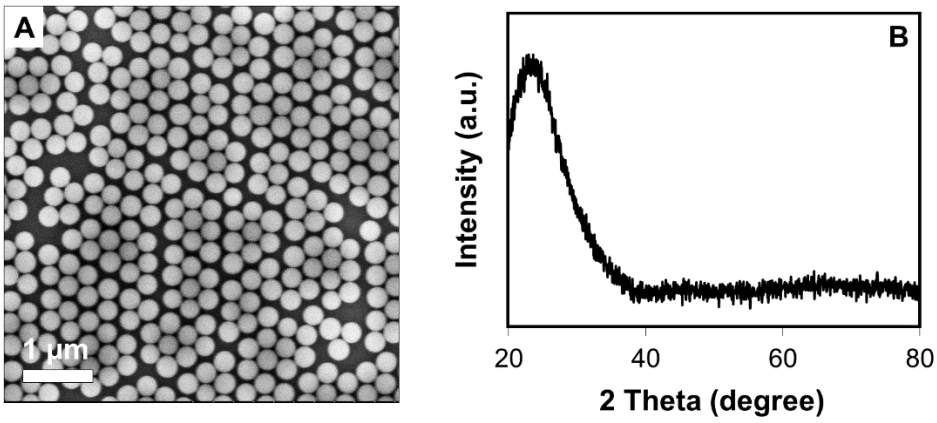

Figure 3. 1. (A) SEM image and (B) powder XRD pattern of Stöber SiO_2 NPs.

The SiO_2 NPs were reduced with Mg metal using the conventional single temperature heating at 650 °C for 3 h. The powder XRD pattern (Fig. 3.2) of the reduced product (mp-Si650) showed reflections at 28.3, 47.2, 56.1, 68.8, and 76.3° corresponding to the 111, 220, 311, 400, and 331 crystal planes of Si (JCPDS#27-1402), respectively. The SEM (Fig. 3.3A) and TEM (Fig. 3.3E) images of the product showed formation of porous Si NPs; however, morphological damage was observed, and the mp-Si NPs were found to be broken (Fig. 3.3E) and sintered in certain areas (Fig. 3.4). This structural damage occurs due to the exothermic nature of the magnesiothermic reduction reaction, where the local temperatures can reach above 1000 °C.[146,147] The HRTEM analysis showed the mp-Si NPs to be composed of crystalline primary particles (Fig. 3.3I) ranging between 20 – 40 nm in

diameter. The EDS analysis indicated the presence of 10 ± 2% atomic oxygen in the mp-Si650 sample.

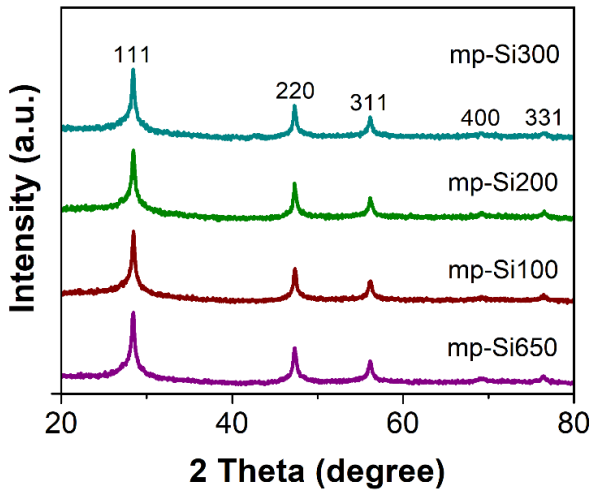

Figure 3. 2. Powder XRD patterns of mp-Si NPs prepared under different magnesiothermic reduction conditions.

To address the issue of heat induced structural damage, our group recently introduced a two-temperature heating method where the reaction is initiated at 650 °C, but the bulk of the reaction is carried out at a second lower temperature.[148] The heat released from the exothermic magnesiothermic reduction provides the additional energy required to sustain the reaction at lower temperatures. Three sets of mp-Si NPs were prepared using the two-temperature heating method, where the reaction was initially heated to 650 °C for 0.5 h followed by a second step of heating at 100 (mp-Si100), 200 (mp-Si200), or 300 °C (mp-Si300) for 6 h. The powder XRD patterns of all three samples showed characteristic reflections corresponding to crystalline elemental Si (Fig. 3.2). The SEM (Fig. 3.3B – D) and TEM (Fig. 3.3F – H) analysis showed mostly spherical mp-Si NPs with minimal

structural damage for samples made with this method. Similar to the mp-Si650 sample, the mp-Si300 showed crystalline primary particles (Fig. 3.3L) ranging between 15 – 30 nm. The mp-Si100 and mp-Si200 samples had smaller regions of crystallinity within the primary particles surrounded by a more disordered structure (Figures 2J and K). The EDS analysis of these mp-Si NPs showed atomic oxygen content of 21 ± 2, 10 ± 2, and 7 ± 1% for the mp-Si100, mp-Si200, and mp-Si300 samples, respectively.

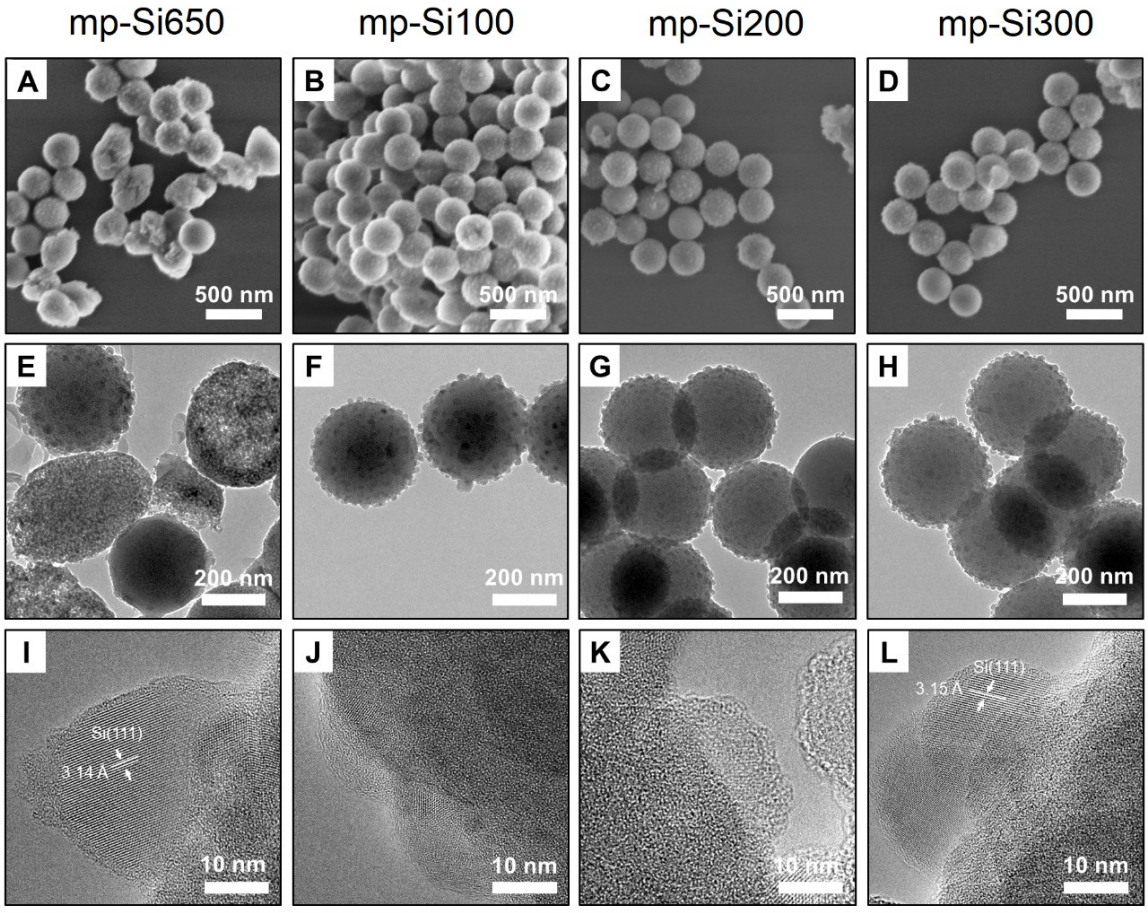

Figure 3. 3. (A – D) SEM, (E – H) TEM, and (I – L) HRTEM images of mp-Si NPs prepared under different magnesiothermic reduction conditions.

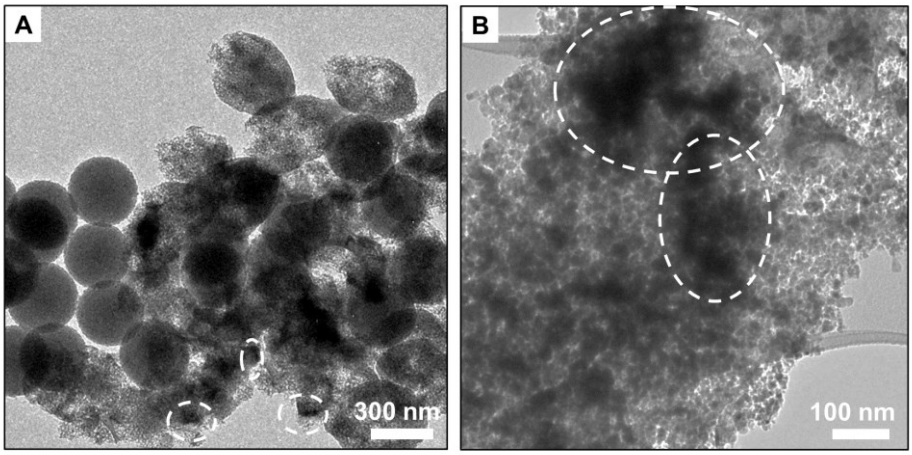

Figure 3. 4. (A) and (B) TEM images of mp-Si650 NPs showing sintering (circled regions).

As discussed in section 2.2.4, Raman spectroscopy is a useful technique to determine crystallinity in Si structures. Typically, a sharp peak is observed at ~520 cm^{-1} corresponding to crystalline Si and a broad peak centered around ~480 cm^{-1} is observed for amorphous Si.[149] For nanocrystalline Si, as the crystallite size and degree of crystallinity decreases, the peak shifts from 520 cm^{-1} to lower wavenumbers and the full width at half maximum (FWHM) of the peak increases.[120] While the powder XRD patterns of all the mp-Si NPs were similar, the Raman analysis revealed the differences in these samples (Fig. 3.5). The mp-Si650 NPs had a peak maximum at 512 cm^{-1} and FWHM of 17 cm^{-1}. The mp-Si300 sample was similar to mp-Si650 with a peak maximum at 514 cm^{-1} and FWHM of 15 cm^{-1}. The peak maximum shifted from 514 to 503 and 494 cm^{-1} as the second heating temperature decreased from 300 to 200 and 100 °C, respectively. Correspondingly, the peak FWHM increased to 22 and 26 cm^{-1} for mp-Si200 and mp-Si100 NPs, respectively, indicating a decrease in grain size and crystallinity with decreasing temperatures which is consistent with HRTEM analysis.

XPS analysis was performed to understand the extent of surface oxidation in the mp-Si NP samples. The Si 2p region of freshly prepared mp-Si NPs showed the presence of elemental Si (Si(0) $2p_{3/2}$ peak at ~99.2 eV), suboxides (Si(+1, +2, and +3) $2p_{3/2}$ peaks at ~100.2, ~101.4, and ~102.5 eV, respectively), and SiO_2 (Si(+4) $2p_{3/2}$ peak at ~103.4 eV) in all the samples (Fig. 3.6).[150] The highest amount of SiO_2 was present in the mp-Si100 and mp-Si650 samples whereas, the smallest amount of SiO_2 was present in the mp-Si300 NPs. Our group has previously determined the SSA of mp-Si650, mp-Si100, mp-Si200, and mp-Si300 samples using N_2 adsorption measurements to be 174 ± 22, 364 ± 18, 412 ± 15, and 527 ± 21 $m^2\ g^{-1}$, respectively.[147,148]

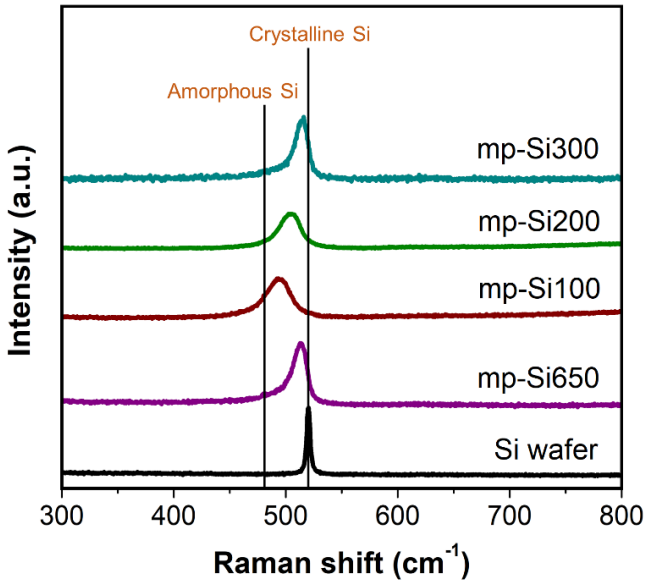

Figure 3. 5. Raman spectra of a Si wafer and mp-Si NPs prepared under different magnesiothermic reduction conditions.

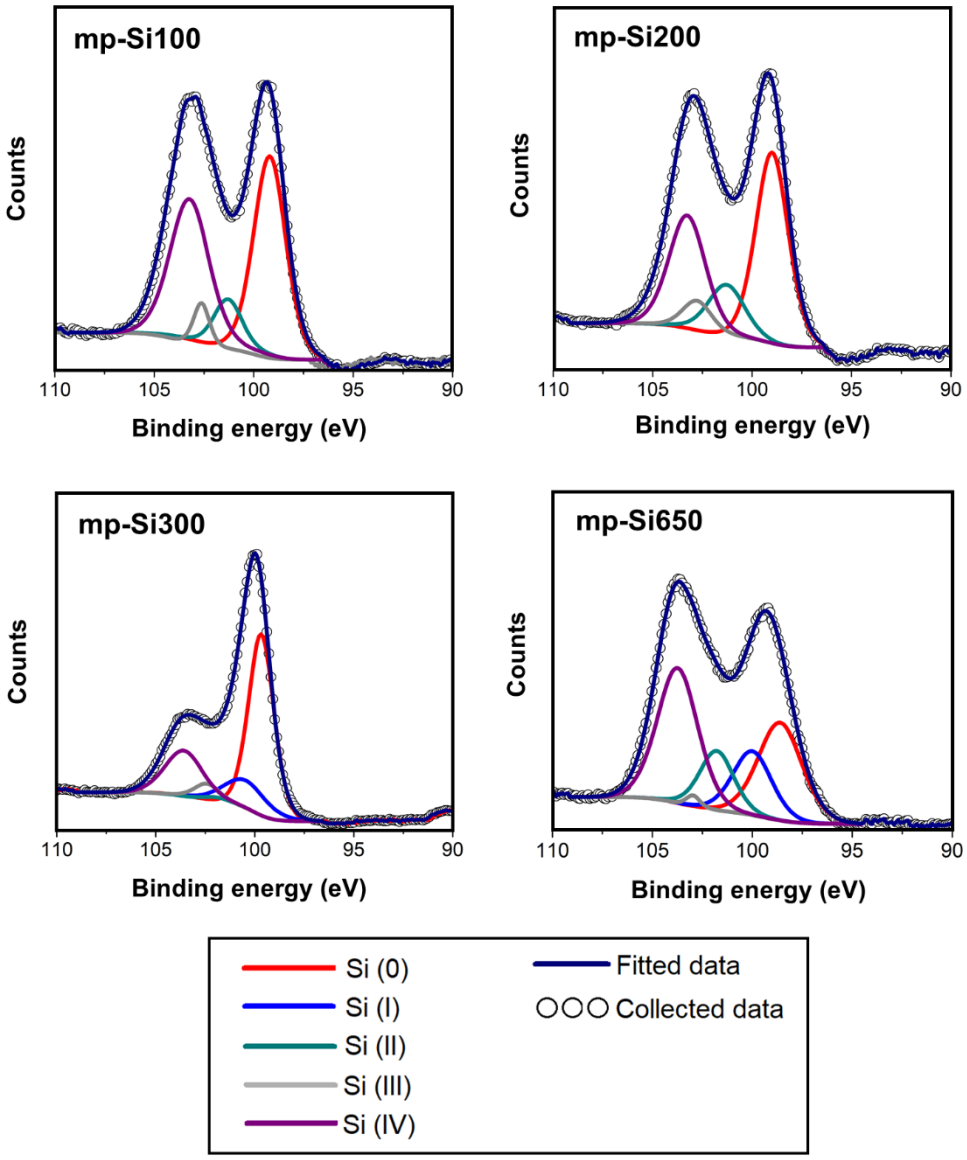

Figure 3. 6. High resolution XP spectra of the Si 2p region of mp-Si NPs prepared under different magnesiothermic reduction conditions. For clarity, only $2p_{3/2}$ fit peaks are shown.

Optical absorption measurements were performed on mp-Si NPs dispersed in EtOH (Fig. 3.7) and all the samples exhibited the typical absorption profile observed for nanostructured Si where the absorption increases moving from the near-IR to visible

region. The optical bandgaps of mp-Si samples were estimated using Tauc plots (Fig. 3.7) derived from the absorption measurements to be 1.45, 1.52, 1.50, and 1.46 eV for mp-Si650, mp-Si100, mp-Si200, and mp-Si300 NPs, respectively. All the values were higher than the bulk Si bandgap of 1.11 eV which is due to quantum confinement effects in the nanostructured mp-Si NPs.[151] This observation is consistent with other mp-Si materials prepared using magnesiothermic reduction which all exhibit wider bandgaps than bulk Si.[72–74]

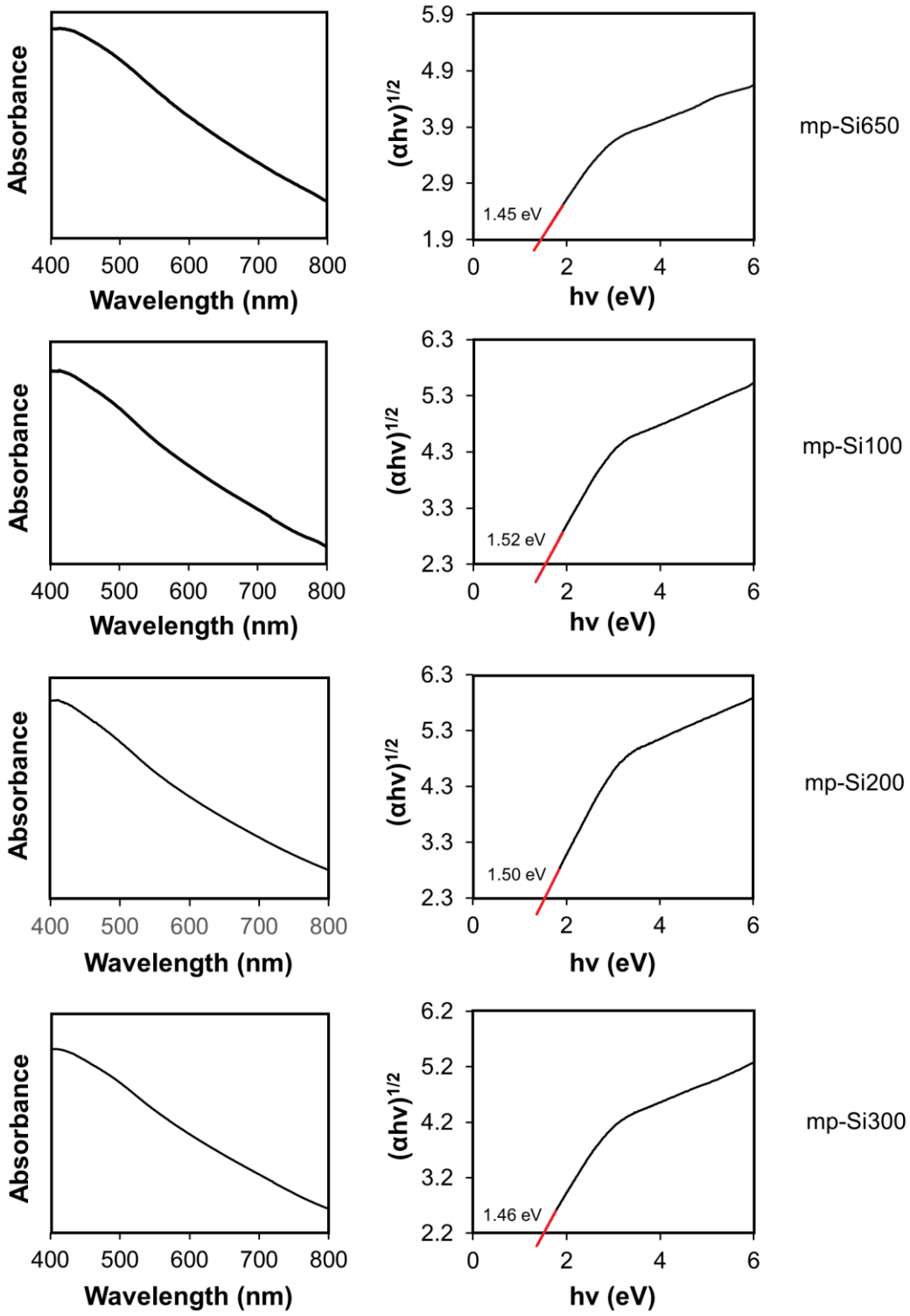

Figure 3. 7. UV-Vis absorbance spectra and corresponding Tauc plots of mp-Si NPs prepared under different magnesiothermic reduction conditions.

3.3.2. Photocatalytic Hydrogen Evolution: Effect of the Magnesiothermic Reduction Conditions

The photocatalytic H_2 evolution performance of freshly prepared (less than 48 h after the synthesis) mp-Si NPs *via* water-splitting was investigated under 100 mW cm^{-2} broadband illumination. As Si does not have a wide enough bandgap to perform overall water splitting, CH_3OH (which gets oxidized to CH_2O[45]) was used as a sacrificial hole scavenger in the photocatalytic experiments. The amount of H_2 evolved was quantified using gas chromatography. The typical H_2 evolution profiles for the different mp-Si NPs are shown in Fig. 3.8A. An H_2 evolution rate of 3554 ± 373, 1118 ± 275, 1997 ± 350, and 4437 ± 450 μmol h^{-1} g^{-1} of Si was observed for mp-Si650, mp-Si100, mp-Si200, and mp-Si300, respectively (Fig. 3.8B). In the dark, H_2 evolution rates were below 200 μmol h^{-1} g^{-1} of Si for all the samples investigated. The lowest rate was observed for the mp-Si100 sample, which is likely due to the high oxygen content and low crystallinity, both of which introduce large concentrations of defect states leading to charge carrier recombination and low catalytic activity.[73,152–154] The XPS analysis revealed mp-Si100 to have a high surface SiO_2 amount (Fig. 3.6) and the EDS analysis showed high atomic oxygen content probably due to incomplete reduction. This can be seen in the TEM analysis of this sample (Fig. 3.3F) which contains a darker core likely due to the presence of non-porous unreduced SiO_2. The HRTEM (Fig. 3.3J) and Raman (Fig. 3.5) analysis also revealed the presence of less crystalline regions in the mp-Si100 sample. The best performance was observed for the mp-Si300 sample, which had the lowest oxygen content and possessed high crystallinity. Even though mp-Si650 had similar crystallinity to the mp-Si300 NPs (as seen in the HRTEM and Raman analysis), it had lower activity owing to higher surface oxidation as seen in the XPS (Fig. 3.6). Due to more extensive morphological damage, the mp-Si650

NPs fractured, exposing more of the Si which probably results in higher surface oxidation. Furthermore, sintering can introduce higher amounts of grain boundaries which can act as trap states for charge carriers[155] and contribute to lower photocatalytic activity. While both the mp-Si650 and mp-Si200 have a similar oxygen content based on EDS analysis, the latter had lower photocatalytic performance likely due to lower crystallinity. This shows that Si crystallinity is more crucial in determining its photocatalytic activity. The cycling ability of only the highest performing mp-Si300 sample was evaluated (Fig. 3.8C). A slight drop in the H_2 evolution rate was observed in cycle 2, however, after leaving the mp-Si NPs suspended in water overnight, a considerable decline in photocatalytic activity was observed in cycle 3. Similar drops in performance during cycling experiments have been observed before, due to the gradual surface oxidation of mp-Si NPs.[72] Robust surface protection strategies are required to improve the longevity of mp-Si NPs and make them a viable option for solar-driven H_2 generation *via* water-splitting. The mp-Si300 NPs were also tested under natural sunlight during which bubble evolution (due to H_2 gas formation) can be seen, demonstrating their potential in solar-driven water-splitting (Fig. 3.8D).

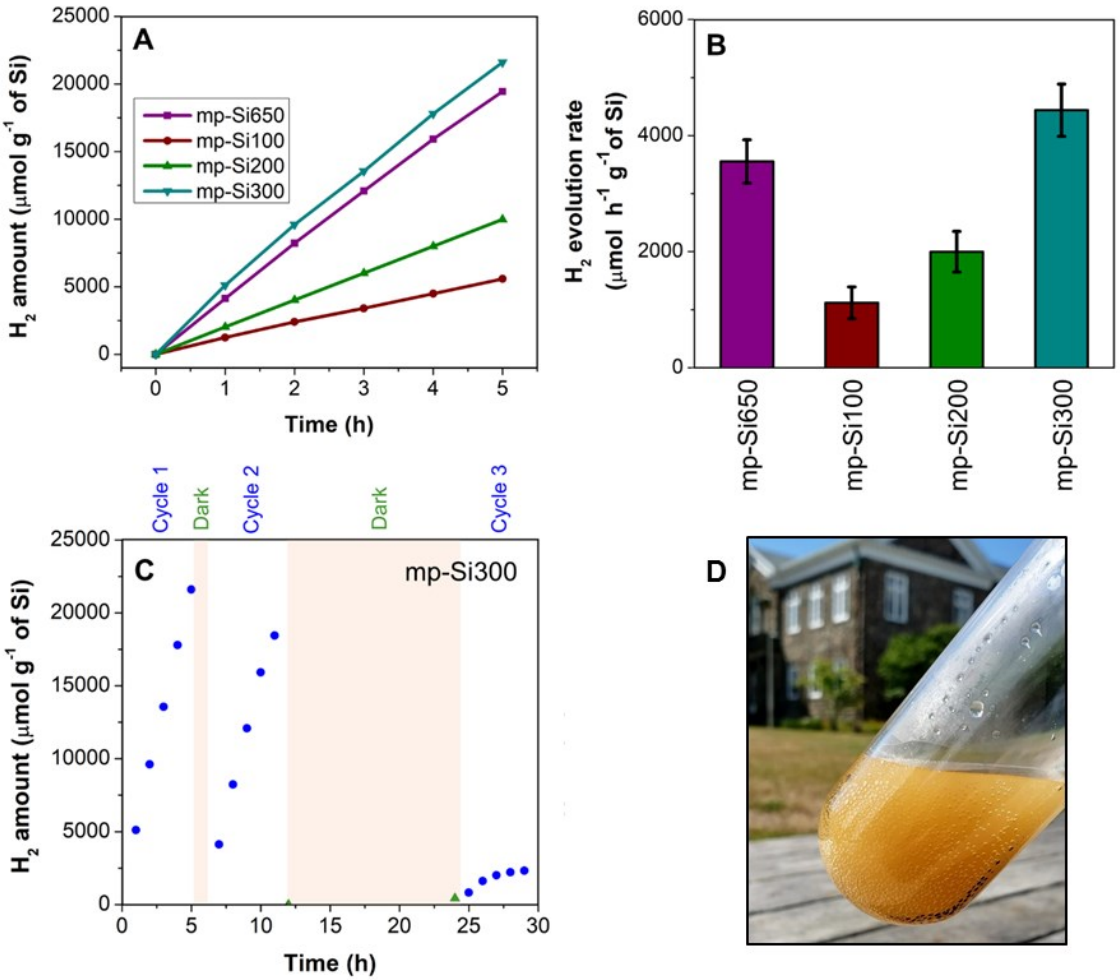

Figure 3. 8. (A) H_2 evolution profiles of different mp-Si NPs under broadband illumination, (B) H_2 evolution rates of mp-Si NPs, (C) photocatalytic cyclability of mp-Si300 NPs, and (D) formation of H_2 gas under natural sunlight by mp-Si300 NPs in water + CH_3OH solution.

The influence of magnesiothermic reduction time on the photocatalytic activity of mp-Si NPs was also explored. The mp-Si NPs were prepared using the conventional single temperature heating method at 650 °C, but the reaction time was increased from 3 to 6 h. The powder XRD pattern revealed the formation of crystalline Si (Fig. 3.9A) but the TEM images showed extensive particle damage and sintering (Fig. 3.9B and C). The EDS analysis indicated presence of 8 ± 1% atomic oxygen. The photocatalytic study showed an

H_2 evolution rate of 983 ± 223 μmol h^{-1} g^{-1} of Si which is significantly lower compared to the 3 h reaction time sample. This is likely due to particle sintering, which can introduce a significant number of grain boundaries and defect states in which the carriers can get trapped.[155] Therefore, care must be taken to prevent extensive morphological damage during the synthesis of mp-Si NPs.

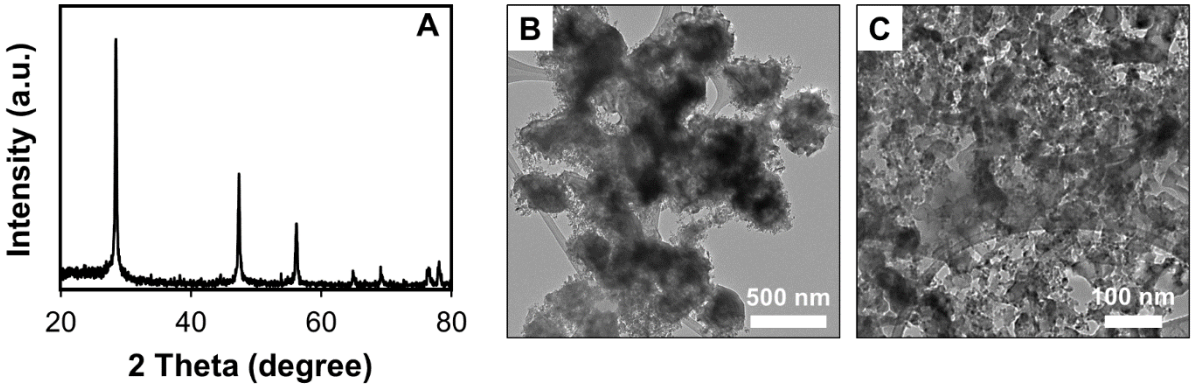

Figure 3. 9. (A) Powder XRD pattern, (B) and (C) TEM images of mp-Si NPs prepared at 650 °C with 6 h reaction time.

3.3.3. Catalyst Aging

After the synthesis of mp-Si, the NPs form an oxide shell as shown by the XPS analysis (Fig. 3.6). This native oxide on Si is typically believed to be self-passivating (within a few hours) and as such, the synthesized mp-Si NPs were stored under ambient conditions.[156] However, a gradual decline in the H_2 evolution rates was observed even in a matter of a few days, while performing the replicates for the photocatalytic studies. The H_2 evolution rate decreased from 4437 to 4055 μmol h^{-1} g^{-1} of Si after storing the mp-Si300 NPs for ~7 days in air (Fig. 3.10). The rate continued to decrease to 3175 and 1899 μmol

h^{-1} g^{-1} of Si as the sample was aged for ~30 and ~90 days, respectively. XPS analysis of the Si 2p regions showed an increase in SiO_2 and Si suboxide amounts with catalyst aging (Fig. 3.11). Correspondingly, EDS analysis showed the atomic % oxygen to increase from 7 ± 1 in the freshly prepared mp-Si300 to 11 ± 2, 18 ± 2, and 22 ± 3% for samples aged for approximately 7, 30, and 90 days, respectively. This demonstrates that oxidation continues to occur long after the mp-Si NP synthesis and care must be taken to properly store them. The surface oxides are known to introduce trap states in nanostructured Si,[157] which would deleteriously affect the catalytic activity and therefore a decline in H_2 evolution rate is observed. In the future, it would also be beneficial to report the age of the mp-Si photocatalysts to allow for better comparison between the different literature reports.

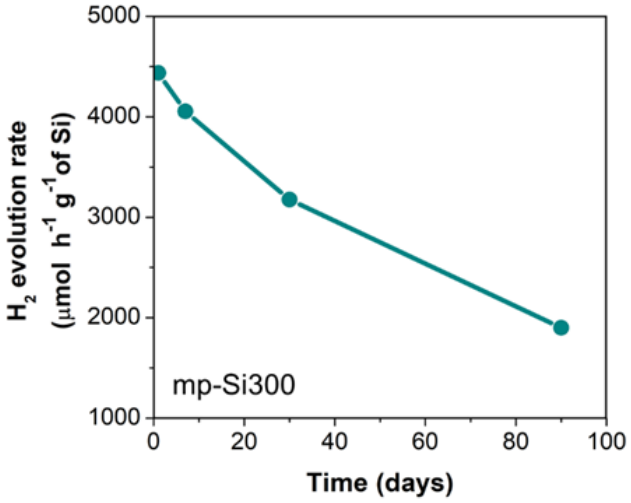

Figure 3. 10. Change in H_2 evolution rate of mp-Si300 NPs with catalyst aging (time after synthesis).

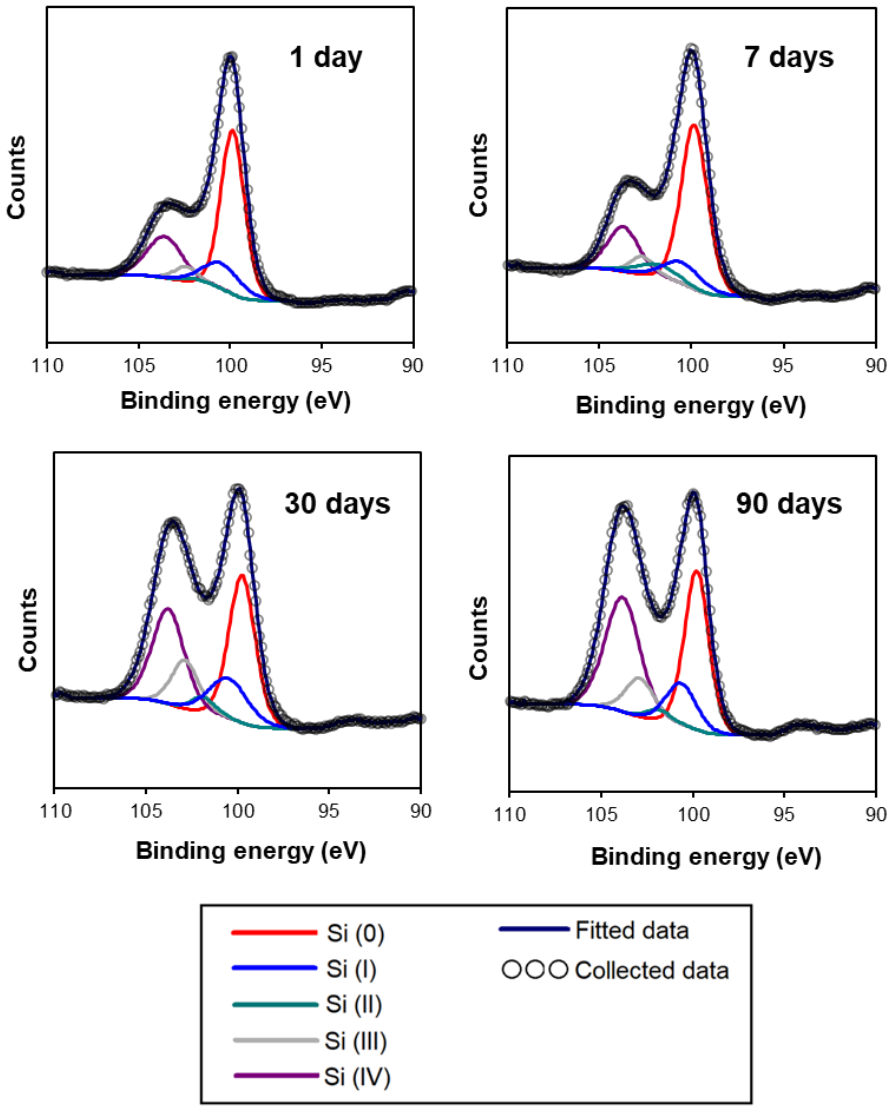

Figure 3. 11. High resolution XP spectra of the Si 2p region of mp-Si300 NPs at different times after the synthesis and storage under ambient conditions. For clarity, only $2p_{3/2}$ peaks of different oxidation states are shown.

3.4. Conclusions

In summary, this chapter discusses the influence of magnesiothermic reduction conditions on the photocatalytic activity of mp-Si NPs. When the NPs are prepared using the conventional single temperature heating step at 650 °C for 3 h, an H_2 evolution rate of

3554 μmol h^{-1} g^{-1} of Si was observed. When the reaction time was increased, the rate decreased to 983 μmol h^{-1} g^{-1} owing to an increase in particle sintering. Three sets of mp-Si NPs were prepared using a two-step heating process where the reaction was initiated at 650 °C for 0.5 h, but the bulk of the reaction was performed at 100, 200, or 300 °C. Of these, mp-Si100 had the lowest H_2 evolution rate of 1118 μmol h^{-1} g^{-1} of Si due to low crystallinity and high amounts of oxygen. The mp-Si200 had an H_2 evolution rate of 1997 μmol h^{-1} g^{-1} of Si despite lower amount of oxygen. It is hypothesized that the crystallinity plays an important role in determining the catalytic activity and therefore, mp-Si200 exhibited lower activity due to lesser crystallinity. The mp-Si300 NPs had the highest H_2 evolution rate reported in the literature to date of 4437 μmol h^{-1} g^{-1} of Si, as it had good crystallinity, low oxygen content, and minimal particle sintering. To prepare optimally performing mp-Si photocatalysts, we need to maximize crystallinity but also minimize oxidation and grain boundaries resulting from particle sintering.

The mp-Si NPs were found to continue to oxidize when stored under ambient conditions which led to a decrease in the H_2 evolution rate over time. Therefore, care must be taken to store the mp-Si NPs to minimize oxidation. In the future, surface protection approaches must be developed to improve the longevity of mp-Si NPs during the photocatalytic experiments.

CHAPTER 4. Influence of Porosity on the Photocatalytic Performance of Mesoporous Silicon

4.1. Introduction

Magnesiothermic reduction has been used to prepare mp-Si from a variety of SiO_2 sources including SiO_2 fume,[158] clay,[111] rice husks,[159–161] sand,[162] diatoms,[109,163] zeolites,[164] and other industrial wastes.[165] The SiO_2 precursor acts as a template for mp-Si during magnesiothermic reduction, and the overall morphology is usually well maintained in the product. The effects of the reaction conditions are typically assumed to outweigh the effects of the chosen precursor on the properties of mp-Si.[98] However, the type of SiO_2 precursor used to prepare mp-Si *via* magnesiothermic reduction can still be a contributing parameter affecting the morphology and pore characteristics of the photocatalyst.

The work discussed in Chapter 3 revealed that crystallinity plays a dramatic role in the photocatalytic performance of mp-Si photocatalysts, and is influenced by the conditions (*i.e.,* reaction temperature and time) of magnesiothermic reduction. Secondly, a high oxygen content arising from incomplete reduction and/or surface oxidation of mp-Si deleteriously affects H_2 evolution rates.[166] In this chapter, the role of precursor porosity on the photocatalytic activity of mp-Si is examined. Studies performed on TiO_2 photocatalysts have shown that the catalytic activity increases with increasing SSA.[167–170] Mesoporous SiO_2 precursors (SBA-15) of varying pore sizes were used to synthesize nanostructured mp-Si. Conventional SBA-15 mesoporous SiO_2 has a fibrous macrostructure consisting of rod-like particles several tens of micrometers in length. The rods consist of a hexagonal array of uniform channels (pores), formed using a surfactant-templating method, which have a tunable average diameter typically in the nanoscale, which depends on the structure of the surfactant used.[171,172] In this study, mp-Si was prepared using SBA-15 SiO_2 with

pore sizes of 4 (mp-Sip4), 6 (mp-Sip6), and 8 (mp-Sip8) nm. The degree of crystallinity of the mp-Si was held constant by using the same reaction conditions (temperature and time) for the magnesiothermic reduction of each precursor. With crystallinity as a control variable, the effects of the surface area and pore size on the photocatalytic performance could be more closely investigated. The mp-Si NPs were characterized using the techniques discussed in Chapter 2. The H_2 evolution rates were determined and compared against the physical properties of the mp-Si photocatalysts.

4.2. Experimental Methods

4.2.1. Materials

Magnesium −325 mesh powder (Mg, 99.8%) was purchased from Alfa Aesar. SBA-15 mesoporous SiO_2 (< 150 μm, pore sizes of 4, 6, and 8 nm), hydrochloric acid (HCl, 37%), and methanol were purchased from Sigma-Aldrich. All reagents were used as received without further purification. Deionized water was obtained using an Arium Ultrapure Water System.

4.2.2. Magnesiothermic Reduction of SBA-15 Mesoporous Silica

The mp-Si NPs were prepared as discussed in sections 2.1.2 and 3.2.3. All samples were annealed at 650 °C for 0.5 h, then cooled and held at 300 °C for 6 h.

4.2.3. Materials Characterization

Powder XRD, SEM, EDS, TEM, HRTEM, Raman, XPS, UV-Vis and surface area analysis were conducted as discussed in section 2.2. Surface area and pore size analysis was conducted by a technician at Anton Paar Canada Inc.

4.2.4. Photocatalytic Hydrogen Evolution

Photocatalytic experiments were performed as discussed in sections 2.3 and 3.2.5.

4.3. Results and Discussion

4.3.1. Characterization of Mesoporous Silicon Nanoparticles and Precursors

Mesoporous SiO_2 (SBA-15) with particle size < 150 μm and pore sizes of 4, 6 and 8 nm ($SBA\text{-}15_{4nm}$, $SBA\text{-}15_{6nm}$, $SBA\text{-}15_{8nm}$, respectively) were commercially purchased and used without further purification. Microscopy (SEM and TEM) images of these precursors (Fig. 4.1) show the typical fiber-like morphology of SBA-15, consisting of rods several microns in length. Some spherical structures, which appear to be agglomerates of smaller particles, are also seen using SEM. The pore channels, which run lengthwise through the rod-shaped SBA-15 particles can be seen in the TEM images. All three precursors show a broad peak ~22° in their XRD patterns (Fig. 4.2), corresponding to amorphous SiO_2.[173]

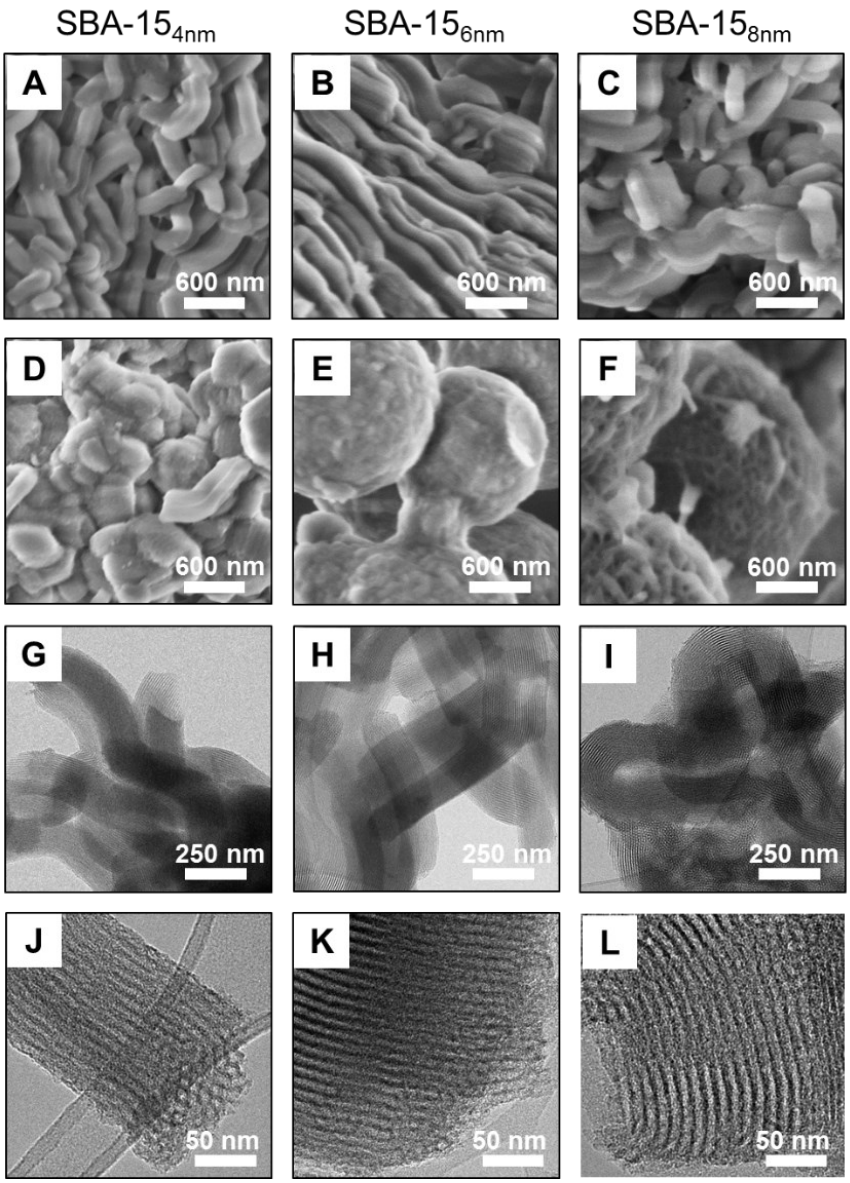

Figure 4. 1. (A – F) SEM, (G – I) TEM, and (J – L) HRTEM images of SBA-15 SiO_2 with varying pore sizes.

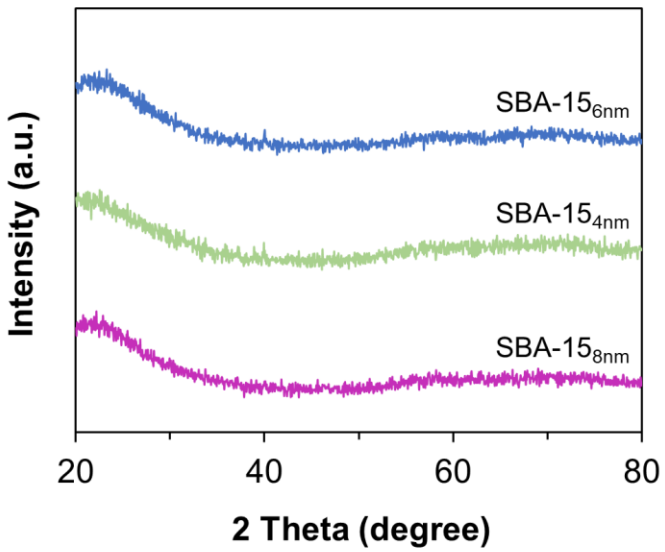

Figure 4. 2. Powder XRD patterns of SBA-15 SiO_2 with varying pore size.

In previous work using Stöber SiO_2 precursors (Chapter 3), the optimal reaction conditions for the highest performing photocatalyst were achieved using a two-temperature heating method, which reduced the effect of heat-induced structural damage. To prepare mp-Si with varying average pore sizes, the SBA-15 precursors and –325 mesh Mg metal were heated to 650 °C (Mg melting point) for 0.5 h to initiate the reaction, then held at 300 °C for 6 h. The powder XRD patterns (Fig. 4.3) of the reduced products (mp-Sip4, mp-Sip6, and mp-Sip8) showed reflections at 28.3, 47.2, 56.1, 68.8, and 76.3° corresponding to the 111, 220, 311, 400, and 331 crystal planes of Si (JCPDS#27-1402), respectively. Notably, the peaks in the XRD pattern are clearly broadened compared to the mp-Si synthesized under the same reaction conditions in Chapter 3,[166] indicating that the SBA-15 produces mp-Si with smaller crystallite sizes. The SEM and TEM analysis (Fig. 4.4) showed similar rod-shaped particles as in the precursors; however, some of the particles appear to be fractured. Additional to the pore channels of the template SBA-15, the

products have a sponge-like texture which is a result of the magnesiothermic reduction reaction. The newly formed mesopores are seen throughout the surface and on the pore walls of the material, causing the original pore walls of SBA-15 to become more interconnected. HRTEM analysis shows each of the mp-Si samples to contain crystalline regions ranging from about 3 nm to a maximum of ~20 nm in size (Figure 2G-I). Regions of a more disordered structure between the crystallites are also seen in each sample.

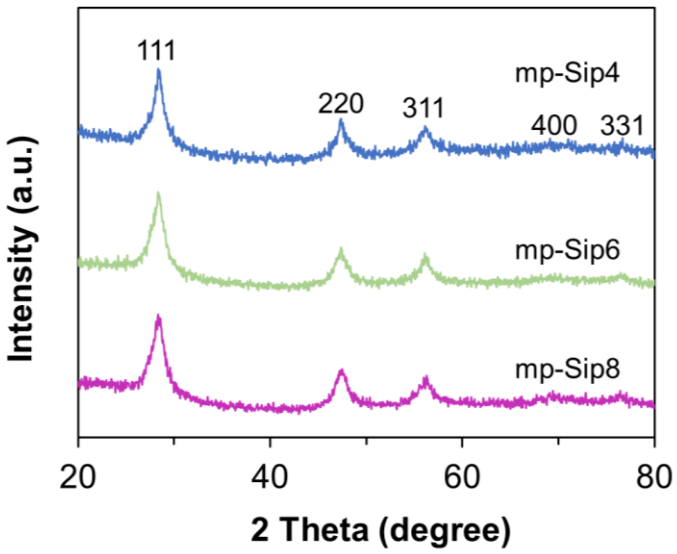

Figure 4. 3. Powder XRD patterns of mp-Si NPs prepared by magnesiothermic reduction using different SBA-15 precursors with varying pore size.

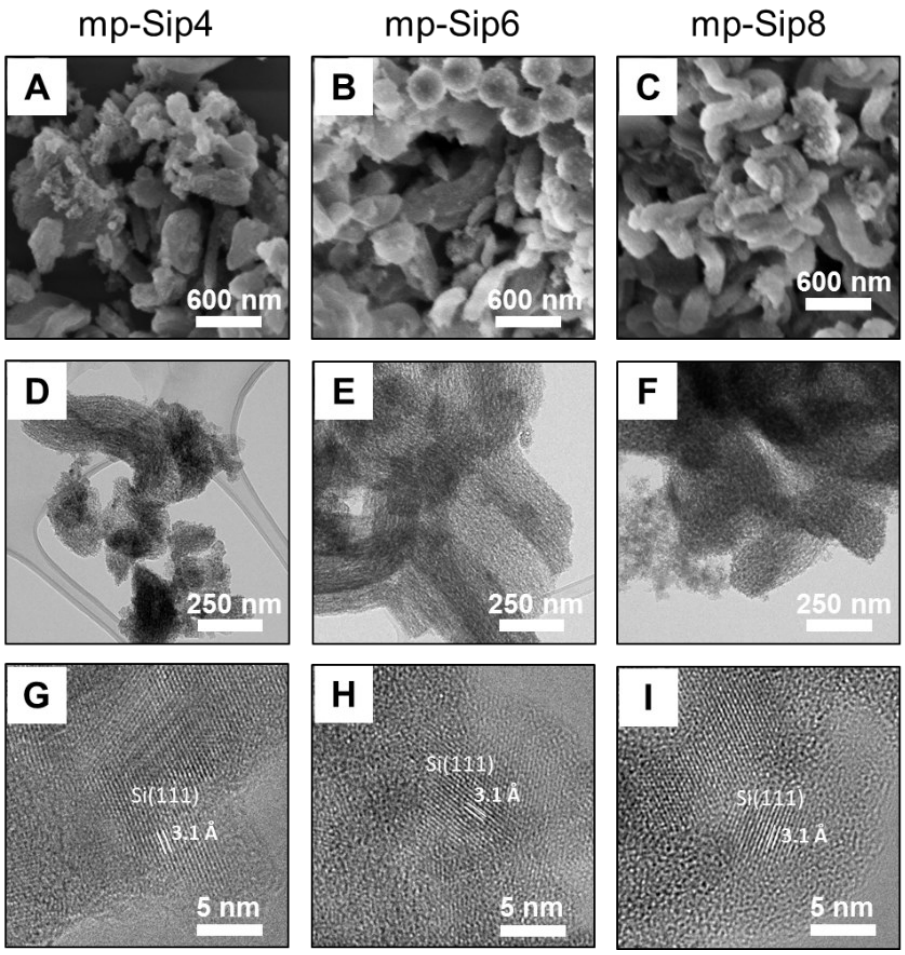

Figure 4. 4. (A – C) SEM, (D – F) TEM and (G – I) HRTEM images of mp-Si NPs prepared by magnesiothermic reduction using different SBA-15 precursors with varying pore size.

Raman spectroscopy was used to check for differences in crystallinity not observable by XRD analysis. The mp-Sip4, mp-Sip6, and mp-Sip8 samples all showed a peak in their Raman spectra with a maximum at ~509 cm^{-1} (Fig. 4.5), which is shifted and broadened compared to the peak for a monocrystalline Si wafer (520 cm^{-1}). A peak centered at 480 cm^{-1} in each sample confirms the presence of amorphous regions, consistent with the HRTEM analysis.

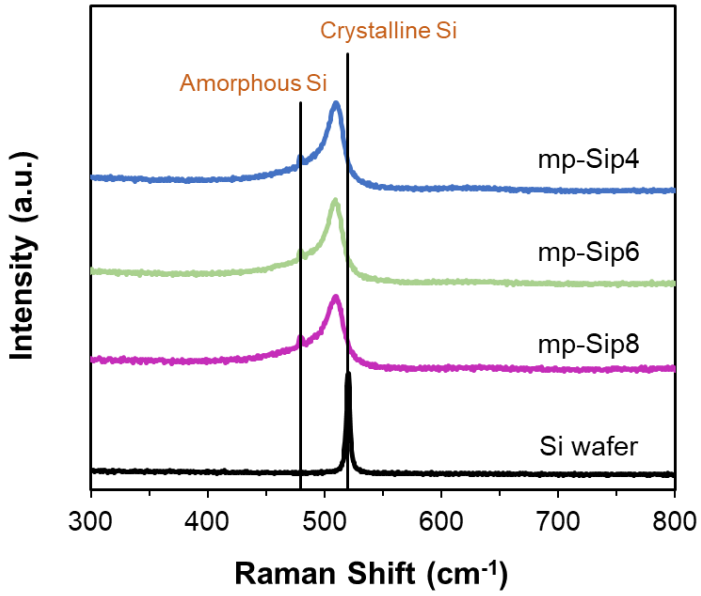

Figure 4. 5. Raman spectra of mp-Si NPs prepared by magnesiothermic reduction using different SBA-15 precursors with varying pore size. The Raman spectrum of a Si wafer is included for comparison.

As discussed in Chapter 3, surface oxidation of mp-Si photocatalysts plays an important role in their photocatalytic performance. Following their synthesis, mp-Si NPs quickly form an oxide layer, which under ambient conditions continues to accumulate over time and can reduce H_2 evolution rates.[166] As such, the mp-Si samples in this chapter were stored under inert atmosphere immediately after synthesis. XPS analysis was performed to compare the extent of surface oxidation between the mp-Sip4, mp-Sip6, and mp-Sip8 samples (Fig. 4.6). The Si 2p region showed the presence of elemental Si (Si(0) $2p_{3/2}$ peak at ~99.2 eV), suboxides (Si(+1, +2, and +3) $2p_{3/2}$ peaks at ~100.2, ~101.4, and ~102.5 eV, respectively), and SiO_2 (Si(+4) $2p_{3/2}$ peak at ~103.4 eV) in all the samples. The mp-Sip4 NPs had the smallest amount of surface oxides. Higher amounts of SiO_2 and Si suboxides were present in the mp-Sip6 and mp-Sip8 samples. EDS analysis was also

performed and showed an atomic oxygen content of 31 ± 4, 34 ± 3 and 46 ± 3 for the mp-Sip4, mp-Sip6, and mp-Sip8, respectively.

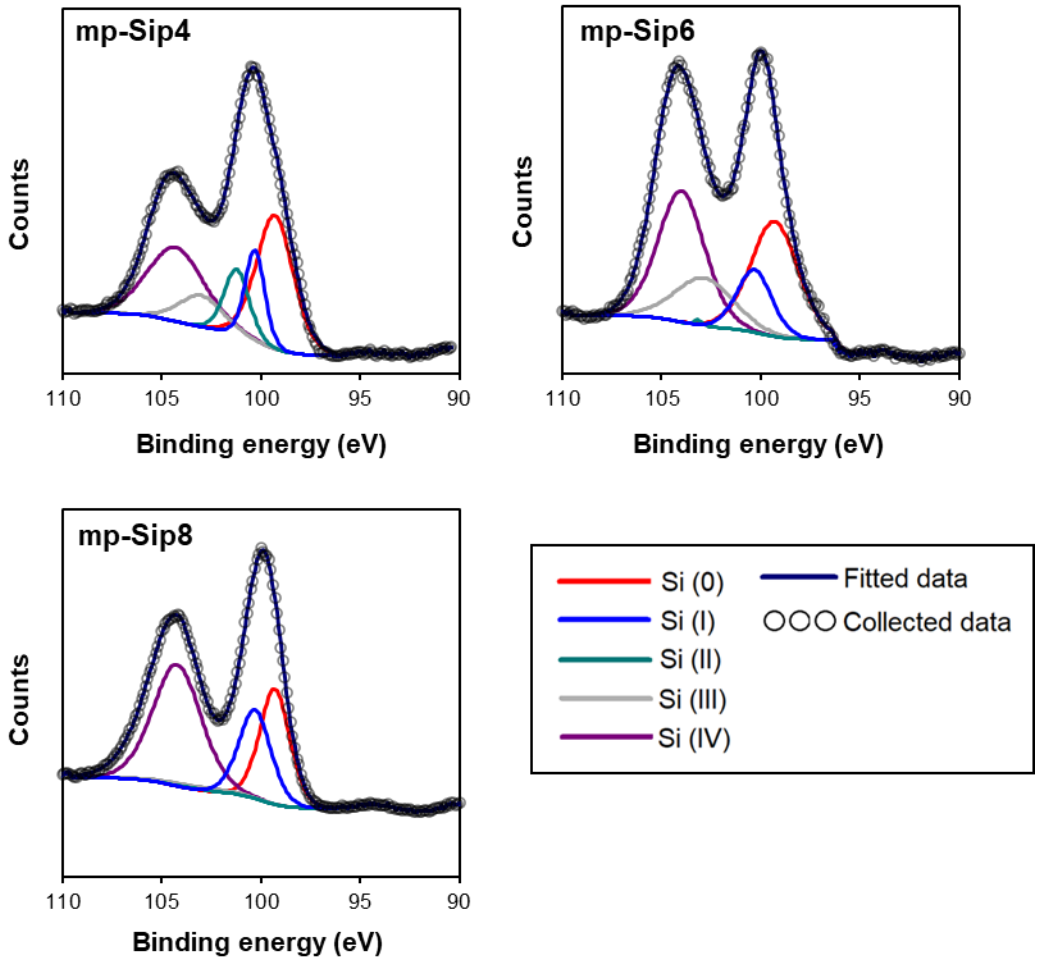

Figure 4. 6. High resolution XP spectra of the Si 2p region of mp-Si NPs prepared by magnesiothermic reduction using different SBA-15 precursors. For clarity, only the $2p_{3/2}$ peak of each oxidation state is shown.

Multipoint BET analysis was performed on both the SBA-15 precursors and on the mp-Si samples to characterize their surface area and porosity (summarized in Table 4.1). The specific surface areas of SBA-15_{4nm}, SBA-15_{6nm}, and SBA-15_{8nm} were 551, 473, and

610 m^2g^{-1}, respectively. The SSAs of mp-Sip4, mp-Sip6, and mp-Sip8 were 395, 401, and 321m^2g^{-1}, respectively. The surface areas of the mp-Si samples are decreased from those of the precursors, which is likely a result of pore collapse within the precursor structure. It is hypothesized that during magnesiothermic reduction, new mesopores are introduced within the pore walls, increasing the interconnectedness of the channels. The formation of these bridges between channels could eventually lead to a total collapse of the pore, resulting in a reduction in the surface area provided by the pore walls. In this case, the effect apparently negates any surface area added by the introduction of new mesopores, resulting in an overall decrease of the SSA. Correspondingly, the average pore size of these samples (estimated by DFT calculations) increased to 9.1, 10.5, and 12.6 nm, for the mp-Sip4, mp-Sip6, and mp-Sip8, respectively. The pore size distributions are also broadened from those of the precursors (Fig. 4.7), which is a typical result for mp-Si prepared via magnesiothermic reduction.[89] The mp-Sip8 sample also had a greater contribution from larger pores ranging between 20 – 50 nm compared to the other two mp-Si samples (Fig. 4.7). The N_2 adsorption analysis of the precursor samples showed Type IV adsorption-desorption isotherms with H1-type hysteresis (as classified by IUPAC), typical for SBA-15 SiO_2.[174] Similar results were seen for the mp-Si samples (Type IV adsorption-desorption with H1 hysteresis loop); however, adsorption within the range representative of mesopore filling ($P/P_o \sim 0.7 – 0.8$) occurs more gradually as a result of the larger average pore sizes (Fig. 4.8).

Table 4. 1. Specific surface area (using BET and DFT methods), DFT pore volume and pore width (mode value) of SBA-15 SiO_2 with varying pore sizes and of mp-Si NPs prepared from the different SBA-15 precursors.

	SBA-15$_{4nm}$	**SBA-15$_{6nm}$**	**SBA-15$_{8nm}$**	**mp-Sip4**	**mp-Sip6**	**mp-Sip8**
BET SSA ($m^2 g^{-1}$)	542	473	610	395	401	321
DFT SSA ($m^2 g^{-1}$)	593	461	537	317	337	267
Pore Volume ($cm^3 g^{-1}$)	0.52	0.53	0.98	0.62	0.72	0.75
Pore Width (nm)	6.1	6.1	8.1	9.1	10.5	12.6

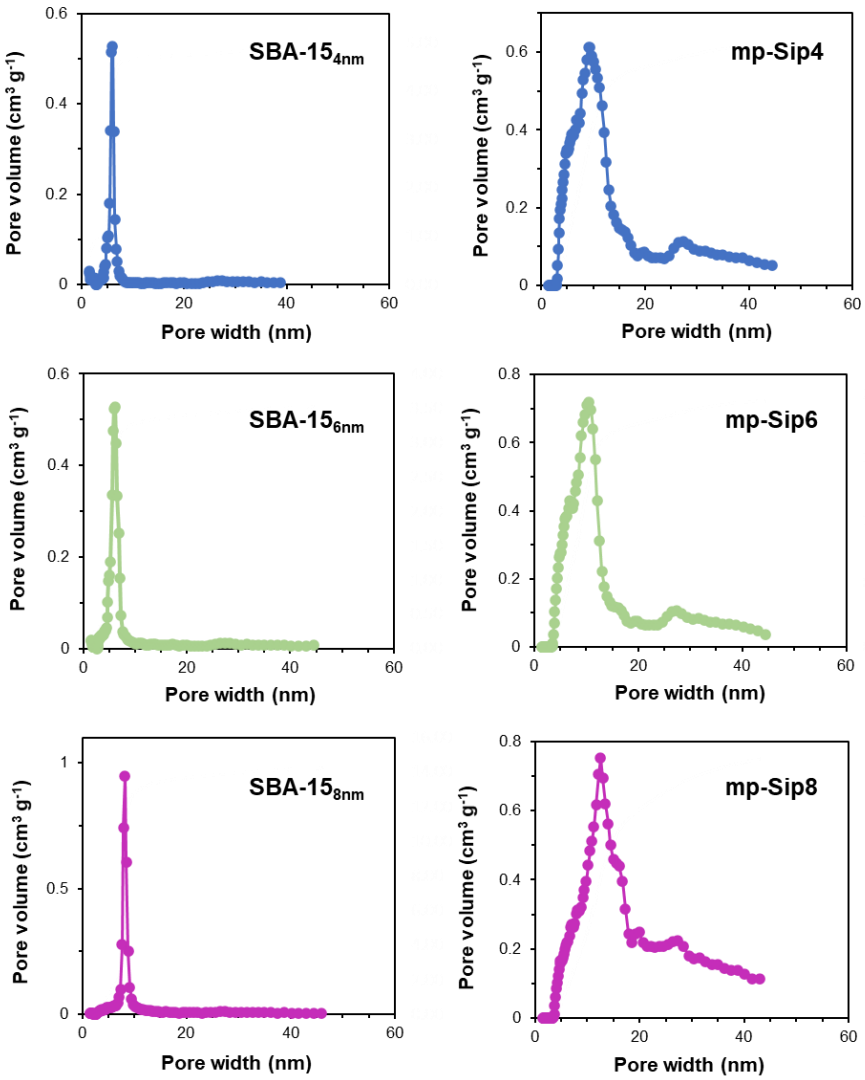

Figure 4. 7. Pore size distributions determined by DFT of SBA-15 SiO_2 with varying pore sizes and of mp-Si NPs prepared from the different SBA-15 precursors.

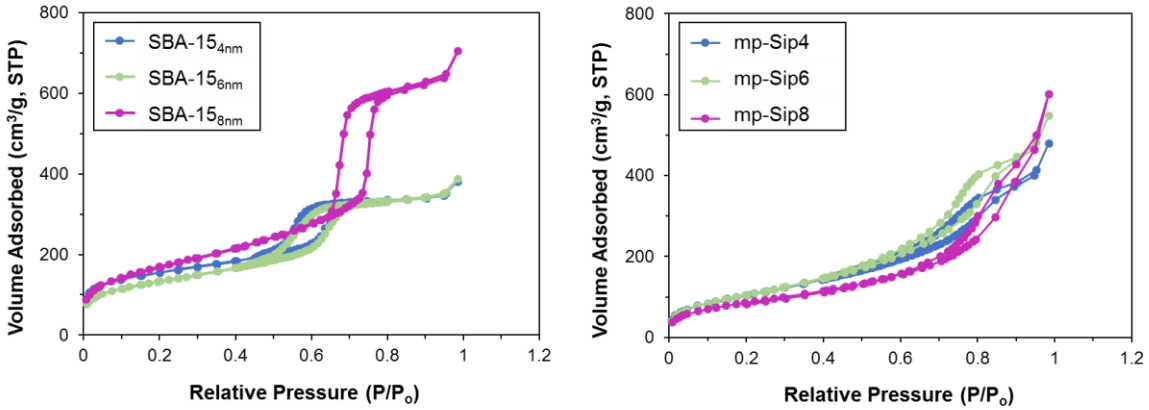

Figure 4. 8. BET N_2 adsorption isotherms of SBA-15 SiO_2 with varying pore sizes and of mp-Si NPs prepared from the different SBA-15 precursors.

Optical absorption measurements were performed on the mp-Si samples dispersed in EtOH, and their bandgaps were estimated using Tauc plots (Fig. 4.9). The bandgaps of mp-Sip4, mp-Sip6, and mp-Sip8 derived from the absorption measurements were all estimated to be ~1.38 eV. The broadened values compared to the bandgap of bulk Si (1.11 eV) are expected due to quantum confinement effects in the nanostructured mp-Si.[92,175,176]

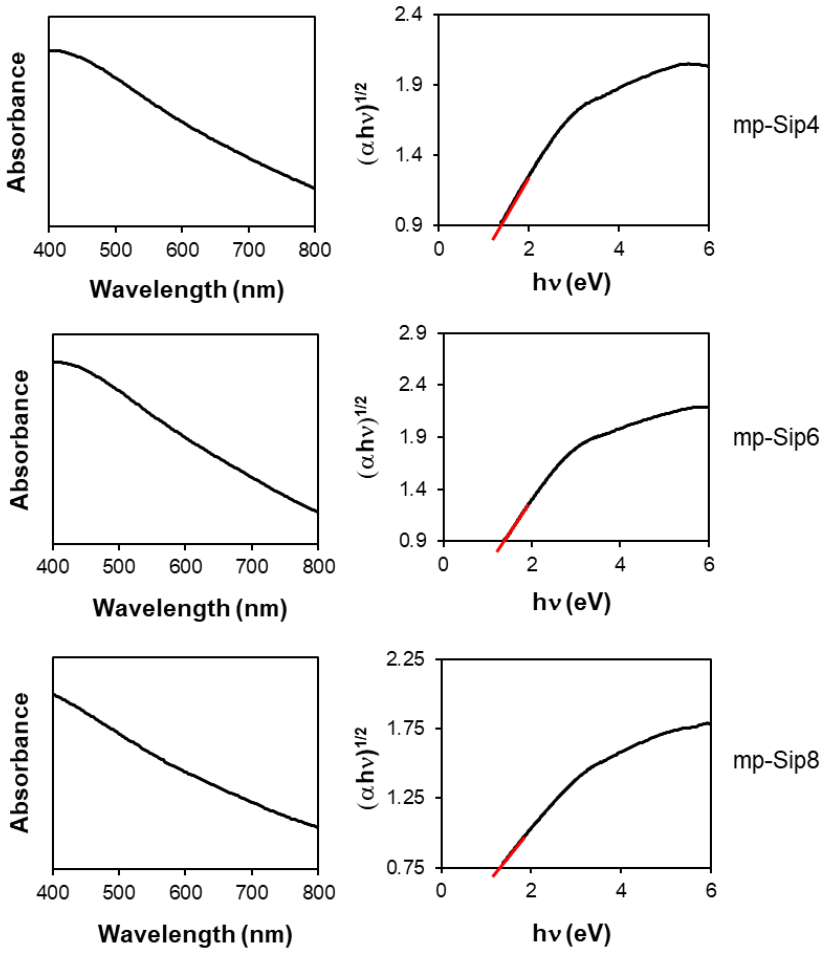

Figure 4. 9. UV-Vis absorbance spectra and corresponding Tauc plots of mp-Si NPs prepared by magnesiothermic reduction using different SBA-15 precursors with varying pore size.

4.3.2. Photocatalytic Hydrogen Evolution: Effect of Porosity

The photocatalytic H_2 evolution performance of the mp-Si samples was investigated under 100 mW cm^{-2} broadband illumination with CH_3OH as a hole scavenger. The amount of H_2 evolved over time was quantified using gas chromatography to give the H_2 evolution profiles shown in Fig. 4.10A. Of the three types of mp-Si, the highest H_2 evolution rates over a five-hour illumination period were observed for mp-Sip4, giving an

average rate of 3896 ± 736 µmol h^{-1} g^{-1} Si. An average H_2 evolution rate of 1672 ± 493 and 155 ± 86 µmol h^{-1} g^{-1} Si was observed for the mp-Sip6 and mp-Sip8, respectively. It is typically assumed for photocatalysts that a higher surface area provides more abundant catalytic sites, thereby enhancing the H_2 evolution performance. Surprisingly, the results of the present study do not reflect a trend to suggest that higher surface area leads to higher H_2 evolution rates when crystallinity is held constant. More notably, the photocatalytic performance decreases with an increase in average pore size of the mp-Si samples.

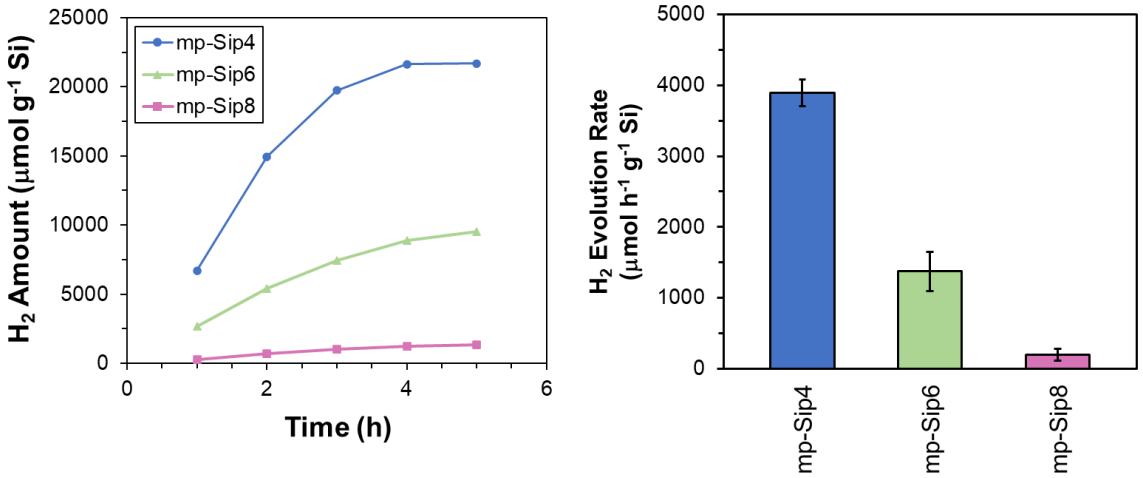

Figure 4. 10. (A) H_2 evolution profiles of mp-Si NPs prepared from different SBA-15 precursors under broadband illumination, (B) average H_2 evolution rates of the mp-Si NPs.

Surface oxides in nanostructured Si are known to introduce trap states which can deleteriously affect catalytic activity.[177–179] Based on XPS fits in the Si 2p region of the mp-Si NPs, the ratios between peak areas corresponding to Si oxide/suboxides and Si(0) were determined. The mp-Sip8 NPs had the highest ratio (2.6:1) of total Si oxide/suboxide (Si (+1, +2, +3 and +4) oxidation states) to Si(0). This is followed by ratios of 2.0:1 and

1.8:1 for the mp-Sip6 and mp-Sip4, respectively. The degree of surface oxidation in these samples likely influences their photocatalytic performance and is in part responsible for the trend in their H_2 evolution rates. The peak areas of each Si oxidation state were also individually compared to that of Si(0). Notably, the ratio of the Si(+4) to Si(0) peak area was 0.85:1, 1.1:1 and 1.7:1 for mp-Sip4, mp-Sip6 and mp-Sip8, respectively. It is possible that the larger pores allow for easier diffusion of oxygen within the structure, thus resulting in higher oxide amounts and lower photocatalytic activity.

The cycling ability of the mp-Si NPs was also evaluated (Fig. 4.11). For the mp-Sip4 and mp-Sip6 samples, a considerable drop in the photocatalytic activity was seen in cycle 2, followed by a slight decrease in the third cycle, which occurred after leaving the NPs suspended in water overnight. The decline in performance is a typical result for mp-Si photocatalysts, and results from surface oxidation occurring during each cycle.[166] Conversely, the mp-Sip8 NPs showed only a slight decrease in photocatalytic activity and maintained a similar level of performance through to the third cycle. Compared to the others, the mp-Sip8 NPs had the highest amount of surface oxide as well as the highest total atomic oxygen content according to EDS analysis. The already high oxygen content of the mp-Sip8 NPs likely prevented any further decrease of the H_2 evolution rate as a result of oxidation. On the other hand, oxidation of the mp-Sip4 and mp-Sip6 NPs following the first cycle caused a drop in their photocatalytic performance, resulting in H_2 evolution rates more like those seen for mp-Sip8.

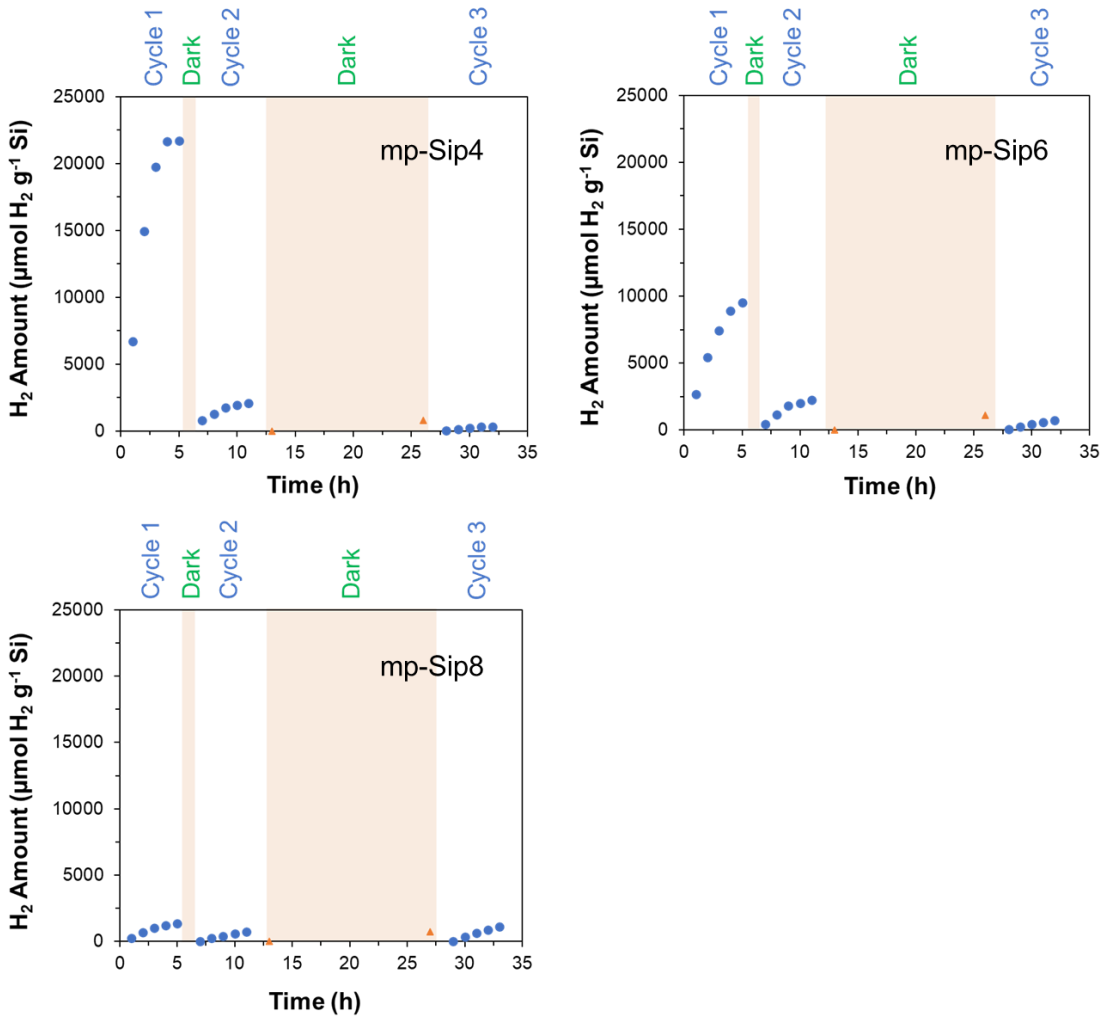

Figure 4. 11. Photocatalytic cyclability of mp-Si NPs prepared from different SBA-15 precursors. The cyclability was evaluated over two days with 5-hour illumination periods.

Based on the work of Chapter 3, it was hypothesized that the crystallinity of mp-Si NPs plays a bigger role compared to the amount of oxide in determining photocatalytic performance. In this study, the crystallinity of mp-Sip4, mp-Sip6 and mp-Sip8 is similar between samples, allowing for a closer investigation into the effects of oxidation, surface area and porosity. Specifically, the amount of surface oxide was found to influence the photocatalytic performance of these samples. The surface areas, however, did not correlate

to any trend in surface oxidation or to the H_2 evolution rates. Furthermore, the use of porous precursors did not result in mp-Si with higher surface area compared to when non-porous precursors are used. Previous work has shown that using the same reaction conditions with a non-porous precursor results in mp-Si with higher surface areas (527 ± 21 m^2g^{-1}) than those reported in this section.[89] These mp-Si NPs also show higher photocatalytic performance;[166] however, this is most likely a result of higher crystallinity and low oxide content. High surface area mp-Si NPs generally perform better as particulate photocatalysts compared to non-porous Si NPs;[176] however, it is likely that after a certain SSA value has been reached, further increase does not improve the catalytic activity.

The H_2 evolution rates of mp-Si NPs made from porous SBA-15 show a negative relationship with pore size. During magnesiothermic reduction, pore walls within the SBA-15 precursors probably collapse, resulting in larger pores while simultaneously reducing the area of exposed surface (depicted in Fig. 4.13). Although this corresponds to an overall decrease in the available surface area to oxidize, larger pores could influence the diffusion of atomic oxygen through the material and lead to faster surface oxidation. Pore size has been previously shown to influence the rate of oxygen diffusion into porous Si layers (*i.e.,* diffusion increases with pore size).[180] This theory would explain the trend in the present data, which shows that samples with a larger average pore size have a higher amount of surface oxide and lower H_2 evolution rate. SiO_2 precursors with a small average pore diameter (≤ 4 nm) or even non-porous precursors should be used to achieve higher H_2 evolution rates.

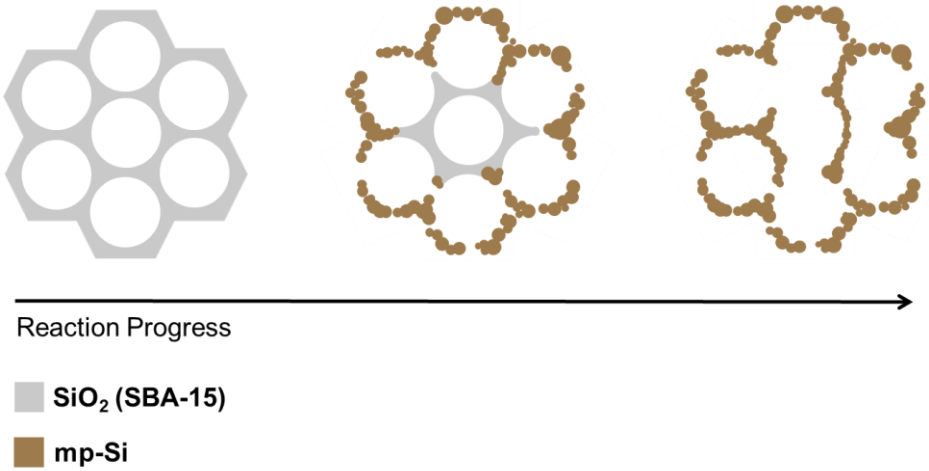

Figure 4. 12. Illustration depicting the collapse of pore walls within the porous structure of SBA-15 hypothesized to occur during magnesiothermic reduction. For simplicity, formation of the MgO by product is not shown.

4.4. Conclusions

The influence of precursor porosity on the photocatalytic performance of mp-Si NPs was investigated by synthesizing mp-Si from three different precursors (SBA-15) with pore sizes of 4, 6, and 8 nm. The mp-Si was prepared *via* magnesiothermic reduction using the same reaction conditions for each sample, resulting in NPs with a similar degree of crystallinity. The SSAs of the mp-Si NPs following magnesiothermic reduction were reduced from that of their corresponding precursor. Concurrently, the widths of the pores within each sample increased from their original size. Of the samples investigated, mp-Sip4 was the highest-performing photocatalyst with an H_2 evolution rate of 3896 ± 736 μmol h^{-1} g^{-1} Si, followed by mp-Sip6 and mp-Sip8, respectively. The trend in photocatalytic performance of the mp-Si NPs did not correlate with surface area; however, H_2 evolution rates were found to decrease with increasing pore size. Furthermore, samples with a larger

pore size were found to have a larger amount of surface oxidation, which is likely a major contributor to the trend in the H_2 evolution rates. Finally, this study revealed that the use of porous SBA-15 as a precursor does not lead to mp-Si NPs with larger surface areas compared to those made from a non-porous precursor (*i.e.*, Stöber SiO_2 spheres). Porosity in the precursor does not necessarily result in an improvement in photocatalytic performance of mp-Si NPs and may even be detrimental due to increased surface oxidation and lower crystallinity.

CHAPTER 5. Preliminary Studies on the Effects of the Magnesium Reagent and Addition of Nickel Cocatalysts*

5.1. Introduction

This chapter presents preliminary results from two projects investigating the photocatalytic H_2 evolution performance of mp-Si NPs. The first project explores methods to deposit Ni cocatalysts onto the mp-Si NPs, as well as the influence of the cocatalyst on the H_2 evolution rates achieved. The second project was motivated by a recent ban in Canada of the supply of Mg reagent used to synthesize the mp-Si NPs in Chapters 3 and 4. Mg reagents from different suppliers were used to investigate the effect of the Mg particle size used in magnesiothermic reduction on the photocatalytic performance of the resulting mp-Si.

5.1.1. The Influence of Cocatalysts on Photocatalytic Performance

The photocatalytic performance of most H_2 evolution photocatalysts is limited by the fast recombination rates of electron-hole pairs before migrating to the surface to participate in the desired chemical reactions. Additionally, surface reactions may be too slow to consume the photogenerated charges before recombination occurs. Metal cocatalysts deposited on the surface of photocatalyst particles can act as electron sinks to promote charge separation driven by junctions formed between the metal and the semiconductor.[25] In a typical system where the metal work function is larger than that of the semiconductor, Schottky junctions between the metal and the photocatalyst allow for irreversible transfer of CB electrons to the metal (Fig. 5.1). The formation of a depletion region at the interface prevents the electrons from passing back through the Schottky

* Photodeposition experiments in this chapter (section 5.2.6) were performed by Yiqi Lai.

barrier, creating efficient separation of electron-hole pairs.[181] Noble metals such as Pt, Pd, Au and Ag have been extensively employed as cocatalysts for the HER.[182] Of these, Pt has the largest work function (Table 5.1) which affords it the strongest ability to trap electrons.[181]

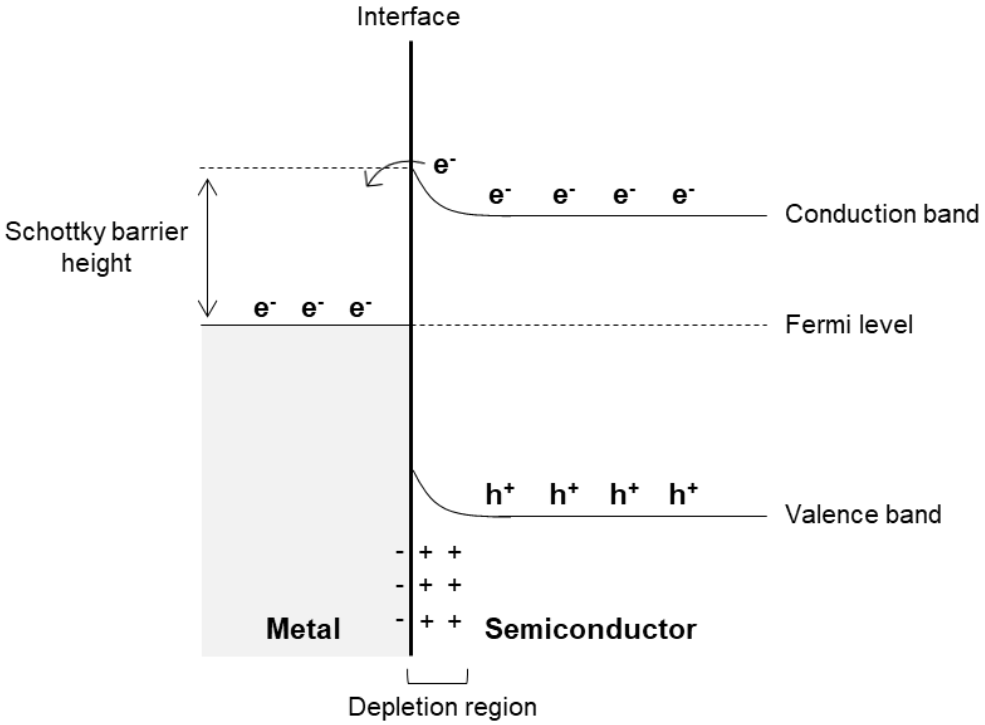

Figure 5. 1. Schematic of a Schottky junction formed between a semiconductor and a metal cocatalyst.

Table 5. 1. Work functions of various metals (obtained from ref. 183) having the ability to perform as cocatalysts for the HER.

Metal	Work Function (eV)[183]
Pt	5.65
Pd	5.12
Au	5.1
Ag	4.26
Co	5.0
Ni	5.15
Cu	4.65

Cocatalysts can also act as reaction sites which lower the activation energy and accelerate the kinetics of the HER. Proton reduction on cocatalysts occurs over two steps through an adsorbed intermediate (Eq. 5.1).[184] If the adsorption energy of the intermediate is too high, adsorption is slow. On the other hand, a low adsorption energy causes slow desorption to release H_2 (Sabatier's principle).[185] As such, cocatalysts showing moderate adsorption-desorption behaviour are best-suited to accelerate H_2 production.[8]

$$2e^- + 2H^+ \rightarrow 2[H_{ads}] \rightarrow H_2 \qquad \text{Eq. 5.1}$$

The cocatalyst loading amount tends to show a volcano-like trend with the photocatalytic activity of a given catalyst (Fig. 5.2). Introduction of the cocatalyst gradually improves the photocatalytic activity to a maximum, while at higher loading beyond the maximum the activity decreases. Although certain cocatalysts can act as active sites for H_2 evolution, high cocatalyst loading can block surface active sites on the photocatalyst from

interacting with sacrificial reagents and water molecules. Additionally, cocatalyst particles may shield the semiconductor from incident light, hindering light absorption.[25]

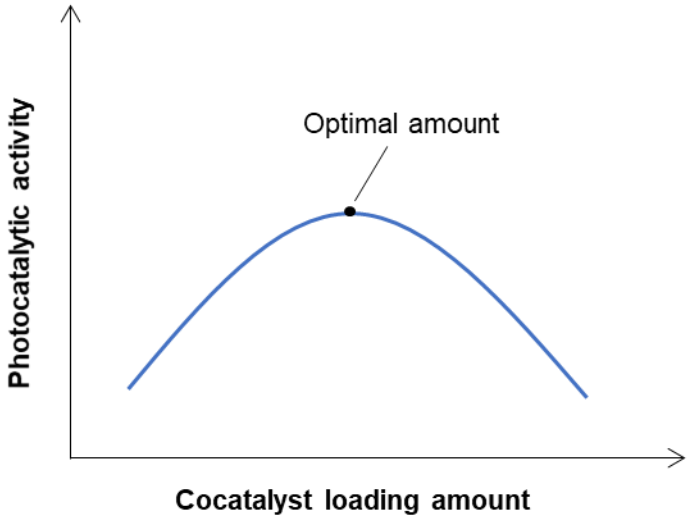

Figure 5. 2. Volcano-type relationship between the cocatalyst loading amount and photocatalytic activity.

Pt is one of the most widely used cocatalysts for H_2 evolution due to its high work function and favourable adsorption-desorption behaviour.[185] However, the high price and scarcity of Pt (along with other noble metals) warrants investigations into more earth-abundant metal cocatalysts. Earth-abundant and low-cost transition metals such as Ni, Co and Cu have been investigated as cocatalysts for photocatalytic H_2 production on various materials.[25] Ni is an attractive alternative to Pt due to its high work function and low overpotential for the HER.[186] Ni has been shown to enhance the photocatalytic H_2 evolution activity of TiO_2,[187–190] g-C_3N_4,[191,192] and other photocatalyst materials.[193–196] Besides Ni metal, Ni oxides (NiO and NiO_x) and Ni/NiO core shell particles have also been shown to promote H_2 evolution.[25,193,194]

Metal cocatalysts are typically deposited through the reduction or decomposition of salt precursors, which can be achieved by a variety of methods.[25] The optimal method may depend on the nature of the photocatalyst substrate. The deposition method can also affect the spatial distribution and physical characteristics of the cocatalyst, which can influence the photocatalytic performance. For instance, both the crystallinity[197] and distribution[198] (influenced by the deposition method) of Pt NPs on g-C_3N_4 have been shown to affect H_2 evolution. Loading of Ni cocatalysts has been reported by incipient wetness impregnation and calcination,[192,194] photodeposition (either as a pre-treatment[188,195,199] or *in-situ*[187,190,194]), and by chemical reduction methods.[189,193]

To date, reports of mp-Si NPs for photocatalytic H_2 evolution from water have not included investigations into the effect of metal cocatalysts. The work in Chapters 3 and 4 of this thesis has shown that mp-Si NPs are active for H_2 evolution without the need for cocatalysts. However, incorporation of a cocatalyst could further enhance their performance. In this chapter, Ni was investigated a cheap and earth-abundant cocatalyst for mp-Si. The work presented focussed on developing an appropriate method for Ni deposition on the mp-Si photocatalysts. Deposition by calcination, photodeposition, and chemical reduction was investigated to prepare mp-Si with various Ni loading amount. The photocatalytic performance of these samples was screened to help identify the most promising deposition method for future studies.

5.1.2. Effect of the Magnesium Reagent used to Synthesize Mesoporous Silicon

Magnesiothermic reduction is a solid-state method, and the reaction rates rely on factors such as the contact area between the reagents. In general, smaller particle sizes lead to higher surface area and increased contact between reagents. As such, particle sizes can

influence the rate of the reaction, which can in turn affect characteristics of the product. The effect of the Mg particle size on mp-Si synthesized by magnesiothermic reduction has been previously investigated by Yang and coworkers.[105] Their work showed that smaller Mg particles led to faster reaction and large amounts of localized heat accumulation, which resulted in excess sintering and fusion in the mp-Si product. In this chapter, Mg reagents with larger (71 ± 25 μm) and smaller (28 ± 16 μm) particle sizes were used to synthesize mp-Si NPs. This changed the trend observed in the H_2 evolution rates for mp-Si synthesized at different reaction temperatures from that reported in Chapter 3. The mp-Si photocatalysts were characterized by XRD, SEM, EDS, Raman, and XPS to gain insight into the effect of the Mg particle size on the mp-Si properties.

5.2. Experimental Methods

5.2.1. Materials

Ammonium hydroxide (28% NH_3) was purchased from Alfa Aesar. The magnesium –325 mesh powders (Mg-S and Mg-S2) were purchased from Alfa Aesar and Oakwood Chemicals Inc., respectively. Mg powder < 0.1 mm (97.0%), tetraethyl orthosilicate (TEOS, 99.9%), hydrochloric acid (HCl, 37%), sodium borohydride ($NaBH_4$), methanol, and ethanol (95% and 100%) were purchased from Sigma-Aldrich. Nickel (Ni) salts ($Ni(OAc)_2{\cdot}4H_2O$ and $Ni(NO_3)_2{\cdot}6H_2O$) were purchased from Fisher Scientific. All reagents were used as received without further purification. Deionized water was obtained from an Arium Ultrapure Water System.

5.2.2. Materials Characterization

Powder XRD, SEM, EDS, Raman, and XPS were conducted as discussed in section 2.2. Particle size analysis was performed on SEM images using Image J software.

5.2.3. Magnesiothermic Reduction of Silica Nanoparticles

The mp-Si NPs were prepared as discussed in sections 2.1.2 and 3.2.3.

5.2.4. Nickel Deposition by Calcination

Dry mp-Si powder was mixed with just enough CH_3OH (~10 mL) to disperse the NPs, followed by a pre-determined amount of 7 mM methanolic nickel (II) acetate ($Ni(OAc)_2$) solution. The dispersion was sonicated for 10 min to ensure thorough mixing of the mp-Si NPs with the Ni salt. The solid was collected after drying in an oven at 100 °C, then calcined under H_2/Ar (5% H_2) flow at 350 °C for 3 h in a tube furnace. The control sample (0 wt% Ni) was prepared following the same procedure but without the addition of $Ni(OAc_2)$ solution.

5.2.5. Photodeposition of Nickel

The mp-Si powder was transferred to the reaction vessel which was then flushed with N_2 gas for 0.5 h. The desired volume of 50 mM $Ni(OAc)_2$ in CH_3OH was bubbled with N_2 for 0.5 h, then added to the reaction vessel under N_2 flow. The mixture was stirred and irradiated with UV light for 2, 4 or 24 h. The NPs were then collected by centrifugation and washed twice with distilled water before drying from acetone in an oven.

5.2.6. In-Situ Photodeposition of Nickel

The photocatalysis procedure outlined in section 2.3 was slightly modified to include the addition of Ni salt. An aqueous stock solution of $Ni(NO_3)_2$ (0.1 or 10 mM) was bubbled with N_2 gas for 0.5 h. The desired volume of $Ni(NO_3)_2$ solution was measured out then topped up to 30 mL with the N_2-bubbled water. This was added to the reaction vessel containing mp-Si, along with 5 mL of the N_2-bubbled CH_3OH (as in section 2.3). Following the experiment, the Ni-decorated mp-Si NPs were collected for characterization by drying the reaction mixture overnight in an oven at 100 °C.

5.2.7. Nickel Deposition by Chemical Reduction

Dry mp-Si powder was dispersed in 10 mL of distilled water by sonication. The desired amount of 10 mM aqueous nickel (II) nitrate ($Ni(NO_3)_2$) solution was added to the dispersion with stirring. 3 mg of $NaBH_4$ was dissolved in 1 mL of cold water, which was then quickly added to the NP dispersion. Within a few seconds, the dispersion turned from light brown to a darker brownish black. The mixture was left to stir for 2 min, then collected by centrifugation, washed twice with distilled water and collected in a minimal amount of acetone. The product was transferred to inert atmosphere immediately after drying to prevent oxidation. The control sample (0 wt% Ni) was prepared following the same procedure but without the addition of $Ni(NO_3)_2$.

5.2.8. Photocatalytic Hydrogen Evolution

Photocatalytic experiments were performed as discussed in section 2.3.

5.3. Results and Discussion

5.3.1. Deposition of Nickel Cocatalysts and their Influence on Photocatalytic Performance

Calcination Method.

For optimal performance of mp-Si during photocatalytic H_2 evolution, Ni NPs or clusters must be deposited onto the surface of the photocatalysts. This can be achieved *via* reduction of Ni salts by calcination, chemical reduction or photoreduction methods. $Ni(OAc)_2$ is known to decompose to Ni under reducing atmosphere above 300ºC.[200] As such, Ni deposition was attempted by calcinating mp-Si NPs with $Ni(OAc)_2$ under 5% H_2 flow. Photocatalysts containing 0.1, 0.5 and 1 wt. % Ni were prepared by this method. Photocatalytic experiments revealed a drop in the H_2 evolution rates for all samples compared to the original unmodified mp-Si (Table 5.2). A slight increase in the H_2 evolution rate occurs from 0.1 to 0.5 wt. % Ni; however, given the standard deviation of the unmodified mp-Si (Table 5.2) this difference may be negligeable and requires replicate studies to confirm the trend. Furthermore, no Ni was detected using XRD, XPS or EDS characterization techniques. In another experiment, a much higher amount of $Ni(OAc)_2$ was added before heat treatment (75 wt. % Ni). EDS analysis showed an average Ni amount of 32 ± 11 wt. %, indicating that much of the Ni is lost during the procedure.

A control sample (0 wt. % Ni) was prepared following the same method (*i.e.*, sonicating in CH_3OH followed by heating) but without the addition of $Ni(OAc)_2$ solution. A similar drop in the H_2 evolution rate for the control was observed. The Si 2p region of

the XP spectra for the calcined samples (Fig. 5.3) showed that the mp-Si was highly oxidized, which could account for the decrease in photocatalytic performance. Given that the particles were calcined under reducing (H_2) atmosphere, it is unlikely that oxidation occurred during the heating step; however, oxidation could have occurred during the mixing and drying process prior to calcination. Other possible explanations for the decrease in catalytic activity could include morphological damage to the mp-Si as a result of calcination or the presence of carbon impurities remaining from the acetate. Immediate future work should include microscopy analysis to discern whether changes to the mp-Si morphology occurred during the Ni deposition procedure.

Table 5. 2. H_2 evolution rates achieved over a 3 h illumination period using mp-Si modified with Ni deposited by the annealing method. The H_2 evolution rate for the unmodified mp-Si sample is reported as the average (± standard deviation) of four photocatalytic experiments.

Sample	H_2 Evolution Rate (μmol h^{-1} g^{-1} Si)
Unmodified mp-Si	4747 ± 704
mp-Si/0wt% Ni (control)	700
mp-Si/0.1wt% Ni	720
mp-Si/0.5wt% Ni	1110
mp-Si/1wt% Ni	1083

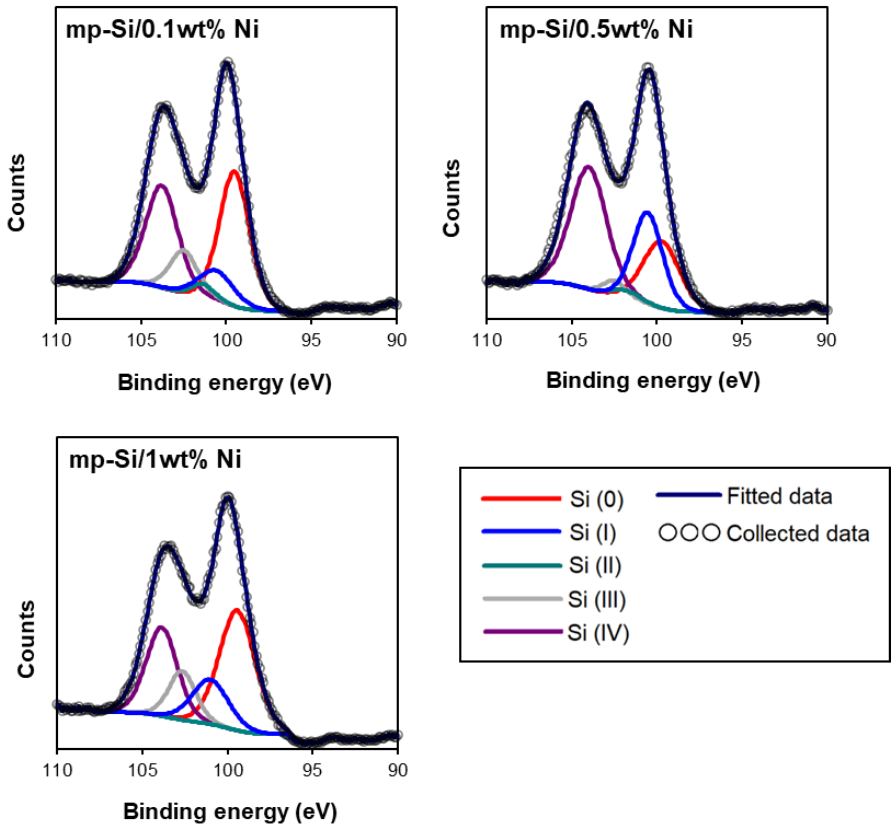

Figure 5. 3. High resolution XP spectra of the Si 2p region of mp-Si NPs calcined with $Ni(OAc)_2$. For clarity, only the $2p_{3/2}$ peak of each oxidation state is shown.

Photodeposition.

The deposition of metal cocatalysts onto semiconductor surfaces can also be achieve *via* photodeposition, whereby metal salts are reduced by photoexcited electrons in the CB. This method was first attempted by irradiating methanolic dispersions of mp-Si containing $Ni(OAc)_2$, then collecting the product before evaluating its photocatalytic performance. Unfortunately, this process killed the catalytic activity of mp-Si, likely due to oxidation that occurred during photodeposition. Furthermore, long reaction times (24 h)

were required to achieve any detectable Ni even when a high amount of Ni (75 wt. %) was used. EDS analysis revealed the actual amount of Ni in this sample to be less than 1 wt. %.

In-situ photodeposition, also referred to as the salt additive method, has been reported for various metal cocatalysts in literature reports.[182,201] In one example, Wang *et al*. reported enhanced H_2 evolution from water on TiO_2 by simply adding $Ni(NO_3)_2$ to the photocatalytic reaction.[190] Their findings suggested that Ni^{2+} ions adsorbed onto the TiO_2 surface are reduced by CB electrons, resulting in Ni clusters on the surface that act as cocatalysts to drive the HER. To test this, photocatalytic experiments were performed after adding enough $Ni(NO_3)_2$ to achieve the desired Ni amount (0.2, 0.5, 1 and 5 wt. %). The Ni 2p region in the XP spectra of the mp-Si/1wt% Ni and mp-Si/5wt% Ni samples (Fig. 5.4) showed the presence of Ni(+2) $2p_{3/2}$ and $2p_{1/2}$ peaks at ~854.5 and ~871.9 eV, respectively, as well as characteristic satellite peaks.[202] The characteristic $2p_{3/2}$ peak for Ni(0) (853.1 eV) was not observed. The photocatalyst samples had to be collected from the reaction vessel following a photocatalytic experiment to be characterized, so any Ni^0 present would likely oxidize during this process. As such, the oxidation state of Ni observed by XPS may not be representative of the oxidation state present during photocatalysis. The average Ni amount was determined by EDS to be 2 ± 0.2 and 7 ± 1 wt. % Ni for the mp-Si/1wt% Ni and mp-Si/5wt% Ni samples, respectively. However, no conclusions can be drawn from these results as to whether the Ni^{2+} in the reaction mixture was successfully deposited as Ni^0 onto the surface of mp-Si. Ni was not detected in the 0.5 or 0.2 wt. % Ni samples by either XPS or EDS.

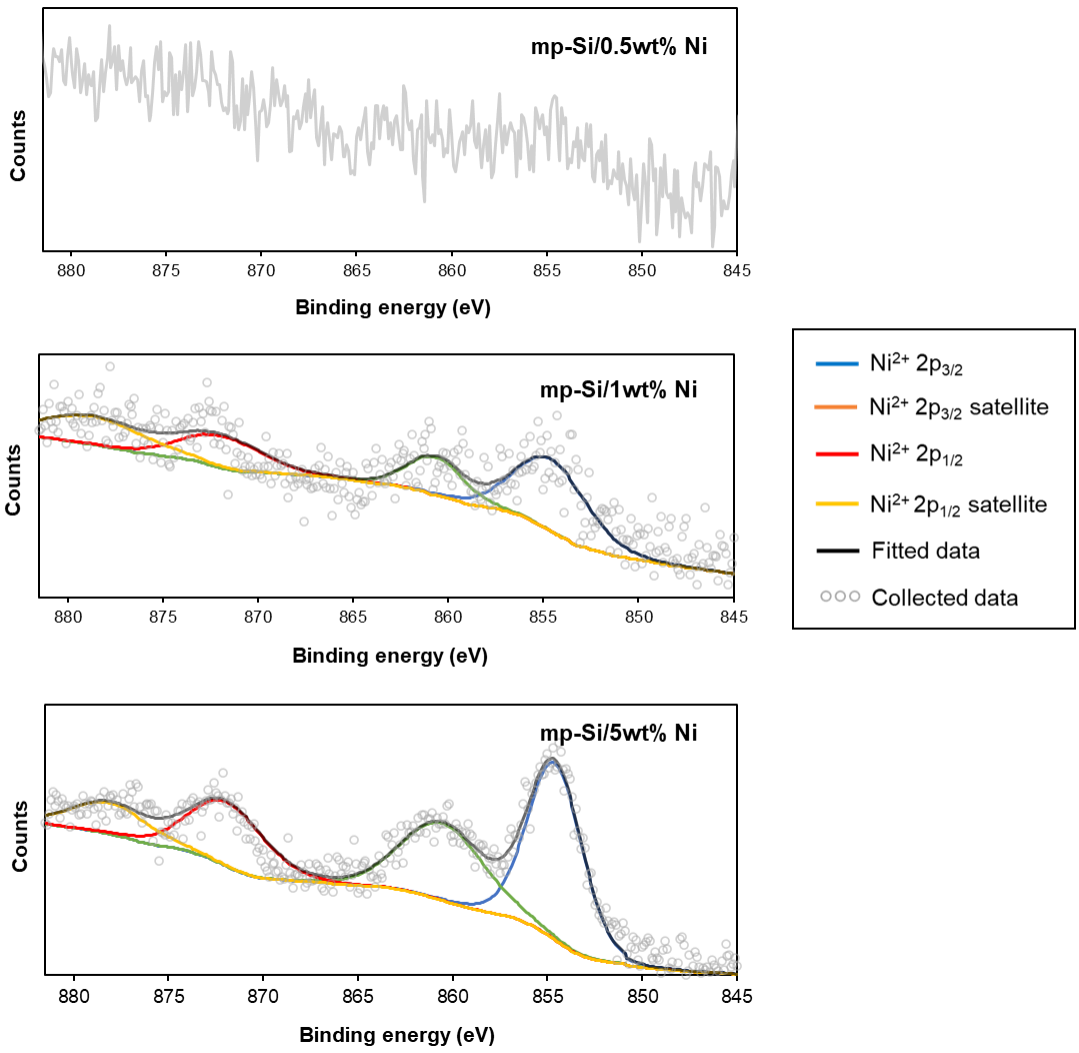

Figure 5. 4. High resolution XP spectra of the Ni 2p region of mp-Si NPs following *in-situ* photodeposition of Ni.

The H_2 evolution rates for the mp-Si NPs tested with and without $Ni(NO_3)_2$ additive are shown in Table 5.3. The highest H_2 evolution rate (2533 µmol h^{-1} g^{-1} of Si) was observed for the mp-Si/0.2wt% Ni sample, however the rate is still decreased from that of unmodified mp-Si NPs from the same batch. One hypothesis for this observation is that the reduction of Ni^{2+} during photocatalysis contributes to faster oxidation of the mp-Si, which hinders the catalytic activity. This is supported by the Si 2p regions of the XP spectra (Fig.

5.5), which show very high amounts of surface oxide on the mp-Si following *in-situ* photodeposition. The H_2 evolution rates are further decreased as the Ni amount increases from 0.5 to 1 to 5 wt. %, following the expected trend for optimal cocatalyst loading.

Table 5. 3. H_2 evolution rates achieved over a 5 h illumination period with and without $Ni(NO_3)_2$ additive. The H_2 evolution rate for the mp-Si sample without $Ni(NO_3)_2$ is reported as the average (± standard deviation) of three photocatalytic experiments.

Sample	H_2 Evolution Rate (μmol h^{-1} g^{-1} Si)
mp-Si (no $Ni(NO_3)_2$)	3926 ± 403
mp-Si/0.2wt% Ni	2533
mp-Si/0.5wt% Ni	1644
mp-Si/1wt% Ni	1483
mp-Si/5wt% Ni	970

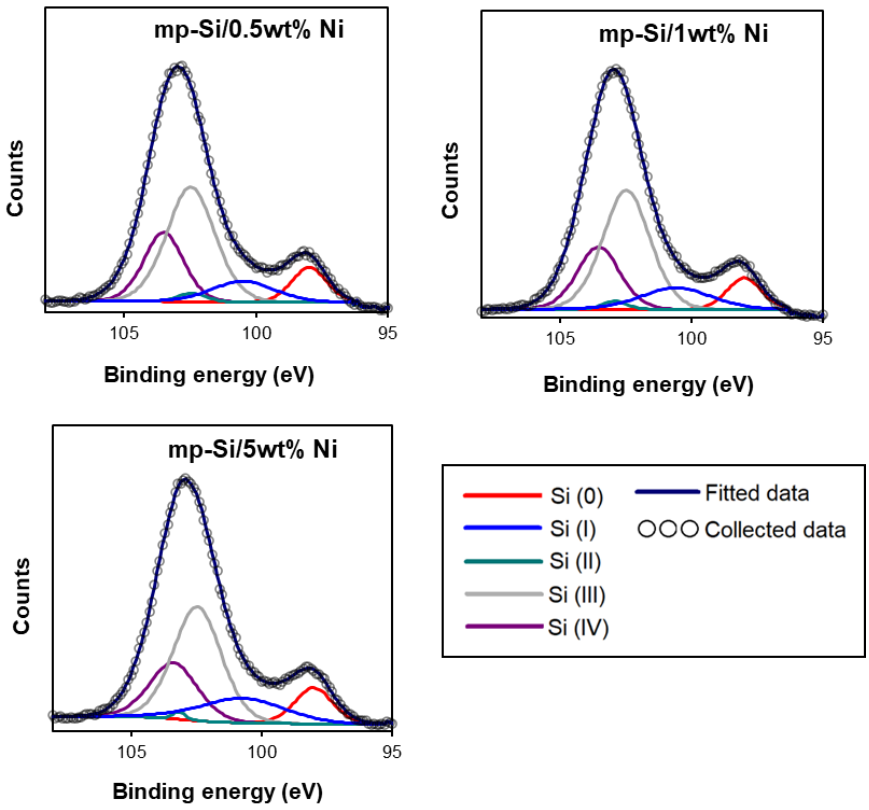

Figure 5. 5. High resolution XP spectra of the Si 2p region of mp-Si NPs following *in-situ* photodeposition of Ni. For clarity, only the $2p_{3/2}$ peak of each oxidation state is shown.

Chemical Reduction Method.

Chemical reduction of salt precursors using $NaBH_4$ is a popular method for depositing metal cocatalysts. $NaBH_4$ has also been used as a reducing agent to prepare isolated Ni NPs from $Ni(NO_3)_2$.[203] The chemical reduction method was explored to prepare mp-Si NPs with 1 and 5 wt. % Ni, along with a control (0 wt. % Ni). After the addition of $NaBH_4$ to an aqueous mp-Si suspension containing $Ni(NO_3)_2$, the mixture turned a dark brownish black color, indicating the reduction of Ni^{2+} to Ni^0.[203] However, no Ni was detected in the collected samples by XRD, XPS, or EDS, likely due to the loss of Ni during the isolation steps, and lower actual wt. % Ni in the final product. The H_2 evolution rates

for the mp-Si samples before and after Ni deposition are shown in Table 5.4. Due to a lack in supply of reagents needed to prepare high-performing mp-Si at the time of these experiments, the H_2 evolution rates are lower than those typically reported. Nonetheless, the effects of Ni deposition could still be observed.

Table 5. 4. H_2 evolution rates achieved over a 3 h illumination period using mp-Si modified with Ni deposited by chemical reduction with $NaBH_4$. The H_2 evolution rate for the unmodified mp-Si sample is reported as the average (± standard deviation) of three photocatalytic experiments.

Sample	H_2 Evolution Rate (μmol h^{-1} g^{-1} Si)
Unmodified mp-Si	429 ± 57
mp-Si/0wt% Ni (control)	398
mp-Si/1wt% Ni	585
mp-Si/5wt% Ni	399

Compared to the unmodified mp-Si, no significant change (beyond the standard deviation) was observed in the H_2 evolution rates for the mp-Si/1wt% Ni as well as the control sample. However, a slight increase (~36 %) was seen in the rate for the mp-Si/5wt% Ni sample. Unfortunately, the need for large amounts of mp-Si starting material and low yields of Ni-decorated mp-Si after processing prevented further studies. Replicate experiments are required to confidently assign trends to the data.

5.3.2. Summary of Nickel Deposition Methods

In theory, Ni should have the ability to act as a cocatalyst for the HER of water splitting. However, in order to enhance the photocatalytic performance of mp-Si, an optimal Ni deposition method must be developed. Some advantages and disadvantages of the methods attempted in this chapter are outlined in Table 5.5. Both calcination and photodeposition, while simple to perform, resulted in a loss of photocatalytic activity that could be attributed to the method itself and not necessarily the amount of Ni. The simplest method to perform was *in-situ* photodeposition, which required no additional processing prior to the photocatalytic experiment. Therefore, the experiments could be completed relatively quickly and only using a small amount of mp-Si (10 mg) each time. However, the photocatalytic performance was worsened for the Ni amounts tested, and the nature of the method limits the ability to test lower wt. % Ni without modifying the setup to upscale the amount of mp-Si.

The chemical reduction method, while more tedious and wasteful compared to other methods, gave the most promising results for photocatalytic enhancement. Future work should focus on replicating the results presented herein using high-performing mp-Si samples (*i.e.*, with comparable H_2 evolution rates to those discussed in Chapter 3). Detailed microscopy analysis should be performed to determine the size and morphology of the Ni NPs/clusters and to verify their deposition onto the photocatalyst surface. Furthermore, higher Ni amounts (10 wt. % and higher) should be investigated since the actual Ni amount in the product is likely much lower than what is added during deposition (suggested by the lack of Ni detection by XPS or EDS).

Table 5. 5. Summary of advantages and disadvantages associated with the Ni deposition methods attempted for mp-Si NPs.

Deposition Method	Advantages	Disadvantages
Calcination	- Simple to perform	- Inefficient deposition (Ni lost) - Procedure results in loss of catalytic activity
Photodeposition	- Simple to perform	- Inefficient deposition - Procedure results in loss of catalytic activity
In-situ photodeposition	- Very simple to perform, no additional workup required	- Decrease in H_2 evolution rates at Ni wt. % $\geq$ 0.5 - Difficult to achieve low Ni wt. % without upscaling reaction
Chemical reduction	- Procedure does not negatively impact catalytic activity	- Tedious procedure - Inefficient deposition - Low yield due to loss of material during processing

5.3.3. Effect of the Magnesium Reagent used to Prepare Mesoporous Silicon

Due to a recent ban of supply to Canada of the Mg reagent (–325 mesh powder from Alfa Aesar, Sigma, and Fisher) used for the mp-Si syntheses discussed in Chapters 3 and 4, new Mg reagents with different particle size distributions were needed to synthesize mp-Si photocatalysts for further studies. The Mg particle size is expected to affect the reagent mixing, contact area between the reactants, and heat accumulation during magnesiothermic reduction, which could in turn influence the properties of the mp-Si formed.[105] Therefore, the influence of the Mg reagent on photocatalytic performance for mp-Si prepared using the new Mg reagents was briefly investigated and is discussed in this section.

Mg reagents obtained from Alfa Aesar (–325 mesh), Oakwood Chemicals Inc. (–325 mesh) and Sigma-Aldrich (< 0.1 mm) were imaged by SEM to verify the difference in

their particle size distributions (Fig. 5.6). The images clearly show that on average, smaller particles are seen in the–325 mesh Mg (Fig. 5.6A and C) than in the < 0.1 mm Mg (Fig. 5.6B). Average particle sizes were estimated using Image J to be 35 ± 13 and 71 ± 25 µm, respectively, for Mg powders obtained from Alfa Aesar and Sigma Aldrich. For the remainder of this section, the Mg reagents are denoted Mg-S and Mg-L for the smaller (Alfa Aesar, –325 mesh) and larger (Sigma-Aldrich, < 0.1 mm) Mg powders, respectively.

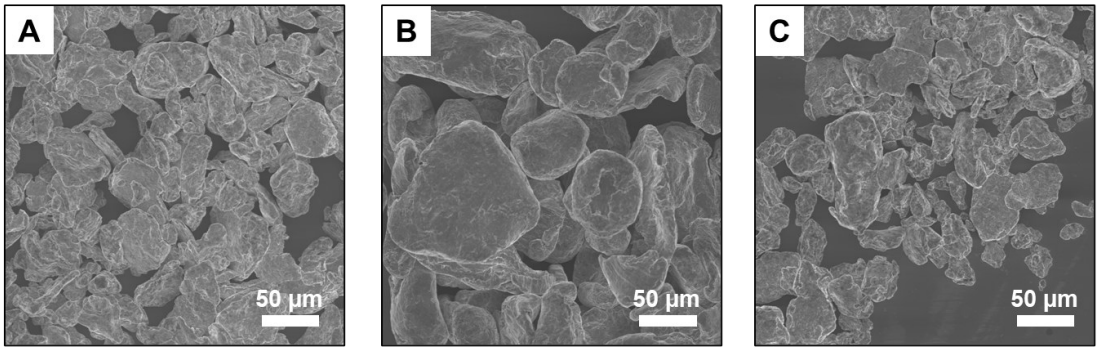

Figure 5. 6. SEM images of magnesium reagents (A) Mg-S, (B) Mg-L, and (C) Mg-S2 used to prepare mp-Si by magnesiothermic reduction.

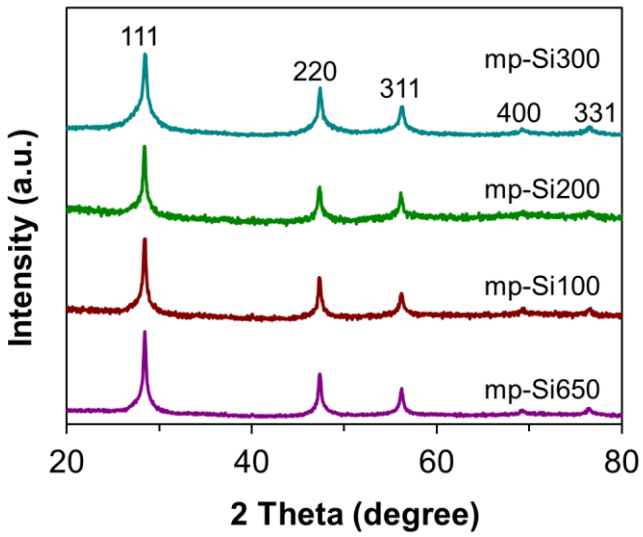

Figure 5. 7. Powder XRD patterns of mp-Si NPs prepared under different magnesiothermic reduction conditions using Mg-L.

Mg-L was used to prepare mp-Si NPs using single temperature heating at 650 °C for 3 h (mp-Si650) as well as the two-temperature heating method (mp-Si100, mp-Si200 and mp-Si300) outlined in the previous sections. The powder XRD patterns (Fig. 5.7) showed the characteristic reflections of crystalline Si. The photocatalytic performance of these samples was screened *via* water splitting under 100 mW cm^{-2} broadband illumination with MeOH as a hole scavenger. The H_2 evolution rates for these samples are presented in Fig. 5.8. The highest H_2 evolution rate; 6747 µmol h^{-1} g^{-1} of Si, was seen for the mp-Si200 sample. H_2 evolution rates of 1125, 1978 and 1888 µmol h^{-1} g^{-1} of Si were seen for the mp-Si100, mp-Si300 and mp-Si650 NPs, respectively. Evidently, the photocatalytic performance of mp-Si NPs prepared using Mg-L under the different annealing conditions does not follow the same trend as those prepared using Mg-S in Chapter 3.

Throughout this work, average H_2 evolution rates are typically reported for a single batch of mp-Si NPs prepared in one synthesis with a given set of reaction conditions. However, reasonable reproducibility in the rates for mp-Si from different batches (*i.e.,* separate syntheses using the same reaction conditions) was typically seen when Mg-S was used as the reagent (Table 5.7). On the contrary, mp-Si NPs prepared using Mg-L were found to have lower reproducibility between NPs synthesized in different batches. Table 5.6 shows H_2 evolution rates for three different batches of the highest performing photocatalysts prepared using Mg-S (mp-Si300) and Mg-L (mp-Si200). A larger standard deviation is seen between the rates for samples prepared from Mg-L compared to those prepared using Mg-S.

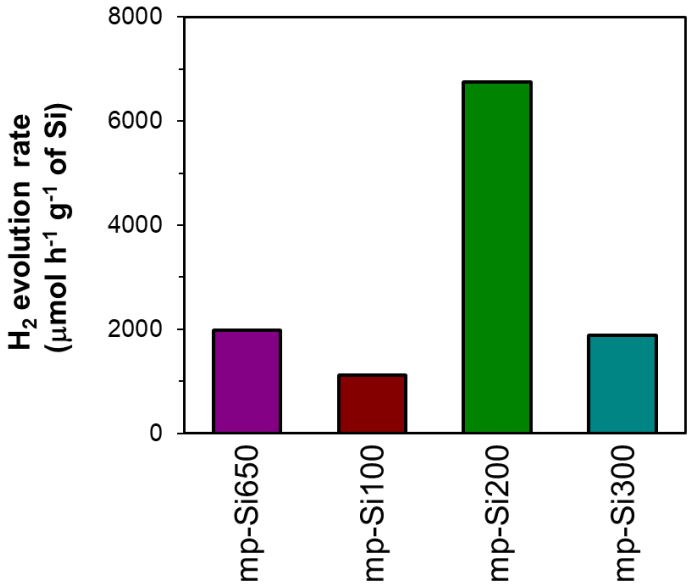

Figure 5. 8. Average H_2 evolution rates for mp-Si NPs prepared using Mg-L.

Table 5. 6. H_2 evolution rates obtained from three different batches of mp-Si NPs prepared using Mg-S (mp-Si300) and Mg-L (mp-Si200).

	mp-Si300 prepared using Mg-S		**mp-Si200 prepared using Mg-L**	
	H_2 Evolution Rate ($\mu mol\ h^{-1}\ g^{-1}$ Si)	**Average H_2 Evolution Rate ± Std. Dev.** ($\mu mol\ h^{-1}\ g^{-1}$ Si)	**H_2 Evolution Rate** ($\mu mol\ h^{-1}\ g^{-1}$ Si)	**Average H_2 Evolution Rate ± Std. Dev.** ($\mu mol\ h^{-1}\ g^{-1}$ Si)
Batch 1	5021	4947 ± 226	2542	5076 ± 2232
Batch 2	5127		5940	
Batch 3	4693		6747	

The mp-Si NPs prepared using Mg-L were characterized using SEM, XPS, and Raman spectroscopy to gain further insight into the effect of the Mg reagent on the mp-Si properties. As expected, morphological damage is observed in the mp-Si650 sample by SEM analysis (Fig. 5.9). Some possible morphological damage is also observed in the mp-Si300 and mp-Si200 samples, as well as what appears to be some unreacted SiO_2 (smooth particles). A larger amount of these smooth particles is observed in the mp-Si100. Raman (Fig. 5.10) was used to compare the crystallinity of the different mp-Si NPs made using Mg-L. The degree of crystallinity was found to increase slightly with higher annealing temperature. Based on XPS analysis (Fig. 5.11), all four samples had a relatively high amount of surface oxide, with the lowest being in the mp-Si200 NPs.

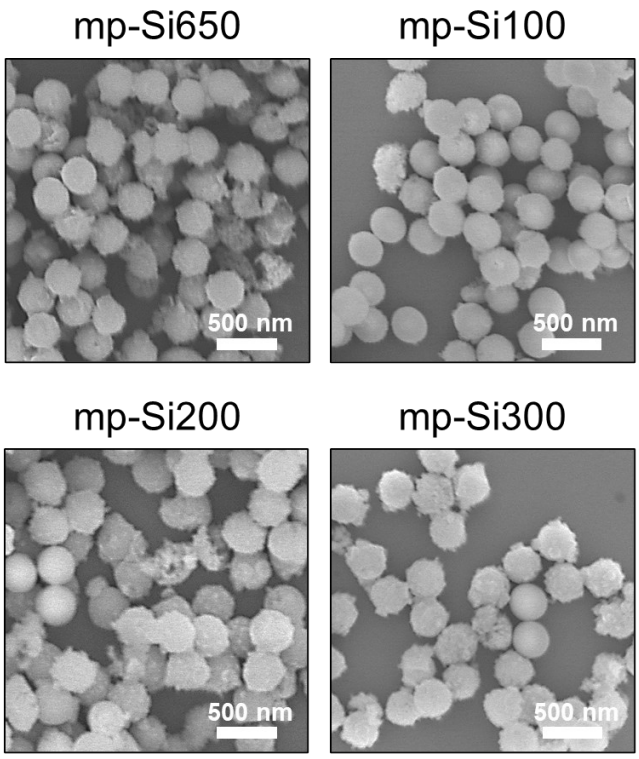

Figure 5. 9. SEM images of mp-Si NPs prepared under different reaction conditions using Mg-L.

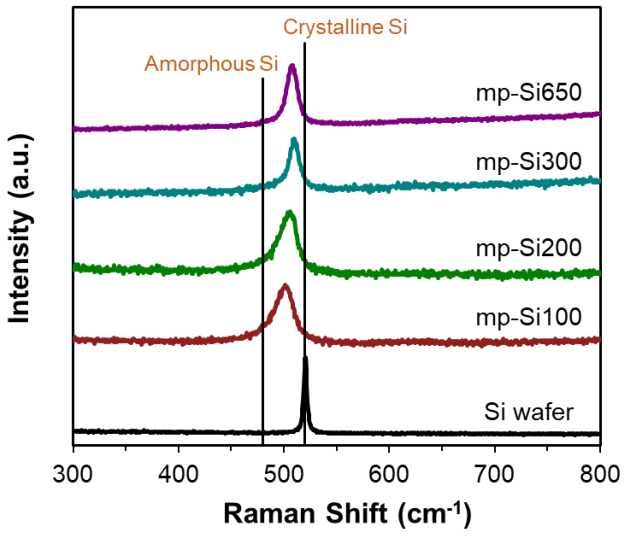

Figure 5. 10. Raman spectra of Si wafer and mp-Si NPs prepared under different annealing conditions using Mg-L as the reagent.

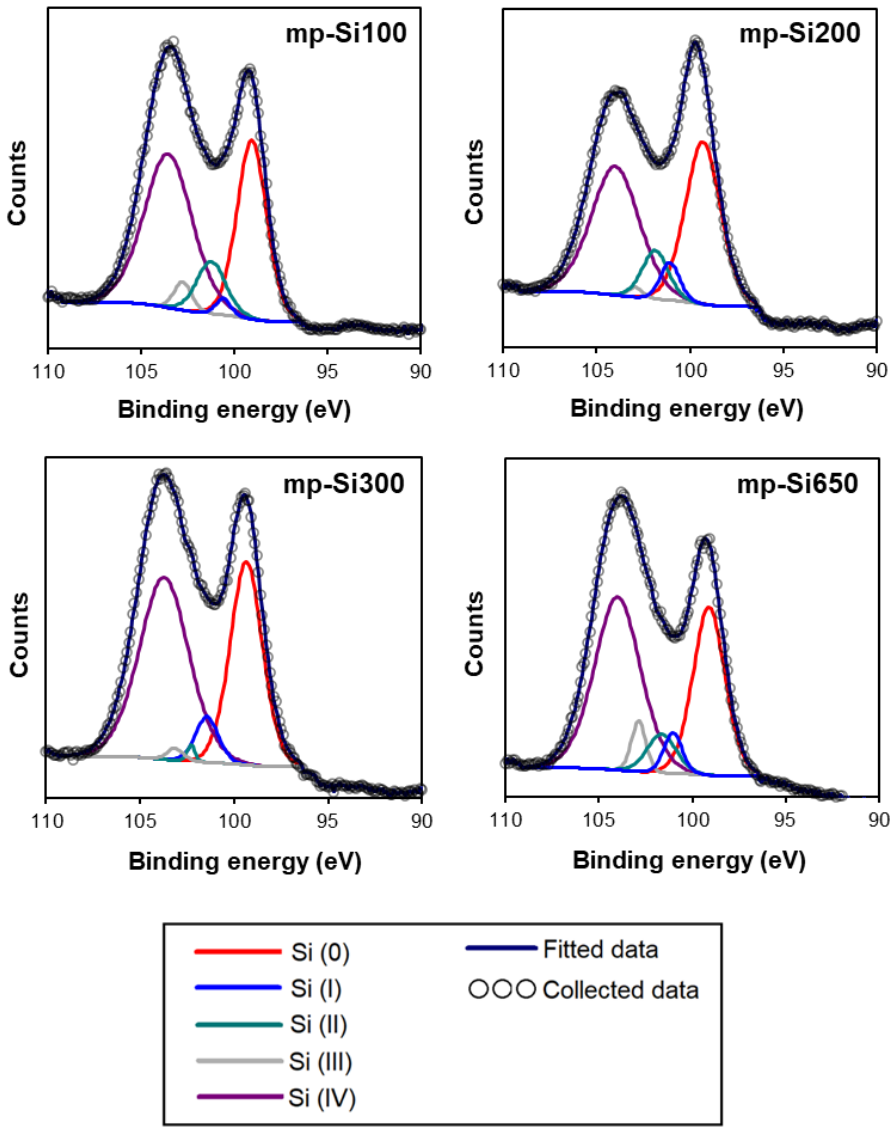

Figure 5. 11. High resolution XP spectra of the Si 2p region of mp-Si NPs prepared under different annealing conditions using Mg-L. For clarity, only $2p_{3/2}$ peaks are shown.

The high amounts of surface oxides that are seen in these samples could be due to a combination of particle fracturing (leading to faster surface oxidation) and incomplete reduction. The larger particle size and broader size distribution of the Mg-L reagent probably leads to a more inhomogeneous reaction mixture compared to when Mg-S is used.

Larger particles slow the rate of magnesiothermic reduction due to lower surface area and higher nucleation barrier, which could result in areas of incomplete reduction. Further, the larger particle sizes can create artificial Mg-poor areas in the reaction leading to unreacted SiO_2 particles and formation of Mg_2Si in Mg-rich regions, which can occur when the Mg:Si ratio is high.[105] The effect of poor homogeneity would also explain the variability seen in the photocatalytic performance between different sample batches (as outlined in Table 5.7). Given that large reagent particles generally reduce the rate of solid-state reactions, it is surprising that the mp-Si200 NPs had a lower oxide amount and better photocatalytic performance than the mp-Si300 NPs. It seems likely that other factors besides the amount of surface oxide (such as the surface area and porosity) contribute to the high performance of the mp-Si200 samples given their drastically improved H_2 evolution rates. One hypothesis is that with higher annealing temperature, heat accumulation in Mg-rich regions of the reaction mixture is high enough to cause morphological damage to the mp-Si, even though the reaction rates at Mg-poor regions may be relatively low. The formation of Mg_2Si could also affect the product morphology since it is removed with MgO during HCl treatment.[98] This could influence the amount of surface oxidation. Further characterization (such as analysis of the surface area and porosity and HRTEM imaging) is required to elucidate these differences and provide a complete explanation for the observed trends.

A third Mg reagent with a –325 mesh size was obtained from Oakwood Chemical (Mg-S2). The average particle size was estimated from SEM (Fig. 5.6C) to be 28 ± 16 μm. The Mg-S2 reagent was used to prepare mp-Si300 by annealing at 650 °C for 0.5 h followed by 300 °C for 6 h. This sample had a relatively low photocatalytic performance with a H_2 evolution rate of 1030 μmol h^{-1} g^{-1} of Si. The XRD pattern (Fig 5.12) revealed

the presence of the by-product Mg_2SiO_4 in this sample, which can form at temperatures above 1100 °C due to excess heat accumulation.[105,106,204] SEM imaging (Fig. 5.13A) also revealed extensive morphological damage and particle fusion. These results suggest that the reaction reaches excessively high temperatures (well above 1000 °C) when using Mg-S2. Therefore, the synthesis was repeated using a lower temperature (100 °C) for the second step to prepare mp-Si100. This dramatically improved the H_2 evolution rate to 4420 μmol h^{-1} g^{-1} of Si. However, Mg_2SiO_4 is still seen in the XRD (Fig. 5.12), and significant morphological damage is observed by SEM (Fig. 5.13B).

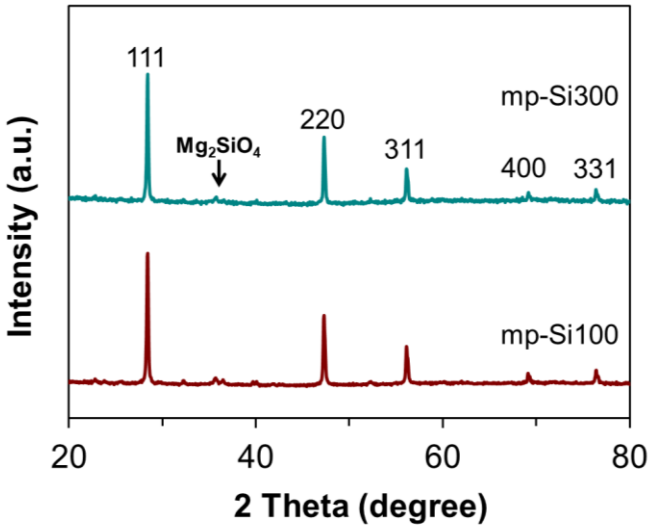

Figure 5. 12. Powder XRD patterns of mp-Si NPs prepared under different magnesiothermic reduction conditions using Mg-S2.

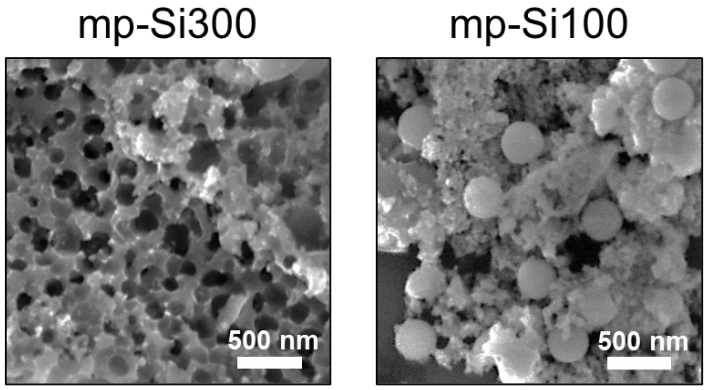

Figure 5. 13. SEM images of mp-Si prepared using Mg-S2.

The results for the photocatalytic performance of mp-Si made from Mg-S2 support the finding that Mg-S2 has a smaller overall particle size distribution compared to Mg-S. Smaller Mg particles have a higher reactivity (due to their high surface area) which can speed up the reaction kinetics of magnesiothermic reduction, leading to a large heat release. This effect has been shown to induce excessive particle sintering in mp-Si in previous work.[105] The use of Mg-S2 resulted in mp-Si NPs containing the by-product Mg_2SiO_4 and large agglomerates of sintered particles, which both can arise from elevated reaction temperatures. Furthermore, these particles had a high degree of crystallinity, indicated by the sharp Si peaks in their XRD spectra (Fig. 5.12), which tends to improve as the reaction temperature increases. The crystallinity of these samples may therefore be a key contributor to their photocatalytic performance, particularly the high performance of the mp-Si100.

It is evident from the preliminary results presented in this section that the choice of Mg reagent has a crucial effect on the optimal magnesiothermic reduction conditions for obtaining high-performing mp-Si photocatalysts. As such, care must be taken to ensure consistency (both in the size and the supplier) of the reagents selected in order to maintain

reproducibility when synthesizing mp-Si. A more thorough investigation into the effects of the Mg characteristics (*i.e.,* average particle size, morphology, purity, and overall size distribution) and further characterization of the resulting mp-Si is necessary to achieve a more complete understanding.

5.4. Conclusions

Four Ni deposition methods (calcination, photodeposition, *in-situ* photodeposition and chemical reduction) were investigated for loading Ni cocatalysts onto the surface of mp-Si NPs. Of these, chemical reduction with $NaBH_4$ gave the most promising results, showing an increase in the H_2 evolution rate when the amount of Ni added was 5 wt. %. These results warrant further investigation into the effect of the Ni loading amount (*via* chemical reduction of $Ni(NO_3)_2$) on the H_2 evolution rates of high-performing mp-Si photocatalysts.

The choice of Mg reagent for magnesiothermic reduction was also found to be an important factor influencing the photocatalytic performance of mp-Si. Using Mg with a different particle size (Mg-L) or from a different supplier (Mg-S2) changed the expected H_2 evolution rates of the mp-Si samples prepared under the previously optimized reaction conditions (650 °C for 0.5 h followed by 300 °C for 6 h). As such, it is important to keep the choice of reagent consistent in order to achieve reproducible mp-Si photocatalysts. High H_2 evolution rates were achieved by using Mg-L (Mg with an average particle size of 71 ± 25 μm) and annealing at 650 °C for 0.5 h, then 200 °C for 6 h.

CHAPTER 6. Conclusions and Future Work

The results presented in this thesis provide insight into how the physical and chemical properties of mp-Si NPs influence their photocatalytic performance for H_2 generation. Specifically, the crystallinity and amount of Si oxides/suboxides were found to play an important role (Fig. 6.1). It is hypothesized that these factors primarily affect the charge carrier diffusion process of photocatalysis. For instance, oxygen impurities introduce defect states which can lead to recombination, while high crystallinity limits the number of defects and facilitates carrier diffusion. Additionally, excess sintering can introduce grain boundaries which may also act as recombination sites.

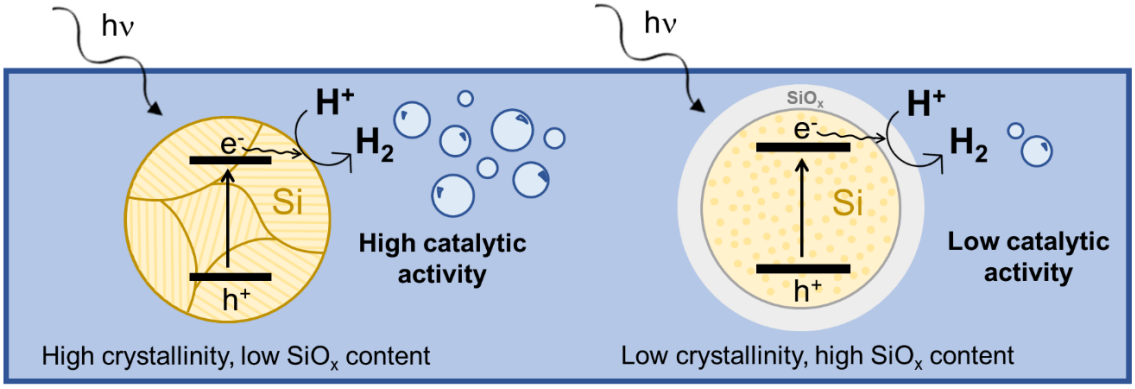

Figure 6. 1. Visual representation showing the effects of crystallinity and oxygen content on photocatalytic H_2 generation by mp-Si NPs. Reproduced from reference 166 by permission of the Royal Society of Chemistry.

Magnesiothermic reduction has become the sought-after method to synthesize mp-Si NPs; however, the number of tunable parameters which can influence their physical properties has led to inconsistencies in the literature between the H_2 evolution rates reported. While the tunability of magnesiothermic reduction reactions could be beneficial

in designing the best performing photocatalysts, the interplay between variables such as the reaction conditions and the chosen reactants (SiO_2 precursor and Mg) adds a complexity to the synthetic method that warrants more complete understanding. In regards to designing high performing mp-Si photocatalysts for H_2 generation, the work in this thesis supports the following general conclusions: 1) to prepare mp-Si by magnesiothermic reduction, a non-porous SiO_2 precursor is preferred, as it yields products with higher crystallinity and lower oxygen content, 2) the reaction conditions (temperature and time) used to synthesize mp-Si by magnesiothermic reduction should be optimized considering the choice of SiO_2 precursor and Mg reagent to achieve high crystallinity, low oxygen amount and to avoid morphological damage, and 3) following their synthesis, mp-Si NPs should be stored under inert atmosphere to prevent further oxidation, which deleteriously affects their catalytic activity. Additionally, it is hypothesized that earth-abundant cocatalysts such as Ni have the potential to enhance the photocatalytic performance of mp-Si. However, further investigation is required to develop an efficient deposition method and to determine the optimal loading amount. The specific effects of the reaction conditions, SiO_2 precursor, Mg reagent and Ni cocatalyst on the catalytic activity of mp-Si are discussed below. Directions for future work on mp-Si NPs applied to H_2 generation are discussed in section 6.4.

6.1. Influence of the Reaction Conditions

The reaction temperature and time used for magnesiothermic reduction was found to influence the crystallinity and amount of oxidation in the resulting mp-Si NPs. The high *in-situ* reaction temperatures that likely occur when the reaction was held at 650 ºC for its duration resulted in sintering and fracturing of the mp-Si NPs, which probably led to faster

oxidation due to the larger exposed surface. The high amount of Si oxide in this sample resulted in lower H_2 evolution rates despite the high degree of crystallinity and large crystallite size. Furthermore, grain boundaries formed from sintering could act as trap states and/or recombination sites.

For the mp-Si NPs prepared by the two-step annealing method, lower temperatures (mp-Si100 and mp-Si200) produced samples with smaller crystallite sizes, a lower degree of crystallinity and higher amount of oxide. The highest H_2 evolution rate (4437 ± 450 μmol h^{-1} g^{-1} of Si) was reported for the mp-Si300 NPs, which had low amounts of oxidation, large crystallites and a high degree of crystallinity. This represents the highest rate for mp-Si NPs reported in the literature thus far.[166]

6.2. Influence of the Reactants

In Chapter 4, porous SiO_2 precursors (SBA-15) were used to investigate the influence of porosity on the photocatalytic activity of mp-Si. While these mp-Si NPs all had a relatively high SSA (> 300 m^2 g^{-1}), small differences in the SSA between samples did not have a noticeable effect on the trend in their H_2 evolution rates. Notably, the SSAs were still lower than those reported for mp-Si prepared from non-porous SiO_2 under the same reaction conditions and were decreased from those of their precursors. This is hypothesized to be a result of collapse of the original SBA-15 pores during the thermal treatment as well as from the formation of elemental Si. H_2 evolution rates observed for the mp-Si NPs were found to increase with decreasing pore size. Larger pores appear to facilitate the oxidation of mp-Si surfaces, which leads to lower catalytic activity.

The Mg particle size used as a reagent for magnesiothermic reduction was also found to influence the optimal reaction conditions needed to prepare high performing mp-Si NPs (discussed in Chapter 5). When larger Mg (< 0.1 mm particles sourced from Sigma Aldrich) was used, samples annealed at 650 °C for 0.5 h, then at 200 °C for 6 h (mp-Si200) had the highest photocatalytic performance. Since larger reagent particles reduce the contact area between the reagents in solid state reactions, local areas of incomplete reduction likely contributed to the high oxygen content observed for these samples. Furthermore, inconsistencies due to the broader size distribution of the Mg particles reduced the reproducibility of the H_2 evolution rates. Conversely, the use of smaller Mg particles (–325 mesh Mg sourced from Oakwood Chemicals) resulted in extensive morphological damage, likely due to fast reaction rates creating high local temperatures. Lowering the temperature of the second annealing step to 100 °C (mp-Si100) dramatically improved the photocatalytic performance. These results demonstrate the importance of consistency when choosing the reactants for magnesiothermic reduction reactions in order to achieve reproducible results.

6.3. Influence of Nickel Cocatalysts

In Chapter 5, preliminary studies were performed in order to screen the plausibility of various Ni deposition methods. Calcination, photodeposition (pre-treatment and *in-situ*), and chemical reduction methods were attempted to deposit Ni cocatalysts onto mp-Si NPs. Of these, chemical reduction gave the most promising results for photocatalytic enhancement, showing a slight increase in the H_2 evolution rate at a Ni loading of 5 wt. %. Photodeposition methods lowered the photocatalytic activity of mp-Si, likely due to oxidation which occurred during the deposition process. Calcination also resulted in a loss

of photocatalytic activity; however, possible reasons for these results are less clear and warrant more a thorough characterization of the materials to discern. For all the methods tested, further studies are required to replicate the findings presented and to determine the optimal Ni loading amount. Plans for future work in this regard are discussed in more detail in section 6.4.3.

6.4. Future Work

6.4.1. Further Understanding of Magnesiothermic Reduction, the Physical Properties of Mesoporous Silicon, and their Effects on Photocatalytic Activity

The results of this thesis demonstrate how the many variables involved in magnesiothermic reduction reactions can influence the properties and thus the photocatalytic performance of mp-Si NPs. Valuable insight was gained regarding the effects of the reaction conditions, the choice of SiO_2 precursor (porous or non-porous) and the particle size of the Mg reagent on the photocatalytic performance of mp-Si. However, future work should aim to develop a more complete understanding of the interplay between these variables and their affect on the physical and chemical properties of mp-Si. Furthermore, the mechanisms through which factors such as the crystallinity and amount of oxygen affect the catalytic activity of mp-Si could be further elucidated.

The reaction conditions required to optimize the photocatalytic performance of mp-Si changed depending on the choice of Mg reagent. With this in mind, it is likely that the nature of the SiO_2 precursor (*i.e.,* the particle size and morphology) would also influence the optimization of reaction conditions. In future studies, experiments conducted in Chapter 3 could be repeated while varying the SiO_2 particle size to investigate the influence of the SiO_2 precursor. Future studies could also look to optimize the reaction conditions for the

SBA-15 precursors used in Chapter 4 to determine whether higher photocatalytic performance could be achieved. The mp-Si NPs in Chapter 4 were synthesized using the best reaction conditions from Chapter 3 for consistency. However, it remains possible that changing the reaction conditions could improve the performance of these mp-Si NPs. Such studies could lead to a better understanding of the mechanisms involved in magnesiothermic reduction and allow us to better predict the combination of precursor, Mg reagent, and reaction conditions that would optimize the performance of mp-Si NPs.

Of all the samples discussed in this work, the highest H_2 evolution rate (6747 μmol h^{-1} g^{-1} of Si) was achieved using the mp-Si200 NPs synthesized with > 0.1 mm Mg sourced from Sigma Aldrich (Table 5.7). Surprisingly, these showed improved performance compared to the mp-Si300 NPs (made with –325 mesh Mg powder from Alfa Aesar) optimized in Chapter 3, despite having a higher oxygen content (Fig. 5.11) and lower crystallinity (Fig. 5.10). The findings suggest that other factors beyond the crystallinity and oxygen amount also play significant roles in the photocatalytic activity. The mp-Si photocatalysts discussed in section 5.3.3 should be further characterized to obtain a more complete understanding of these results. Specifically, an analysis of the surface area and porosity of these samples would be imperative. TEM and HRTEM should also be performed to reveal additional morphological details and determine the crystallite size.

In order to further advance our understanding of photocatalysis using mp-Si, it is necessary to understand the dynamics of photoexcited charge carriers. It is proposed in this thesis that the crystallinity and oxygen content of mp-Si influence the photocatalytic activity through the minimization or introduction of trap states, which limit the charge carrier diffusion lengths. This explanation could be further refined through characterization

of the charge carrier dynamics in the mp-Si NPs. In future work, the average carrier lifetimes in mp-Si samples with varying degrees of crystallinity and oxygen content could be investigated using time-resolved techniques such as transient absorption spectroscopy (TAS).[205]

6.4.2. Surface Protection Strategies

In Chapter 3 (section 3.2.6) it was demonstrated that after synthesis mp-Si NPs continue to oxidize over time, and that this oxidation decreases the photocatalytic performance. The photocatalysts were also found to show poor recyclability (Figs. 3.8C and 4.11) owing to oxidation that occurs during the catalytic reactions. Surface protection strategies such as the incorporation of surface-bound ligands, coatings or polymer encapsulation could be used to improve the oxidative stability of mp-Si NPs. Surface protected Si NPs have been considered for applications as battery anode materials,[206–208] solar cells,[209] LEDs,[210] for photocatalytic degradation of pollutants[45] and to improve the photoluminescent properties of Si quantum dots.[211] However, the effect of surface protection on the photocatalytic activity of mp-Si for H_2 generation has not been investigated. Future work will focus on developing appropriate surface protection strategies to prolong the longevity and recyclability of mp-Si NPs without damaging their photocatalytic performance.

6.4.3. Cocatalysts and Other Enhancement Strategies

Chapter 5 presents the data from initial screening experiments investigating the photocatalytic performance of mp-Si NPs following Ni deposition. Replicate studies are required to confirm these results. Specifically, future work will focus on revisiting the

chemical reduction and calcination methods of Ni deposition. Calcination of mp-Si with $Ni(OAc)_2$ resulted in a decreased H_2 evolution rate for each of the samples tested. However, this may be due to oxidation which occurred during the impregnation (mixing and drying) steps. In future work, performing these steps under inert atmosphere before calcination could potentially give better results. Although the calcination temperature was relatively low (350 °C), there is still a possibility that heat treatment caused morphological damage to the mp-Si NPs which hindered their catalytic activity. Microscopy (SEM and TEM) will be performed to investigate whether morphological damage occurred. For both deposition methods, detailed microscopy analysis is imperative to determine whether Ni was deposited onto the surface of mp-Si, as well as the shape, size and distribution of Ni particles. Microscopy techniques such as back-scattered SEM, TEM and HRTEM could be used to visualize the Ni particles.

Future work could also explore the use of other earth-abundant metals such as cobalt (Co) and copper (Cu) as cocatalysts for mp-Si NPs. Co and Cu cocatalysts have been applied to other materials for photocatalytic H_2 production in previous work.[25] Beyond this, other strategies to enhance the photocatalytic performance of mp-Si such as doping, alloying or plasmonic enhancement could be investigated.

REFERENCES

(1) Bockris, J. O. M. The Hydrogen Economy: Its History. *Int. J. Hydrog. Energy* **2013**, *38*, 2579–2588.

(2) Dou, Y.; Sun, L.; Ren, J.; Dong, L. Opportunities and Future Challenges in Hydrogen Economy for Sustainable Development. In *Hydrogen Economy: Supply Chain, Life Cycle Analysis and Energy Transition for Sustainability;* Academic Press, 2017; pp 277–305.

(3) Rath, R.; Kumar, P.; Mohanty, S.; Nayak, S. K. Recent Advances, Unsolved Deficiencies, and Future Perspectives of Hydrogen Fuel Cells in Transportation and Portable Sectors. *Int. J. Energy Res.* **2019**, *43*, 8931–8955.

(4) Martin, A.; Agnoletti, M.-F.; Brangier, E. Users in the Design of Hydrogen Energy Systems: A Systematic Review. *Int. J. Hydrog. Energy* **2020**, *45*, 11889–11900.

(5) Fonseca, J. D.; Camargo, M.; Commenge, J.-M.; Falk, L.; Gil, I. D. Trends in Design of Distributed Energy Systems Using Hydrogen as Energy Vector: A Systematic Literature Review. *Int. J. Hydrog. Energy* **2019**, *44*, 9486–9504.

(6) Ramachandran, R. An Overview of Industrial Uses of Hydrogen. *Int. J. Hydrog. Energy* **1998**, *23*, 593–598.

(7) Soltani, R.; Rosen, M. A.; Dincer, I. Assessment of CO_2 Capture Options from Various Points in Steam Methane Reforming for Hydrogen Production. *Int. J. Hydrog. Energy* **2014**, *39*, 20266–20275.

(8) Wang, Q.; Domen, K. Particulate Photocatalysts for Light-Driven Water Splitting: Mechanisms, Challenges, and Design Strategies. *Chem. Rev.* **2020**, *120*, 919–985.

(9) Dincer, I.; Zamfirescu, C. Hydrogen and Its Production. In *Sustainable Hydrogen Production*; Elsevier, 2016; pp 65–97.

(10) Hisatomi, T.; Kubota, J.; Domen, K. Recent Advances in Semiconductors for Photocatalytic and Photoelectrochemical Water Splitting. *Chem. Soc. Rev.* **2014**, *43*, 7520–7535.

(11) Joy, J.; Mathew, J.; George, S. C. Nanomaterials for Photoelectrochemical Water Splitting – Review. *Int. J. Hydrog. Energy* **2018**, *43*, 4804–4817.

(12) Roger, I.; Shipman, M. A.; Symes, M. D. Earth-Abundant Catalysts for Electrochemical and Photoelectrochemical Water Splitting. *Nat. Rev. Chem.* **2017**, *1*, 0003.

(13) Mersch, D.; Lee, C.-Y.; Zhang, J. Z.; Brinkert, K.; Fontecilla-Camps, J. C.; Rutherford, A. W.; Reisner, E. Wiring of Photosystem II to Hydrogenase for Photoelectrochemical Water Splitting. *J. Am. Chem. Soc.* **2015**, *137*, 8541–8549.

(14) Ghirardi, M. L.; Dubini, A.; Yu, J.; Maness, P.-C. Photobiological Hydrogen-Producing Systems. *Chem. Soc. Rev.* **2009**, *38*, 52–61.

(15) Rao, C. N. R.; Dey, S. Solar Thermochemical Splitting of Water to Generate Hydrogen. *Proc. Natl. Acad. Sci. U.S.A.* **2017**, *114* (51), 13385–13393.

(16) Muhich, C. L.; Ehrhart, B. D.; Al-Shankiti, I.; Ward, B. J.; Musgrave, C. B.; Weimer, A. W. A Review and Perspective of Efficient Hydrogen Generation via Solar Thermal Water Splitting: A Review and Perspective of Efficient Hydrogen Generation. *WIREs Energy Environ.* **2016**, *5*, 261–287.

(17) Lange, M.; Roeb, M.; Sattler, C.; Pitz-Paal, R. Efficiency Assessment of a Two-Step Thermochemical Water-Splitting Process Based on a Dynamic Process Model. *Int. J. Hydrog. Energy* **2015**, *40*, 12108–12119.

(18) Li, X.; Hao, X.; Abudula, A.; Guan, G. Nanostructured Catalysts for Electrochemical Water Splitting: Current State and Prospects. *J. Mater. Chem. A* **2016**, *4*, 11973–12000.

(19) Homaei, A. A.; Sariri, R.; Vianello, F.; Stevanato, R. Enzyme Immobilization: An Update. *J. Chem. Biol.* **2013**, *6* (4), 185–205.

(20) Takata, T.; Domen, K. Particulate Photocatalysts for Water Splitting: Recent Advances and Future Prospects. *ACS Energy Lett.* **2019**, *4*, 542–549.

(21) Fujishima, A.; Honda, K. Electrochemical Photolysis of Water at a Semiconductor Electrode. *Nature* **1972**, *238*, 37–38.

(22) Schrauzer, G. N.; Guth, T. D. Photolysis of Water and Photoreduction of Nitrogen on Titanium Dioxide. *J. Am. Chem. Soc.* **1977**, *99*, 7189–7193.

(23) Pinaud, B. A.; Benck, J. D.; Seitz, L. C.; Forman, A. J.; Chen, Z.; Deutsch, T. G.; James, B. D.; Baum, K. N.; Baum, G. N.; Ardo, S.; Wang, H.; Miller, E.; Jaramillo, T. F. Technical and Economic Feasibility of Centralized Facilities for Solar Hydrogen Production via Photocatalysis and Photoelectrochemistry. *Energy Environ. Sci.* **2013**, *6*, 1983.

(24) Shaner, M. R.; Atwater, H. A.; Lewis, N. S.; McFarland, E. W. A Comparative Technoeconomic Analysis of Renewable Hydrogen Production Using Solar Energy. *Energy Environ. Sci.* **2016**, *9*, 2354–2371.

(25) Ran, J.; Zhang, J.; Yu, J.; Jaroniec, M.; Qiao, S. Z. Earth-Abundant Cocatalysts for Semiconductor-Based Photocatalytic Water Splitting. *Chem. Soc. Rev.* **2014**, *43*, 7787–7812.

(26) Maeda, K. Z-Scheme Water Splitting Using Two Different Semiconductor Photocatalysts. *ACS Catal.* **2013**, *3*, 1486–1503.

(27) Li, R.; Weng, Y.; Zhou, X.; Wang, X.; Mi, Y.; Chong, R.; Han, H.; Li, C. Achieving Overall Water Splitting Using Titanium Dioxide-Based Photocatalysts of Different Phases. *Energy Environ. Sci.* **2015**, *8*, 2377–2382.

(28) Hara, M.; Kondo, T.; Komoda, M.; Ikeda, S.; Kondo, J. N.; Domen, K.; Hara, M.; Shinohara, K.; Tanaka, A. Cu_2O as a Photocatalyst for Overall Water Splitting under Visible Light Irradiation. *Chem. Commun.* **1998**, *3*, 357–358.

(29) Sayama, K.; Arakawa, H. Photocatalytic Decomposition of Water and Photocatalytic Reduction of Carbon Dioxide over Zirconia Catalyst. *J. Phys. Chem.* **1993**, *97*, 531–533.

(30) Reddy, V. R.; Hwang, D. W.; Lee, J. S. Photocatalytic Water Splitting over ZrO_2 Prepared by Precipitation Method. *Korean J. Chem. Eng.* **2003**, *20*, 1026–1029.

(31) Noda, Y.; Lee, B.; Domen, K.; Kondo, J. N. Synthesis of Crystallized Mesoporous Tantalum Oxide and Its Photocatalytic Activity for Overall Water Splitting under Ultraviolet Light Irradiation. *Chem. Mater.* **2008**, *20*, 5361–5367.

(32) Yanagida, T.; Sakata, Y.; Imamura, H. Photocatalytic Decomposition of H_2O into H_2 and O_2 over Ga_2O_3 Loaded with NiO. *Chem. Lett.* **2004**, *33*, 726–727.

(33) Sakata, Y.; Matsuda, Y.; Yanagida, T.; Hirata, K.; Imamura, H.; Teramura, K. Effect of Metal Ion Addition in a Ni Supported Ga_2O_3 Photocatalyst on the Photocatalytic Overall Splitting of H_2O. *Catal. Lett.* **2008**, *125*, 22–26.

(34) Domen, K.; Naito, S.; Soma, M.; Onishi, T.; Tamaru, K. Photocatalytic Decomposition of Water Vapour on an NiO–$SrTiO_3$ Catalyst. *J. Chem. Soc., Chem. Commun.* **1980**, *12*, 543–544.

(35) Fujiwara, T.; Sasahara, A.; Happo, N.; Kimura, K.; Hayashi, K.; Onishi, H. Single-Crystal Model of Highly Efficient Water-Splitting Photocatalysts: A $KTaO_3$ Wafer Doped with Calcium Cations. *Chem. Mater.* **2020**, *32*, 1439–1447.

(36) Fang, S.; Hu, Y. H. Recent Progress in Photocatalysts for Overall Water Splitting. *Int. J. Energy Res.* **2019**, *43*, 1082–1098.

(37) Nguyen, P. D.; Duong, T. M.; Tran, P. D. Current Progress and Challenges in Engineering Viable Artificial Leaf for Solar Water Splitting. *J. Sci.: Adv. Mater. Devices* **2017**, *2*, 399–417.

(38) Li, R.; Li, C. Photocatalytic Water Splitting on Semiconductor-Based Photocatalysts. In *Advances in Catalysis*; Elsevier, 2017; Vol. 60, pp 1–57.

(39) Mishra, A.; Mehta, A.; Basu, S.; Shetti, N. P.; Reddy, K. R.; Aminabhavi, T. M. Graphitic Carbon Nitride (g-C_3N_4)-Based Metal-Free Photocatalysts for Water Splitting: A Review. *Carbon* **2019**, *149*, 693–721.

(40) Cao, S.; Yu, J. G-C_3N_4-Based Photocatalysts for Hydrogen Generation. *J. Phys. Chem. Lett.* **2014**, *5*, 2101–2107.

(41) Liu, H.; She, G.; Mu, L.; Shi, W. Porous SiC Nanowire Arrays as Stable Photocatalyst for Water Splitting under UV Irradiation. *Mater. Res. Bull.* **2012**, *47*, 917–920.

(42) Hao, J.-Y.; Wang, Y.-Y.; Tong, X.-L.; Jin, G.-Q.; Guo, X.-Y. Photocatalytic Hydrogen Production over Modified SiC Nanowires under Visible Light Irradiation. *Int. J. Hydrog. Energy* **2012**, *37*, 15038–15044.

(43) Kudo, A.; Miseki, Y. Heterogeneous Photocatalyst Materials for Water Splitting. *Chem. Soc. Rev.* **2009**, *38*, 253–278.

(44) Bains, W.; Seager, S. A Combinatorial Approach to Biochemical Space: Description and Application to the Redox Distribution of Metabolism. *Astrobiology* **2012**, *12*, 271–281.

(45) Iqbal, M.; Purkait, T. K.; Goss, G. G.; Bolton, J. R.; Gamal El-Din, M.; Veinot, J. G. C. Application of Engineered Si Nanoparticles in Light-Induced Advanced Oxidation Remediation of a Water-Borne Model Contaminant. *ACS Nano* **2016**, *10*, 5405–5412.

(46) Schneider, J.; Bahnemann, D. W. Undesired Role of Sacrificial Reagents in Photocatalysis. *J. Phys. Chem. Lett.* **2013**, *4*, 3479–3483.

(47) Ahmad, H.; Kamarudin, S. K.; Minggu, L. J.; Kassim, M. Hydrogen from Photo-Catalytic Water Splitting Process: A Review. *Renew. Sust. Energ. Rev.* **2015**, *43*, 599–610.

(48) Kahng, S.; Yoo, H.; Kim, J. H. Recent Advances in Earth-Abundant Photocatalyst Materials for Solar H_2 Production. *Adv. Powder Technol.* **2020**, *31*, 11–28.

(49) Liu, S.; Zhang, C.; Sun, Y.; Chen, Q.; He, L.; Zhang, K.; Zhang, J.; Liu, B.; Chen, L.-F. Design of Metal-Organic Framework-Based Photocatalysts for Hydrogen Generation. *Coord. Chem. Rev.* **2020**, *413*, 213266.

(50) Halpin, Y.; Pryce, M. T.; Rau, S.; Dini, D.; Vos, J. G. Recent Progress in the Development of Bimetallic Photocatalysts for Hydrogen Generation. *Dalton Trans.* **2013**, *42*, 16243.

(51) Teo, S. H.; Islam, A.; Taufiq-Yap, Y. H.; Awual, Md. R. Introducing the Novel Composite Photocatalysts to Boost the Performance of Hydrogen (H_2) Production. *J. Clean. Prod.* **2021**, *313*, 127909.

(52) Zhu, J.; Zäch, M. Nanostructured Materials for Photocatalytic Hydrogen Production. *Curr. Opin. Colloid Interface Sci.* **2009**, *14*, 260–269.

(53) Sreethawong, T.; Suzuki, Y.; Yoshikawa, S. Photocatalytic Evolution of Hydrogen over Nanocrystalline Mesoporous Titania Prepared by Surfactant-Assisted Templating Sol–Gel Process. *Catal. Commun.* **2005**, *6*, 119–124.

(54) Sui, Y.; Liu, S.; Li, T.; Liu, Q.; Jiang, T.; Guo, Y.; Luo, J.-L. Atomically Dispersed Pt on Specific TiO_2 Facets for Photocatalytic H2 Evolution. *J. Catal.* **2017**, *353*, 250–255.

(55) Lalitha, K.; Reddy, J. K.; Phanikrishna Sharma, M. V.; Kumari, V. D.; Subrahmanyam, M. Continuous Hydrogen Production Activity over Finely Dispersed Ag_2O/TiO_2 Catalysts from Methanol:Water Mixtures under Solar Irradiation: A Structure-Activity Correlation. *Int. J. Hydrog. Energy* **2010**, *35*, 3991–4001.

(56) Wang, Y.; Wang, Y.; Xu, R. Photochemical Deposition of Pt on CdS for H_2 Evolution from Water: Markedly Enhanced Activity by Controlling Pt Reduction Environment. *J. Phys. Chem. C* **2013**, *117*, 783–790.

(57) Yang, Y.; Zhang, Y.; Fang, Z.; Zhang, L.; Zheng, Z.; Wang, Z.; Feng, W.; Weng, S.; Zhang, S.; Liu, P. Simultaneous Realization of Enhanced Photoactivity and Promoted Photostability by Multilayered MoS_2 Coating on CdS Nanowire Structure via Compact Coating Methodology. *ACS Appl. Mater. Interfaces* **2017**, *9*, 6950–6958.

(58) Zong, X.; Yan, H.; Wu, G.; Ma, G.; Wen, F.; Wang, L.; Li, C. Enhancement of Photocatalytic H_2 Evolution on CdS by Loading MoS_2 as Cocatalyst under Visible Light Irradiation. *J. Am. Chem. Soc.* **2008**, *130*, 7176–7177.

(59) Chang, K.; Mei, Z.; Wang, T.; Kang, Q.; Ouyang, S.; Ye, J. MoS_2/Graphene Cocatalyst for Efficient Photocatalytic H_2 Evolution under Visible Light Irradiation. *ACS Nano* **2014**, *8*, 7078–7087.

(60) Martin, D. J.; Qiu, K.; Shevlin, S. A.; Handoko, A. D.; Chen, X.; Guo, Z.; Tang, J. Highly Efficient Photocatalytic H_2 Evolution from Water Using Visible Light and Structure-Controlled Graphitic Carbon Nitride. *Angew. Chem. Int. Ed.* **2014**, *53*, 9240–9245.

(61) Tan, Y.; Shu, Z.; Zhou, J.; Li, T.; Wang, W.; Zhao, Z. One-Step Synthesis of Nanostructured g-C_3N_4/TiO_2 Composite for Highly Enhanced Visible-Light Photocatalytic H_2 Evolution. *Appl. Catal. B.* **2018**, *230*, 260–268.

(62) Yang, S.; Gong, Y.; Zhang, J.; Zhan, L.; Ma, L.; Fang, Z.; Vajtai, R.; Wang, X.; Ajayan, P. M. Exfoliated Graphitic Carbon Nitride Nanosheets as Efficient Catalysts for Hydrogen Evolution Under Visible Light. *Adv. Mater.* **2013**, *25*, 2452–2456.

(63) Niu, P.; Zhang, L.; Liu, G.; Cheng, H.-M. Graphene-Like Carbon Nitride Nanosheets for Improved Photocatalytic Activities. *Adv. Funct. Mater.* **2012**, *22*, 4763–4770.

(64) Wang, X.; Maeda, K.; Chen, X.; Takanabe, K.; Domen, K.; Hou, Y.; Fu, X.; Antonietti, M. Polymer Semiconductors for Artificial Photosynthesis: Hydrogen Evolution by Mesoporous Graphitic Carbon Nitride with Visible Light. *J. Am. Chem. Soc.* **2009**, *131*, 1680–1681.

(65) Li, X.-H.; Zhang, J.; Chen, X.; Fischer, A.; Thomas, A.; Antonietti, M.; Wang, X. Condensed Graphitic Carbon Nitride Nanorods by Nanoconfinement: Promotion of Crystallinity on Photocatalytic Conversion. *Chem. Mater.* **2011**, *23*, 4344–4348.

(66) Yuan, Y.-P.; Yin, L.-S.; Cao, S.-W.; Gu, L.-N.; Xu, G.-S.; Du, P.; Chai, H.; Liao, Y.-S.; Xue, C. Microwave-Assisted Heating Synthesis: A General and Rapid Strategy for Large-Scale Production of Highly Crystalline g-C_3N_4 with Enhanced Photocatalytic H_2 Production. *Green Chem.* **2014**, *16*, 4663–4668.

(67) Wang, B.; Zhang, J.; Huang, F. Enhanced Visible Light Photocatalytic H_2 Evolution of Metal-Free g-C_3N_4/SiC Heterostructured Photocatalysts. *Appl. Surf. Sci.* **2017**, *391*, 449–456.

(68) Jitputti, J.; Suzuki, Y.; Yoshikawa, S. Synthesis of TiO_2 Nanowires and Their Photocatalytic Activity for Hydrogen Evolution. *Catal. Commun.* **2008**, *9*, 1265–1271.

(69) Lv, P.; Xu, C.; Peng, B. Design of a Silicon Photocatalyst for High-Efficiency Photocatalytic Water Splitting. *ACS Omega* **2020**, *5*, 6358–6365.

(70) Jang, Y. J.; Ryu, J.; Hong, D.; Park, S.; Lee, J. S. A Multi-Stacked Hyperporous Silicon Flake for Highly Active Solar Hydrogen Production. *Chem. Commun.* **2016**, *52*, 10221–10224.

(71) Ma, W.; Li, J.; Sun, H.; Chen, J.; Wang, D.; Mao, Z. Robust Hydrogen Generation over Layered Crystalline Silicon Materials via Integrated H_2 Evolution Routes. *Int. J. Hydrog. Energy* **2020**, *45*, 19007–19016.

(72) Sun, H.; Chen, J.; Liu, S.; Agrawal, D. K.; Zhao, Y.; Wang, D.; Mao, Z. Photocatalytic H_2 Evolution of Porous Silicon Derived from Magnesiothermic Reduction of Mesoporous SiO_2. *Int. J. Hydrog. Energy* **2019**, *44*, 7216–7221.

(73) Dai, F.; Zai, J.; Yi, R.; Gordin, M. L.; Sohn, H.; Chen, S.; Wang, D. Bottom-up Synthesis of High Surface Area Mesoporous Crystalline Silicon and Evaluation of Its Hydrogen Evolution Performance. *Nat. Commun.* **2014**, *5*, 1–11.

(74) Song, H.; Liu, D.; Yang, J.; Wang, L.; Xu, H.; Xiong, Y. Highly Crystalline Mesoporous Silicon Spheres for Efficient Visible Photocatalytic Hydrogen Evolution. *ChemNanoMat* **2017**, *3*, 22–26.

(75) Ryu, J.; Jang, Y. J.; Choi, S.; Kang, H. J.; Park, H.; Lee, J. S.; Park, S. All-in-One Synthesis of Mesoporous Silicon Nanosheets from Natural Clay and Their Applicability to Hydrogen Evolution. *NPG Asia Mater.* **2016**, *8*, e248.

(76) Martell, S. A.; Werner-Zwanziger, U.; Dasog, M. The Influence of Hydrofluoric Acid Etching Processes on the Photocatalytic Hydrogen Evolution Reaction Using Mesoporous Silicon Nanoparticles. *Faraday discuss.* **2020**, *222*, 176–189.

(77) Hwang, S. W.; Park, G.; Edwards, C.; Corbin, E. A.; Kang, S. K.; Cheng, H.; Song, J. K.; Kim, J. H.; Yu, S.; Ng, J.; Lee, J. E.; Kim, J.; Yee, C.; Bhaduri, B.; Omennetto, F. G.; Huang, Y.; Bashir, R.; Goddard, L.; Popescu, G.; Lee, K. M.; Rogers, J. A. Dissolution Chemistry and Biocompatibility of Single-Crystalline Silicon Nanomembranes and Associated Materials for Transient Electronics. *ACS Nano* **2014**, *8*, 5843–5851.

(78) Battaglia, C.; Cuevas, A.; De Wolf, S. High-Efficiency Crystalline Silicon Solar Cells: Status and Perspectives. *Energy Environ. Sci.* **2016**, *9*, 1552–1576.

(79) Huang, Q.; Ye, Z.; Xiao, X. Recent Progress in Photocathodes for Hydrogen Evolution. *J. Mater. Chem. A* **2015**, *3*, 15824–15837.

(80) Fan, R.; Mi, Z.; Shen, M. Silicon Based Photoelectrodes for Photoelectrochemical Water Splitting. *Opt. Express* **2019**, *27*, A51.

(81) Valiullin, R. Mesoporous Silicon. In *Handbook of Porous Silicon*; Canham, L., Ed.; Springer International Publishing: Cham, 2017; pp 1–15.

(82) Ocier, C. R.; Krueger, N. A.; Zhou, W.; Braun, P. V. Tunable Visibly Transparent Optics Derived from Porous Silicon. *ACS Photonics* **2017**, *4* (4), 909–914.

(83) Levitsky, I. Porous Silicon Structures as Optical Gas Sensors. *Sensors* **2015**, *15*, 19968–19991.

(84) McInnes, S. J. P.; Szili, E. J.; Al-Bataineh, S. A.; Vasani, R. B.; Xu, J.; Alf, M. E.; Gleason, K. K.; Short, R. D.; Voelcker, N. H. Fabrication and Characterization of a Porous Silicon Drug Delivery System with an Initiated Chemical Vapor Deposition Temperature-Responsive Coating. *Langmuir* **2016**, *32*, 301–308.

(85) Lai, Y.; Thompson, J. R.; Dasog, M. Metallothermic Reduction of Silica Nanoparticles to Porous Silicon for Drug Delivery Using New and Existing Reductants. *Chem. Eur. J.* **2018**, *24*, 7913–7920.

(86) Manilov, A. I.; Skryshevsky, V. A. Hydrogen in Porous Silicon – A Review. *Mater. Sci. Eng. B* **2013**, *178*, 942–955.

(87) Entwistle, J. E.; Beaucage, G.; Patwardhan, S. V. Mechanistic Understanding of Pore Evolution Enables High Performance Mesoporous Silicon Production for Lithium-Ion Batteries. *J. Mater. Chem. A* **2020**, *8*, 4938–4949.

(88) Dasog, M.; Kraus, S.; Sinelnikov, R.; Veinot, J. G. C.; Rieger, B. CO_2 to Methanol Conversion Using Hydride Terminated Porous Silicon Nanoparticles. *Chem. Commun.* **2017**, *53*, 3114–3117.

(89) Martell, S. A.; Lai, Y.; Traver, E.; MacInnis, J.; Richards, D. D.; MacQuarrie, S.; Dasog, M. High Surface Area Mesoporous Silicon Nanoparticles Prepared via Two-Step Magnesiothermic Reduction for Stoichiometric CO_2 to CH_3OH Conversion. *ACS Appl. Nano Mater.* **2019**.

(90) Song, H.; Liu, D.; Yang, J.; Wang, L.; Xu, H.; Xiong, Y. Highly Crystalline Mesoporous Silicon Spheres for Efficient Visible Photocatalytic Hydrogen Evolution. *ChemNanoMat* **2017**, *3*, 22–26.

(91) Martell, S. A.; Werner-Zwanziger, U.; Dasog, M. The Influence of Hydrofluoric Acid Etching Process on the Photocatalytic Hydrogen Evolution Reaction Using Mesoporous Silicon Nanoparticles. *Faraday Discuss.* **2019**.

(92) Sun, H.; Chen, J.; Liu, S.; Agrawal, D. K.; Zhao, Y.; Wang, D.; Mao, Z. Photocatalytic H2 Evolution of Porous Silicon Derived from Magnesiothermic Reduction of Mesoporous SiO_2. *Int. J. Hydrog. Energy* **2019**, *44*, 7216–7221.

(93) Dai, F.; Zai, J.; Yi, R.; Gordin, M. L.; Sohn, H.; Chen, S.; Wang, D. Bottom-up Synthesis of High Surface Area Mesoporous Crystalline Silicon and Evaluation of Its Hydrogen Evolution Performance. *Nat. Commun.* **2014**, *5*.

(94) Santos, A.; Kumeria, T. Electrochemical Etching Methods for Producing Porous Silicon. In *Electrochemically Engineered Nanoporous Materials*; Losic, D., Santos, A., Eds.; Springer International Publishing: Cham, 2015; Vol. 220, pp 1–36.

(95) Nissinen, T.; Ikonen, T.; Lama, M.; Riikonen, J.; Lehto, V.-P. Improved Production Efficiency of Mesoporous Silicon Nanoparticles by Pulsed Electrochemical Etching. *Powder Technol.* **2016**, *288*, 360–365.

(96) Kolasinski, K. W. Porous Silicon Formation by Stain Etching. In *Handbook of Porous Silicon*; Canham, L., Ed.; Springer International Publishing: Cham, 2017; pp 1–21.

(97) Nagamori, M.; Malinsky, I.; Claveau, A. Thermodynamics of the Si-C-O System for the Production of Silicon Carbide and Metallic Silicon. *Metall. Trans. B* **1986**, *17*, 503–514.

(98) Entwistle, J.; Rennie, A.; Patwardhan, S. A Review of Magnesiothermic Reduction of Silica to Porous Silicon for Lithium-Ion Battery Applications and Beyond. *J. Mater. Chem. A* **2018**, *6*, 18344–18356.

(99) Palmero, P. Synthesis of Ceramic Powders by Wet Chemical Routes. In *Encyclopedia of Materials: Technical Ceramics and Glasses*; Elsevier, 2021; pp 27–39.

(100) Brinker, C. J.; Scherer, G. W. *Sol-Gel Science: The Physics and Chemistry of Sol-Gel Processing*; Academic Press: Boston, 1990.

(101) Stöber, W.; Fink, A.; Bohn, E. Controlled Growth of Monodisperse Silica Spheres in the Micron Size Range. *J. Colloid Interface Sci.* **1968**, *26*, 62–69.

(102) Han, Y.; Lu, Z.; Teng, Z.; Liang, J.; Guo, Z.; Wang, D.; Han, M.-Y.; Yang, W. Unraveling the Growth Mechanism of Silica Particles in the Stöber Method: In Situ Seeded Growth Model. *Langmuir* **2017**, *33*, 5879–5890.

(103) Bourebrab, M. A.; Oben, D. T.; Durand, G. G.; Taylor, P. G.; Bruce, J. I.; Bassindale, A. R.; Taylor, A. Influence of the Initial Chemical Conditions on the Rational Design of Silica Particles. *J. Sol-Gel Sci. Technol.* **2018**, *88*, 430–441.

(104) Fernandes, R. S.; Raimundo, I. M.; Pimentel, M. F. Revising the Synthesis of Stöber Silica Nanoparticles: A Multivariate Assessment Study on the Effects of Reaction Parameters on the Particle Size. *Colloids Surf. A Physicochem. Eng. Asp.* **2019**, *577*, 1–7.

(105) Yang, Z.; Du, Y.; Hou, G.; Ouyang, Y.; Ding, F.; Yuan, F. Nanoporous Silicon Spheres Preparation via a Controllable Magnesiothermic Reduction as Anode for Li-Ion Batteries. *Electrochim. Acta* **2020**, *329*, 135141.

(106) Shi, L.; Wang, W.; Wang, A.; Yuan, K.; Yang, Y. Understanding the Impact Mechanism of the Thermal Effect on the Porous Silicon Anode Material Preparation via Magnesiothermic Reduction. *J. Alloys Compd.* **2016**, *661*, 27–37.

(107) Kirshenbaum, M. J.; Boebinger, M. G.; Katz, M. J.; McDowell, M. T.; Dasog, M. Solid-State Route for the Synthesis of Scalable, Luminescent Silicon and Germanium Nanocrystals. *ChemNanoMat* **2018**, *4*, 423–429.

(108) Khanna, L.; Lai, Y.; Dasog, M. Systematic Evaluation of Inorganic Salts as a Heat Sink for the Magnesiothermic Reduction of Silica. *Can. J. Chem.* **2018**, *96*, 965–968.

(109) Luo, W.; Wang, X.; Meyers, C.; Wannenmacher, N.; Sirisaksoontorn, W.; Lerner, M. M.; Ji, X. Efficient Fabrication of Nanoporous Si and Si/Ge Enabled by a Heat Scavenger in Magnesiothermic Reactions. *Sci. Rep.* **2013**, *3*.

(110) Stein, A.; Keller, S. W.; Mallouk, T. E. Turning Down the Heat: Design and Mechanism in Solid-State Synthesis. *Science* **1993**, *259*, 1558–1564.

(111) Ryu, J.; Hong, D.; Choi, S.; Park, S. Synthesis of Ultrathin Si Nanosheets from Natural Clays for Lithium-Ion Battery Anodes. *ACS Nano* **2016**, *10*, 2843–2851.

(112) Kaliva, M.; Vamvakaki, M. Nanomaterials Characterization. In *Polymer Science and Nanotechnology*; Elsevier, 2020; pp 401–433.

(113) Bardia, M. M. F.; Ollé, X. A. *X-Ray Single Crystal and Powder Diffraction: Possibilities and Applications;* CCiTUB, 2012.

(114) Inkson, B. J. Scanning Electron Microscopy (SEM) and Transmission Electron Microscopy (TEM) for Materials Characterization. In *Materials Characterization Using Nondestructive Evaluation (NDE) Methods*; Elsevier, 2016; pp 17–43.

(115) Akhtar, K.; Khan, S. A.; Khan, S. B.; Asiri, A. M. Scanning Electron Microscopy: Principle and Applications in Nanomaterials Characterization. In *Handbook of Materials Characterization*; Sharma, S. K., Ed.; Springer International Publishing: Cham, 2018; pp 113–145.

(116) Vernon-Parry, K. D. Scanning Electron Microscopy: An Introduction. *III-Vs Review* **2000**, *13*, 40–44.

(117) Pendse, D. R.; Chin, A. K. Cathodoluminescence and Transmission Cathodoluminescence. In *Encyclopedia of Materials: Science and Technology*; Elsevier, 2001; pp 1–7.

(118) Devine, T. M.; Adar, F. Raman Spectroscopy of Solids. In *Characterization of Materials*; Kaufmann, E. N., Ed.; John Wiley & Sons, Inc.: Hoboken, NJ, USA, 2012.

(119) Tuschel, D. Why Are the Raman Spectra of Crystalline and Amorphous Solids Different? *Spectroscopy* **2017**, *32*, 26–33.

(120) Droz, C.; Vallat-Sauvain, E.; Bailat, J.; Feitknecht, L.; Meier, J.; Shah, A. Relationship between Raman Crystallinity and Open-Circuit Voltage in Microcrystalline Silicon Solar Cells. *Sol. Energy Mater. Sol. Cells* **2004**, *81*, 61–71.

(121) Ivanda, M. Raman Spectroscopy of Porous Silicon. In *Handbook of Porous Silicon*; Canham, L., Ed.; Springer International Publishing: Cham, 2018; pp 611–620.

(122) Stevie, F. A.; Donley, C. L. Introduction to X-Ray Photoelectron Spectroscopy. *J. Vac. Sci. Technol. A* **2020**, *38*, 063204.

(123) Stevie, F. A.; Garcia, R.; Shallenberger, J.; Newman, J. G.; Donley, C. L. Sample Handling, Preparation and Mounting for XPS and Other Surface Analytical Techniques. *J. Vac. Sci. Technol. A* **2020**, *38*, 063202.

(124) Greczynski, G.; Hultman, L. X-Ray Photoelectron Spectroscopy: Towards Reliable Binding Energy Referencing. *Prog. Mater. Sci.* **2020**, *107*, 100591.

(125) Nefedov, V. I. Photoelectron Elastic Scattering Effects in XPS. *J. Electron Spectros. Relat. Phenomena* **1999**, *100*, 1–15.

(126) Skoog, D. A.; West, D. M.; Holler, J. F.; Crouch, S. R. *Fundamentals of Analytical Chemistry*, 9th ed.; Brooks/Cole: Belmont, CA, 2014.

(127) Zanatta, A. R. Revisiting the Optical Bandgap of Semiconductors and the Proposal of a Unified Methodology to Its Determination. *Sci. Rep.* **2019**, *9*, 11225.

(128) Wood, D. L.; Tauc, J. Weak Absorption Tails in Amorphous Semiconductors. *Phys. Rev. B* **1972**, *5*, 3144–3151.

(129) Davis, E. A.; Mott, N. F. Conduction in Non-Crystalline Systems V. Conductivity, Optical Absorption and Photoconductivity in Amorphous Semiconductors. *Philos. Mag. Lett.* **1970**, *22*, 0903–0922.

(130) Makuła, P.; Pacia, M.; Macyk, W. How To Correctly Determine the Band Gap Energy of Modified Semiconductor Photocatalysts Based on UV–Vis Spectra. *J. Phys. Chem. Lett.* **2018**, *9*, 6814–6817.

(131) Atkins, P. W.; De Paula, J. *Physical Chemistry: Thermodynamics, Structure, and Change*, Tenth edition.; W.H. Freeman: New York, 2014.

(132) Swenson, H.; Stadie, N. P. Langmuir's Theory of Adsorption: A Centennial Review. *Langmuir* **2019**, *35*, 5409–5426.

(133) Gómez-Serrano, V.; González-García, C. M.; González-Martín, M. L. Nitrogen Adsorption Isotherms on Carbonaceous Materials. Comparison of BET and Langmuir Surface Areas. *Powder Technol.* **2001**, *116*, 103–108.

(134) Brunauer, S.; Emmett, P. H.; Teller, E. Adsorption of Gases in Multimolecular Layers. *J. Am. Chem. Soc.* **1938**, *60*, 309–319.

(135) Palchoudhury, S.; Baalousha, M.; Lead, J. R. Methods for Measuring Concentration (Mass, Surface Area and Number) of Nanomaterials. In *Frontiers of Nanoscience*; Elsevier, 2015; Vol. 8, pp 153–181.

(136) Yurdakal, S.; Garlisi, C.; Özcan, L.; Bellardita, M.; Palmisano, G. (Photo)Catalyst Characterization Techniques. In *Heterogeneous Photocatalysis*; Elsevier, 2019; pp 87–152.

(137) Kruk, M.; Jaroniec, M. Gas Adsorption Characterization of Ordered Organic-Inorganic Nanocomposite Materials. *Chem. Mater.* **2001**, *13*, 3169–3183.

(138) Galarneau, A.; Mehlhorn, D.; Guenneau, F.; Coasne, B.; Villemot, F.; Minoux, D.; Aquino, C.; Dath, J.-P. Specific Surface Area Determination for Microporous/Mesoporous Materials: The Case of Mesoporous FAU-Y Zeolites. *Langmuir* **2018**, *34*, 14134–14142.

(139) Esen, V.; Sağlam, Ş.; Oral, B. Solar Irradiation Fundamentals and Solar Simulators. In *A Practical Guide for Advanced Methods in Solar Photovoltaic Systems*; Mellit, A., Benghanem, M., Eds.; Advanced Structured Materials; Springer International Publishing: Cham, 2020; Vol. 128, pp 3–28.

(140) Shellie, R. A. Gas Chromatography. In *Encyclopedia of Forensic Sciences*; Elsevier, 2013; pp 579–585.

(141) Sholokhova, A. Yu.; Patrushev, Y. V.; Sidelnikov, V. N.; Buryak, A. K. Analysis of Light Components in Pyrolysis Products by Comprehensive Two-Dimensional Gas Chromatography with PLOT Columns. *Talanta* **2020**, *209*, 120448.

(142) Millipore Sigma Hayesep Porous Polymer Adsorbent product page. https://www.sigmaaldrich.com/CA/en/product/supelco/10301u?context=product (accessed 2021-11-08).

(143) Varlet, V.; Smith, F.; Augsburger, M. Indirect Hydrogen Analysis by Gas Chromatography Coupled to Mass Spectrometry (GC-MS): Indirect Hydrogen Analysis. *J. Mass Spectrom.* **2013**, *48*, 914–918.

(144) Nozawa, K.; Gailhanou, H.; Raison, L.; Panizza, P.; Ushiki, H.; Sellier, E.; Delville, J. P.; Delville, M. H. Smart Control of Monodisperse Stöber Silica Particles: Effect of Reactant Addition Rate on Growth Process. *Langmuir* **2005**, *21*, 1516–1523.

(145) Musić, S.; Filipović-Vinceković, N.; Sekovanić, L. Precipitation of Amorphous SiO_2 Particles and Their Properties. *Braz. J. Chem. Eng.* **2011**, *28*, 89–94.

(146) Luo, W.; Wang, X.; Meyers, C.; Wannenmacher, N.; Sirisaksoontorn, W.; Lerner, M. M.; Ji, X. Efficient Fabrication of Nanoporous Si and Si/Ge Enabled by a Heat Scavenger in Magnesiothermic Reactions. *Sci. Rep.* **2013**, *3*, 2222.

(147) Lai, Y.; Thompson, J. R.; Dasog, M. Metallothermic Reduction of Silica Nanoparticles to Porous Silicon for Drug Delivery Using New and Existing Reductants. *Chem. Eur. J.* **2018**, *24*, 7913–7920.

(148) Martell, S. A.; Lai, Y.; Traver, E.; MacInnis, J.; Richards, D. D.; MacQuarrie, S.; Dasog, M. High Surface Area Mesoporous Silicon Nanoparticles Prepared via Two-Step Magnesiothermic Reduction for Stoichiometric CO_2 to CH_3OH Conversion. *ACS Appl. Nano Mater.* **2019**, *2*, 5713–5719.

(149) Periasamy, S.; Venkidusamy, S.; Venkatesan, R.; Mayandi, J.; Pearce, J.; Selj, J. H.; Veerabahu, R. Micro-Raman Scattering of Nanoscale Silicon in Amorphous and Porous Silicon. *Z. Phys. Chem.* **2017**, *231*, 1585–1598.

(150) Dane, A.; Demirok, U. K.; Aydinli, A.; Suzer, S. X-Ray Photoelectron Spectroscopic Analysis of Si Nanoclusters in SiO_2 Matrix. *J. Phys. Chem. B* **2006**, *110*, 1137–1140.

(151) Kim, T. Y.; Park, N. M.; Kim, K. H.; Sung, G. Y.; Ok, Y. W.; Seong, T. Y.; Choi, C. J. Quantum Confinement Effect of Silicon Nanocrystals in Situ Grown in Silicon Nitride Films. *Appl. Phys. Lett.* **2004**, *85*, 5355–5357.

(152) Esser, A.; Seibert, K.; Kurz, H.; Parsons, G. N.; Wang, C.; Davidson, B. N.; Lucovsky, G.; Nemanich, R. J. Ultrafast Recombination and Trapping in Amorphous Silicon. *Phys. Rev. B* **1990**, *41*, 2879–2884.

(153) Newman, R. C. Defects in Silicon. *Rep. Prog. Phys.* **1982**, *45*, 1163–1210.

(154) Shen, Z.; Kortshagen, U.; Campbell, S. A. Electrical Characterization of Amorphous Silicon Nanoparticles. *J. Appl. Phys.* **2004**, *96*, 2204–2209.

(155) Mataré, H. F. Carrier Transport at Grain Boundaries in Semiconductors. *J. Appl. Phys.* **1984**, *56*, 2605–2631.

(156) Bohling, C.; Sigmund, W. Self-Limitation of Native Oxides Explained. *Silicon* **2016**, *8*, 339–343.

(157) Huang, W. Q.; Jin, F.; Wang, H. X.; Xu, L.; Wu, K. Y.; Liu, S. R.; Qin, C. J. Stimulated Emission from Trap Electronic States in Oxide of Nanocrystal Si. *Appl. Phys. Lett.* **2008**, *92*, 221919.

(158) Barati, M.; Sarder, S.; McLean, A.; Roy, R. Recovery of Silicon from Silica Fume. *J. Non Cryst. Solids* **2011**, *357*, 18–23.

(159) Islam, A.; Teo, S. H.; Awual, Md. R.; Taufiq-Yap, Y. H. Assessment of Clean H_2 Energy Production from Water Using Novel Silicon Photocatalyst. *J. Clean. Prod.* **2020**, *244*, 118805.

(160) Liu, N.; Huo, K.; McDowell, M. T.; Zhao, J.; Cui, Y. Rice Husks as a Sustainable Source of Nanostructured Silicon for High Performance Li-Ion Battery Anodes. *Sci. Rep.* **2013**, *3*.

(161) Ikram, N.; Akhter, M. X-Ray Diffraction Analysis of Silicon Prepared from Rice Husk Ash. *J. Mater. Sci.* **1988**, *23*, 2379–2381.

(162) Furquan, M.; Raj Khatribail, A.; Vijayalakshmi, S.; Mitra, S. Efficient Conversion of Sand to Nano-Silicon and Its Energetic Si-C Composite Anode Design for High Volumetric Capacity Lithium-Ion Battery. *J. Power Sources* **2018**, *382*, 56–68.

(163) Bao, Z.; Weatherspoon, M. R.; Shian, S.; Cai, Y.; Graham, P. D.; Allan, S. M.; Ahmad, G.; Dickerson, M. B.; Church, B. C.; Kang, Z.; Abernathy III, H. W.; Summers, C. J.; Liu, M.; Sandhage, K. H. Chemical Reduction of Three-Dimensional Silica Micro-Assemblies into Microporous Silicon Replicas. *Nature* **2007**, *446*, 172–175.

(164) Kim, N.; Park, H.; Yoon, N.; Lee, J. K. Zeolite-Templated Mesoporous Silicon Particles for Advanced Lithium-Ion Battery Anodes. *ACS Nano* **2018**, *12*, 3853–3864.

(165) Huang, L.; Chen, J.; Yang, X.; Li, J.; Luo, X. Synthesis of Mesoporous Silicon from Industrial Waste Sodium-Based Slag. *Mater. Lett.* **2018**, *228*, 187–190.

(166) Curtis, I. S.; Wills, R. J.; Dasog, M. Photocatalytic Hydrogen Generation Using Mesoporous Silicon Nanoparticles: Influence of Magnesiothermic Reduction Conditions and Nanoparticle Aging on the Catalytic Activity. *Nanoscale* **2021**.

(167) Estrada-Flores, S.; Martínez-Luévanos, A.; Perez-Berumen, C. M.; García-Cerda, L. A.; Flores-Guia, T. E. Relationship between Morphology, Porosity, and the Photocatalytic Activity of TiO_2 Obtained by Sol–Gel Method Assisted with Ionic and Nonionic Surfactants. *Bol. Soc. Esp. Cerám. Vidr.* **2020**, *59*, 209–218.

(168) Masai, H.; Sakurai, H.; Koreeda, A.; Fujii, Y.; Ohkubo, T.; Miyazaki, T.; Akai, T. Photocatalytic Hydrogen Generation of Monolithic Porous Titanium Oxide-Based Glass-Ceramics. *Sci. Rep.* **2020**, *10*, 11615.

(169) Naik, A. P.; Mittal, H.; Wadi, V. S.; Sane, L.; Raj, A.; Alhassan, S. M.; Al Alili, A.; Bhosale, S. V.; Morajkar, P. P. Super Porous TiO_2 Photocatalyst: Tailoring the Agglomerate Porosity into Robust Structural Mesoporosity with Enhanced Surface Area for Efficient Remediation of Azo Dye Polluted Waste Water. *J. Environ. Manage.* **2020**, *258*, 110029.

(170) You-ji, L.; Wei, C. Photocatalytic Degradation of Rhodamine B Using Nanocrystalline TiO_2-Zeolite Surface Composite Catalysts: Effects of Photocatalytic Condition on Degradation Efficiency. *Catal. Sci. Technol.* **2011**, *1*, 802.

(171) Wu, S.-H.; Mou, C.-Y.; Lin, H.-P. Synthesis of Mesoporous Silica Nanoparticles. *Chem. Soc. Rev.* **2013**, *42*, 3862.

(172) Sayari, A.; Han, B.-H.; Yang, Y. Simple Synthesis Route to Monodispersed SBA-15 Silica Rods. *J. Am. Chem. Soc.* **2004**, *126*, 14348–14349.

(173) Musić, S.; Filipović-Vinceković, N.; Sekovanić, L. Precipitation of Amorphous SiO_2 Particles and Their Properties. *Braz. J. Chem. Eng.* **2011**, *28*, 89–94.

(174) Galarneau, A.; Cambon, H.; Di Renzo, F.; Ryoo, R.; Choi, M.; Fajula, F. Microporosity and Connections between Pores in SBA-15 Mesostructured Silicas as a Function of the Temperature of Synthesis. *New J. Chem.* **2003**, *27*, 73–79.

(175) Dai, F.; Zai, J.; Yi, R.; Gordin, M. L.; Sohn, H.; Chen, S.; Wang, D. Bottom-up Synthesis of High Surface Area Mesoporous Crystalline Silicon and Evaluation of Its Hydrogen Evolution Performance. *Nat. Commun.* **2014**, *5* (1).

(176) Song, H.; Liu, D.; Yang, J.; Wang, L.; Xu, H.; Xiong, Y. Highly Crystalline Mesoporous Silicon Spheres for Efficient Visible Photocatalytic Hydrogen Evolution. *ChemNanoMat* **2017**, *3*, 22–26.

(177) Lv, P.; Xu, C.; Peng, B. Design of a Silicon Photocatalyst for High-Efficiency Photocatalytic Water Splitting. *ACS Omega* **2020**, *5*, 6358–6365.

(178) Liu, D.; Li, L.; Gao, Y.; Wang, C.; Jiang, J.; Xiong, Y. The Nature of Photocatalytic "Water Splitting" on Silicon Nanowires. *Angew. Chem. Int. Ed.* **2015**, *54*, 2980–2985.

(179) Li, N.; Xiang, F.; Fratalocchi, A. Silicon-Based Photocatalysis for Green Chemical Fuels and Carbon Negative Technologies. *Adv. Sustain. Syst.* **2021**, *5*, 2000242.

(180) Gelir, A.; Yargi, O.; Yuksel, S. A. Elucidation of the Pore Size and Temperature Dependence of the Oxygen Diffusion into Porous Silicon. *Thin Solid Films* **2017**, *636*, 602–607.

(181) Xiao, N.; Li, S.; Li, X.; Ge, L.; Gao, Y.; Li, N. The Roles and Mechanism of Cocatalysts in Photocatalytic Water Splitting to Produce Hydrogen. *Chinese J. Catal.* **2020**, *41*, 642–671.

(182) Liu, M.; Xia, P.; Zhang, L.; Cheng, B.; Yu, J. Enhanced Photocatalytic H_2-Production Activity of g-C_3N_4 Nanosheets via Optimal Photodeposition of Pt as Cocatalyst. *ACS Sustain. Chem. Eng.* **2018**, *6*, 10472–10480.

(183) Michaelson, H. B. The Work Function of the Elements and Its Periodicity. *J. Appl. Phys.* **1977**, *48*, 4729–4733.

(184) Yang, J.; Wang, D.; Han, H.; Li, C. Roles of Cocatalysts in Photocatalysis and Photoelectrocatalysis. *Acc. Chem. Res.* **2013**, *46*, 1900–1909.

(185) Quaino, P.; Juarez, F.; Santos, E.; Schmickler, W. Volcano Plots in Hydrogen Electrocatalysis – Uses and Abuses. *Beilstein J. Nanotechnol.* **2014**, *5*, 846–854.

(186) Wang, Z.; Fan, J.; Cheng, B.; Yu, J.; Xu, J. Nickel-Based Cocatalysts for Photocatalysis: Hydrogen Evolution, Overall Water Splitting and CO_2 Reduction. *Mater. Today Phys.* **2020**, *15*, 100279.

(187) Korzhak, A. V.; Ermokhina, N. I.; Stroyuk, A. L.; Bukhtiyarov, V. K.; Raevskaya, A. E.; Litvin, V. I.; Kuchmiy, S. Ya.; Ilyin, V. G.; Manorik, P. A. Photocatalytic Hydrogen Evolution over Mesoporous TiO_2/Metal Nanocomposites. *J. Photochem. Photobiol. A* **2008**, *198*, 126–134.

(188) Onsuratoom, S.; Puangpetch, T.; Chavadej, S. Comparative Investigation of Hydrogen Production over Ag-, Ni-, and Cu-Loaded Mesoporous-Assembled TiO_2-ZrO_2 Mixed Oxide Nanocrystal Photocatalysts. *Chem. Eng. J.* **2011**, *173*, 667–675.

(189) Tran, P. D.; Xi, L.; Batabyal, S. K.; Wong, L. H.; Barber, J.; Chye Loo, J. S. Enhancing the Photocatalytic Efficiency of TiO_2 Nanopowders for H_2 Production by Using Non-Noble Transition Metal Co-Catalysts. *Phys. Chem. Chem. Phys.* **2012**, *14*, 11596.

(190) Wang, W.; Liu, S.; Nie, L.; Cheng, B.; Yu, J. Enhanced Photocatalytic H_2-Production Activity of TiO_2 Using $Ni(NO_3)_2$ as an Additive. *Phys. Chem. Chem. Phys.* **2013**, *15*, 12033–12039.

(191) Bi, L.; Xu, D.; Zhang, L.; Lin, Y.; Wang, D.; Xie, T. Metal Ni-Loaded g-C_3N_4 for Enhanced Photocatalytic H_2 Evolution Activity: The Change in Surface Band Bending. *Phys. Chem. Chem. Phys.* **2015**, *17*, 29899–29905.

(192) Liu, J.; Jia, Q.; Long, J.; Wang, X.; Gao, Z.; Gu, Q. Amorphous NiO as Co-Catalyst for Enhanced Visible-Light-Driven Hydrogen Generation over g-C_3N_4 Photocatalyst. *Appl. Catal. B* **2018**, *222*, 35–43.

(193) Agegnehu, A. K.; Pan, C.-J.; Rick, J.; Lee, J.-F.; Su, W.-N.; Hwang, B.-J. Enhanced Hydrogen Generation by Cocatalytic Ni and NiO Nanoparticles Loaded on Graphene Oxide Sheets. *J. Mater. Chem.* **2012**, *22*, 13849.

(194) Husin, H.; Su, W.-N.; Chen, H.-M.; Pan, C.-J.; Chang, S.-H.; Rick, J.; Chuang, W.-T.; Sheu, H.-S.; Hwang, B.-J. Photocatalytic Hydrogen Production on Nickel-Loaded $La_xNa_{1-x}TaO_3$ Prepared by Hydrogen Peroxide-Water Based Process. *Green Chem.* **2011**, *13*, 1745.

(195) Dinh, C.-T.; Pham, M.-H.; Kleitz, F.; Do, T.-O. Design of Water-Soluble CdS-Titanate-Nickel Nanocomposites for Photocatalytic Hydrogen Production under Sunlight. *J. Mater. Chem. A* **2013**, *1*, 13308.

(196) Huang, L.; Wang, X.; Yang, J.; Liu, G.; Han, J.; Li, C. Dual Cocatalysts Loaded Type I CdS/ZnS Core/Shell Nanocrystals as Effective and Stable Photocatalysts for H_2 Evolution. *J. Phys. Chem. C* **2013**, *117*, 11584–11591.

(197) Fina, F.; Ménard, H.; Irvine, J. T. S. The Effect of Pt NPs Crystallinity and Distribution on the Photocatalytic Activity of Pt-g-C_3N_4. *Phys. Chem. Chem. Phys.* **2015**, *17*, 13929–13936.

(198) Lu, Z.; Song, W.; Ouyang, C.; Wang, H.; Zeng, D.; Xie, C. Enhanced Visible-Light Photocatalytic Performance of Highly-Dispersed Pt/g-C_3N_4 Nanocomposites by One-Step Solvothermal Treatment. *RSC Adv.* **2017**, *7*, 33552–33557.

(199) Ma, W.; Xie, M.; Xie, S.; Wei, L.; Cai, Y.; Zhang, Q.; Wang, Y. Nickel and Indium Core-Shell Co-Catalysts Loaded Silicon Nanowire Arrays for Efficient Photoelectrocatalytic Reduction of CO_2 to Formate. *J. Energ. Chem.* **2021**, *54*, 422–428.

(200) De Jesus, J. C.; González, I.; Quevedo, A.; Puerta, T. Thermal Decomposition of Nickel Acetate Tetrahydrate: An Integrated Study by TGA, QMS and XPS Techniques. *J. Molec. Catal. A* **2005**, *228*, 283–291.

(201) Fu, X.; Zhang, L.; Liu, L.; Li, H.; Meng, S.; Ye, X.; Chen, S. In Situ Photodeposition of MoS_x on CdS Nanorods as a Highly Efficient Cocatalyst for Photocatalytic Hydrogen Production. *J. Mater. Chem. A* **2017**, *5*, 15287–15293.

(202) Li, J.; Li, P.; Li, J.; Tian, Z.; Yu, F. Highly-Dispersed Ni-NiO Nanoparticles Anchored on an SiO_2 Support for an Enhanced CO Methanation Performance. *Catalysts* **2019**, *9*, 506.

(203) Roy, P. S.; Bhattacharya, S. K. Size-Controlled Synthesis, Characterization and Electrocatalytic Behaviors of Polymer-Protected Nickel Nanoparticles: A Comparison with Respect to Two Polymers. *RSC Adv.* **2014**, *4*, 13892–13900.

(204) Brindley, G. W.; Hayami, R. Kinetics and Mechanism of Formation of Forsterite (Mg_2SiO_4) by Solid State Reaction of MgO and SiO_2. *Philo. Mag. Lett.* **1965**, *12*, 505–514.

(205) Miao, T. J.; Tang, J. Characterization of Charge Carrier Behavior in Photocatalysis Using Transient Absorption Spectroscopy. *J. Chem. Phys.* **2020**, *152*, 194201.

(206) Zhou, S.; Fang, C.; Song, X.; Liu, G. The Influence of Compact and Ordered Carbon Coating on Solid-state Behaviors of Silicon during Electrochemical Processes. *Carbon Energy* **2020**, *2*, 143–150.

(207) Min, Jeong-Hye; Bae, Young-San; Kim, Joong-Yeon; Kim, Sung-Soo; Song, Seung-Wan. Self-Organized Artificial SEI for Improving the Cycling Ability of Silicon-Based Battery Anode Materials. *Bull. Korean Chem. Soc.* **2013**, *34*, 1296–1299.

(208) Wang, J.; Liao, L.; Lee, H. R.; Shi, F.; Huang, W.; Zhao, J.; Pei, A.; Tang, J.; Zheng, X.; Chen, W.; Cui, Y. Surface-Engineered Mesoporous Silicon Microparticles as High-Coulombic-Efficiency Anodes for Lithium-Ion Batteries. *Nano Energy* **2019**, *61*, 404–410.

(209) Liu, C.-Y.; Holman, Z. C.; Kortshagen, U. R. Hybrid Solar Cells from P3HT and Silicon Nanocrystals. *Nano Lett.* **2009**, *9*, 449–452.

(210) Morozova, S.; Alikina, M.; Vinogradov, A.; Pagliaro, M. Silicon Quantum Dots: Synthesis, Encapsulation, and Application in Light-Emitting Diodes. *Front. Chem.* **2020**, *8*, 191.

(211) Miyano, M.; Endo, S.; Takenouchi, H.; Nakamura, S.; Iwabuti, Y.; Shiino, O.; Nakanishi, T.; Hasegawa, Y. Novel Synthesis and Effective Surface Protection of Air-Stable Luminescent Silicon Nanoparticles. *J. Phys. Chem. C* **2014**, *118*, 19778–19784.

APPENDIX A. Energy-Dispersive X-Ray Spectra

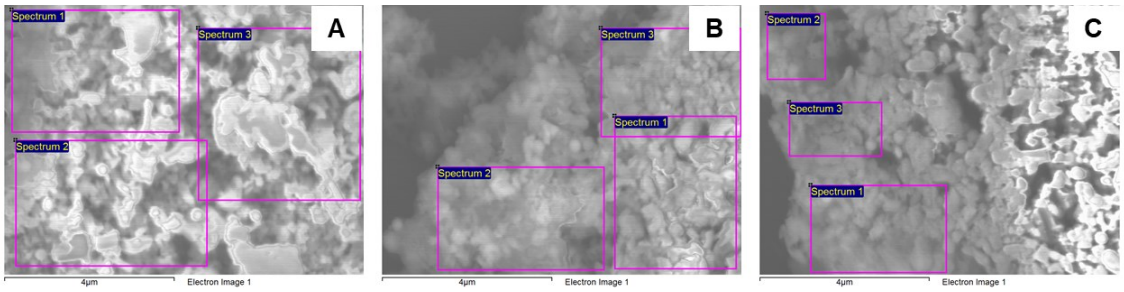

Image	Spectrum Number	C	O	Si	Na	Cl
A	1	2.61	27.42	69.97		
	2	2.64	26.9	70.46		
	3	2.83	28.71	68.46		
B	1	9.75	32.97	55.36	0.74	1.18
	2	9.43	30.91	58.31	0.60	0.75
	3	10.53	33.01	54.93	0.73	0.79
C	1	6.28	24.91	68.52	0.30	
	2	9.63	26.45	63.58	0.34	
	3	9.05	25.15	65.8		

Figure A. 1. Images used for EDS analysis and results table for mp-Sip4 NPs. Numerical results are presented in atomic %.

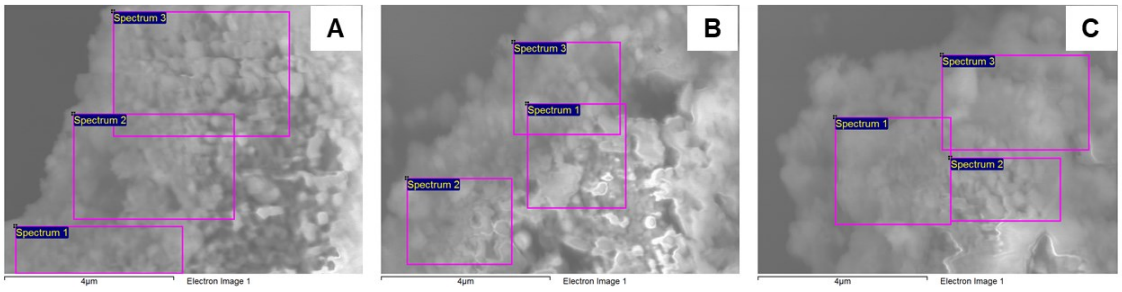

Image	Spectrum Number	C	O	Si
A	1	9.34	32.32	58.34
	2	8.03	32.82	59.14
	3	8.82	34.49	56.70
B	1	11.35	32.51	56.14
	2	10.35	28.24	61.41
	3	12.52	31.75	55.72
C	1	7.15	30.77	62.08
	2	7.16	31.53	61.31
	3	5.43	27.65	66.93

Figure A. 2. Images used for EDS analysis and results table for mp-Sip6 NPs. Numerical results are presented in atomic %.

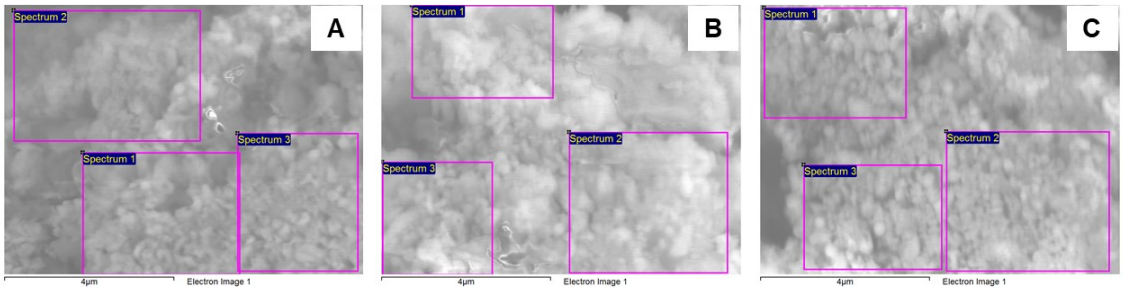

Image	Spectrum Number	C	O	Si
A	1	6.03	44.50	49.47
	2	6.38	37.53	56.09
	3	5.97	46.66	47.37
B	1	5.01	46.23	48.77
	2	4.17	45.38	50.44
	3	4.70	45.74	49.55
C	1	11.14	38.95	49.91
	2	9.69	37.69	52.62
	3	10.94	39.66	49.40

Figure A. 3. Images used for EDS analysis and results table for mp-Sip8 NPs. Numerical results are presented in atomic %.

APPENDIX B. Copyright Information

Photocatalytic hydrogen generation using mesoporous silicon nanoparticles: influence of magnesiothermic reduction conditions and nanoparticle aging on the catalytic activity

I. S. Curtis, R. J. Wills and M. Dasog, *Nanoscale*, 2021, **13**, 2685 **DOI:** 10.1039/D0NR07463B

ROYAL SOCIETY OF CHEMISTRY

Paper number: _____

Licence to Publish Agreement

This licence to publish agreement (hereinafter the **Agreement**) sets out the rights granted to the Royal Society of Chemistry (**RSC**) a company incorporated in England by Royal Charter (Registered No. RC000524) and a Registered Charity No. 207890 whose registered office is located at Burlington House, Piccadilly London W1J 0BA, United Kingdom by the Copyright Owner(s) to allow the RSC to publish the Article and Supplementary Material, as defined below. It also sets out the rights and warranties of the Copyright Owner(s). Publication is subject to the terms and conditions set out below.

1.1 By signing this Agreement, the Copyright Owner(s) will be deemed to have read and accepted the terms and conditions of the Agreement, confirm that all the authors are aware of the content of the Article at the time of submission, agree to grant the licence as detailed herein and confirm that they have the right to grant such licence.

Licenced rights granted to the RSC

2.1 In consideration of the Copyright Owner(s) granting the RSC the rights in clause 2.2 (a) to (b), the RSC shall evaluate the Article for publication and publish the Article if it is appropriate to do so, within the RSC's sole discretion.

2.2 If the RSC publishes the Article under clause 2.1, the Copyright Owner(s) grant to RSC and its partners (clause 2.6), from the date of acceptance of the Article for publication and for the full term of any copyright and database rights in the Article (including all renewals, extensions and reversions), the exclusive rights to :

(a) to edit, adapt, publish, reproduce, distribute, display, and store the Article in all forms, formats, and media whether now known or hereafter developed (including but without limitation in print, digital or electronic form) throughout the world, and
(b) to translate the Article into other languages, create adaptations, summaries or extracts of the Article or other derivative works based on the Article and exercise all of the rights set forth in (a) above in such translations, adaptations, summaries, extracts, and derivative works.

(subject to the remaining provisions of this clause 2 and clause 3)

2.3 The Copyright Owner(s) also grants to RSC all the same rights at clause 2.2 above, on a non-exclusive basis, for any Supplementary Material submitted with the Article (and published if RSC so decides).

2.4 The Copyright Owner shall promptly notify the RSC in writing if any government or public body or equivalent throughout the world (**Public Body**) is the owner of any rights or is the holder of any information contained in the Article or the Supplementary Material (**Public Information**). Notwithstanding anything to the contrary in the Agreement, the licences granted under clause 2.2 and clause 2.3 (**Licences**) shall only extend to such Public Information if and to the extent permissible by applicable laws or under licence from the Public Body (including, if applicable, on a non-exclusive basis). If reasonably required by the RSC, the Copyright Owner shall use reasonable endeavours to assist the RSC in obtaining the necessary permissions from the relevant Public Body for the RSC to publish the Article as anticipated under the Agreement.

2.5 Subject to clause 2.4, the licence and rights at clause 2.1, 2.2 and 2.3 above are freely transferable by RSC and include the right to sub-license without limitation. RSC may sell or distribute the Article and/or Supplementary Material within a journal, on its own, or with other related material.

2.6 If the journal in which the Article is to be published is published by RSC on behalf of any other organisation(s), or by RSC as part owner of, the licence and rights granted at clause 2.1, 2.2 and 2.3 above shall also be deemed granted to the other organisation(s).

2.7 If any third party infringes, or on reasonable grounds appears to be infringing, any intellectual property rights in the Article and/or Supplementary Material, and RSC is of the reasonable belief that this infringement will be prejudicial to or interfere with its business, RSC shall have the right to bring an action for infringement pursuant to section 101A of the Copyright, Designs and Patents Act 1988 (as amended, extended or re-enacted from time to time) or its equivalent legislation in any relevant jurisdiction. The RSC is hereby authorised by the Copyright Owner(s) independently to take such steps as RSC considers necessary or appropriate in respect of such infringement, including the institution and conduct of legal proceedings and any subsequent appeals. In doing so, RSC shall not be taken as acting as agent or acting in any way on behalf of the Copyright Owner(s). RSC shall bear all costs arising from taking such steps but shall be entitled to retain for its absolute benefit any damages, profits, costs or other amounts awarded or recovered in such proceedings.

2.8 The Copyright Owner(s) hereby consents to the inclusion of electronic links from the Article to third party material wherever it may be located.

2.9 The rights to any raw research data included in the Article are not covered by the Agreement.

2.10 Submission of the Article does not guarantee publication. If the Article is withdrawn, rejected, or not published, RSC shall notify the Copyright Owner(s) of this and the rights aforementioned in clause 2.2 shall not take effect, or if they have taken effect, shall terminate with immediate effect upon the RSC notifying the Copyright Owner(s) of the same. The RSC' may need to retain a copy of the Article and Supplemental Material as a record (including via any contractor) but will do so only for as long as is reasonably required.

2.11 The Copyright Owner(s) agrees to be RSC's primary point of contact in respect of this Agreement. The Copyright Owner(s) shall be responsible for ensuring up to date contact details are provided to the RSC.

Copyright owner(s)' Rights

3.1 Ownership of the copyright remains with the Copyright Owner(s). The Copyright Owner(s) waives such of its rights as it may be necessary to waive in order for RSC to exercise any of the rights granted at clause 2 above, with the exception of the rights listed at clause 3.2 below which are reserved by the Copyright Owner(s) on its own behalf or for the benefit of (and exercisable by) them, and so are granted under clause 2 on a non-exclusive basis.

3.2 The Copyright Owner shall retain the following non-exclusive rights:

(a) in the **Submitted Manuscript**:
  (i) the right to self-archive the Submitted Manuscript on the Copyright Owner's personal website, place in a preprint server or repository or in an Approved SCN or in the Copyright Owner's company/institutional repository or archive. The right extends to both intranets and the Internet. The Copyright Owner may replace (or authorise replacement of) the Submitted Manuscript with the Accepted Manuscript, after the embargo period as set out in 3.2(b)(ii) below has elapsed;
  (ii) the right to share copies of the Submitted Manuscript with colleagues, including via Approved SCN's, provided there is no systematic distribution or automated delivery;

(b) in the **Accepted Manuscript**:
  (i) the right to share copies of the Accepted Manuscript with colleagues within private research sharing groups only including via intranets and Approved SCN's provided there is no systematic distribution, the Accepted Manuscript is not updated or replaced with the Version of Record and the Copyright Owner ensures recipients are notified that the Accepted Manuscript must not be used for Commercial Use,
  (ii) following expiry of any embargo period secured pursuant to 3.7 below, the right to make available the Accepted Manuscript via the Copyright Owner's personal website; archive the Accepted Manuscript in the Copyright Owner(s)'s or employer's institutional or other open access repository and, archive the same in Approved SCN's and in subject based repositories and the Copyright Owner shall be entitled to permit third parties who access the Accepted Manuscript via these repositories to copy and reproduce (but not adapt or create derivatives versions of) the Accepted Manuscript in accordance with the provisions of the Creative Commons licence CC BY NC ND (3.0).

(c) with respect to the **Version of Record**:
   (i) the personal right of the Copyright Owner only to share copies of the Version of Record in any format with colleagues upon their express request and for their personal use and with private research sharing groups including via intranets and Approved SCN's, there is no systematic distribution/networking of the Version of Record to external users and, recipients are notified that they may not further distribute or copy the Version of Record,
   (ii) the right to include the Version of Record in normal teaching duties at the Copyright Owner's university/institution or internal training at the Copyright Owner's place of employment,
   (iii) the right to include (in whole or in part) in submissions of grant applications, and the thesis of the Copyright Owner in printed form and the right to create and make the PDF in the thesis of the Copyright Owner available via any website that the university/institution of the Copyright Owner may have for the deposition of the same. Recipients of the PDF must be notified that this may not be further made available or distributed,
   (iv) reproduce, perform, transmit and otherwise communicate the Version of Record in spoken presentations (including those which are accompanied by visual materials such as slides, overheads and computer projections);

(d) with respect to **Article abstracts, figures, tables, artworks and selected text (up to 10% of total words)**
   (i) the Copyright Owner may re-use unmodified abstracts for use other than Commercial Use,
   (ii) the Copyright Owner may re-use figures, tables, artworks, and selected text up to 10% of the total number of words from the Article, provided full and accurate credit is given to the Version of Record, no changes are made other than modification to the figures and tables being noted, re-use must not be for Commercial Use and, there is no dual publication in breach of journal ethical practices.

3.3 The Copyright Owner must submit a written request to RSC for any use other than those specified at clause 3.2 above.

3.4 All cases of republication/reproduction must be accompanied by an acknowledgement of first publication of the Article by RSC, the wording of which depends on the journal in which the Article was published originally. The acknowledgement should also include a hyperlink to the Article on the RSC website.

3.5 In all cases of deposition there must be a link from the deposited version to the Version of Record on the RSC website.

3.6 The Copyright Owner and/or RSC may deposit the Supplementary Material corresponding to the Article in any repository, there being no embargo.

3.7 The embargo period referred to in 3.2(a)(i) and (3.2(b)(ii) above is 12 months from the date of publication by RSC of the Accepted Manuscript or the final Version of Record if the Article was not published as an Accepted Manuscript.

Copyright Owner Warranties

4.1 The Copyright Owner(s) warrants that:

(a) where the Article and Supplementary Material is multi-authored, all individuals identified contributed to the Article and Supplementary Material and all individuals who contributed are named in the Article;
(b) the Copyright Owner has obtained written permissions from third party copyright owner(s) to grant the licence and rights to RSC as their agent on these terms and that all Copyright Owner(s) agree to the obligations herein. The Copyright Owner(s) will supply a copy of the same to RSC upon request; and
(c) if copyright in the Article is owned by any third party, whether an employer or third party to whom the Copyright Owner(s) has assigned rights, the Copyright Owner(s) have obtained written authorisation from such copyright owner to grant this licence to the RSC on their behalf as their agent. The Copyright Owner(s) will supply a copy of the same to RSC upon request.

4.2 The Copyright Owner(s) further warrants that:

(a) the Article and Supplementary Material is the original work of the Copyright Owner(s) and has not been copied (in whole or in part) from any other work or matter or, if the Article and/or Supplementary Material includes excerpts of copyright work of persons other than the Copyright Owner(s), the Article and Supplementary Material is substantially the original work of the Copyright Owner(s) and all permissions as are necessary for the grant of the licence and rights to RSC herein have been obtained for use of such excerpts and all necessary credits to the sources have been included;

(b) the Article and Supplementary Material and the exercise of the licence and rights granted to RSC by the Agreement will in no way whatsoever infringe the intellectual property rights (including without limitation copyright, database rights, patent or trademark or other third party rights) of any person whatsoever or result in breach of any existing duty of confidentiality, or duty to respect privacy, or any other right (including any moral right) of any person or entity whatsoever or breach of any contract or of any law;

(c) the Article and the Supplementary Material do not contain anything which is defamatory, libellous or unlawful and that, to current scientific knowledge, all statements contained in the Article and the Supplementary Material purporting to be facts are true and any recipe, formula, instruction or equivalent contained in the Article will not, if followed accurately, cause any injury or damage to the user;

(d) there are no conflicts of interest relating to the Article and Supplementary Material, except as disclosed;

(e) the Copyright Owner(s) has read and complied with the RSC guidelines: http://www.rsc.org/journals-books-databases/journal-authors-reviewers/author-responsibilities/ and confirms that the Article has not been, and will not prior to publication by RSC be, published, with the exception of such deposition or presentation of the research in the manner listed at clause 3 above and which is in line with the RSC guidelines referred to above.

4.3 The Copyright Owner(s) shall be responsible for ensuring that the correct permissions and rights have been granted to them in writing from any other copyright owner as mentioned in clause 4 above, in order to submit the Article to the RSC and grant the RSC the rights detailed in clause 2.

4.4 All warranties and obligations set out in clauses 4.1; 4.2(a), 4.2(b), 4.2(c); and 4.3 are subject to clause 2.4 and, accordingly, do not extend to the Copyright Owner's dealings with Public Information contained in the Article or Supplementary Materials.

General

5.1 In exercising its rights and performing its obligations under the Agreement, each party shall comply with all applicable laws, rules and regulations of governmental entities having jurisdiction over such performance including but not limited to its obligations under the Data Protection Act 2018 and UK GDPR (as amended or updated from time to time) which arise in connection with the Agreement with regard to the use of personal data and its obligations under the Bribery Act 2010 (as amended).

5.2 RSC is entitled to assign its rights under the Agreement to any third party without the prior written consent of any other party to this Agreement.

5.3 No change or modification of the Agreement will be valid unless agreed by both parties in writing.

5.4 Failure or delay by RSC to exercise any right or remedy under the Agreement shall not be deemed to be a waiver of that right or remedy, or prevent RSC from exercising that or any other right or remedy on any occasion.

5.5 The Agreement shall be governed by English law and the parties submit for all purposes connected with the Agreement to the exclusive jurisdiction of the English courts.

SIGNED by the Owner or by someone duly authorised to sign for the Owner.

Signed:.....

Name: .....

Date:.....

Definitions

Accepted Manuscript:	the manuscript version of the Article that has been accepted for publication and may include Author-incorporated changes suggested during submission, peer review, and editor-Author communications but excludes other RSC value-added contributions such as copy-editing, formatting, technical enhancements and (if relevant) pagination and subsequent author corrections at proof stage.
Article:	all the material that comprises the article submitted to RSC pursuant to this Agreement, including but not limited to the abstract, tables, reference lists, figures, images, multimedia files that are directly embedded within the text, and the text itself. The Article does not include the Supplementary Material.
Copyright owner:	the individual, group or entity (or entities) that are the original legal owners of the copyright in the Article and Supplementary Material (as applicable). This will usually be the author(s) of the article (whether sole or joint), but may also be an employer where that author created the Article and Supplementary Material in the course of their employment, or a third party where that third party has a vested interest in the Article or Supplementary Material such as funding any element of research or providing any services or supplies which contributed to the content of the Article or Supplementary Material;
Commercial Use:	includes without limitation: • copying or downloading of documents, or linking to such postings, for further redistribution, sale or licensing, for a fee; • copying, downloading or posting by a site or service that incorporates advertising with such content; • inclusion or incorporation of document content in other works or services (other than for legally permitted quotations with an appropriate citation) that is then available for sale or licensing for a fee; • use of documents or document content (other than for legally permitted quotations with appropriate citation) by organisations for any promotional or advertising purposes whether direct or indirect, whether for a fee or otherwise. • use for the purposes of monetary reward by means of sale, resale, license, loan, hire transfer or other form of commercial exploitation.
Scholarly Collaboration Network (SCN):	a professional networking site that facilitates collaboration among researchers as well as the sharing of data, results, and publications. An approved SCN is one which endorses and is a signatory to the voluntary STM article sharing principles (see: https://www.stm-assoc.org/2015_06_08_Voluntary_principles_for_article_sharing_on_scholarly_collaboration_networks.pdf).
Submitted Manuscript:	the manuscript version of the Article (including Supplementary Material) as originally submitted by the Corresponding Author for publication.

Supplementary Material:	material that has been judged by peer review as being relevant to the understanding of the Article but too lengthy or of too limited interest for inclusion in the Article itself. Supplementary Material will be made available electronically only and may include data tables or sets, appendices, movie or audio clips, or other multimedia files.
Version of Record:	the final published version of the Article that is produced by the RSC after peer review, electronic production and other publisher value-added contributions such as copy-editing, formatting, technical enhancements and (if relevant) pagination.